ELECTRON PARAMAGNETIC RESONANCE SPECTROSCOPIC STUDY OF TWO GADOLINIUM CENTRES AT CALCIUM SITES IN SYNTHETIC FLUORAPATITE

A Thesis

Submitted to the College of Graduate Studies and Research

in Partial Fulfillment of the Requirements

for the Degree of Doctor of Philosophy

in the

Department of Geological Sciences

University of Saskatchewan

by

Ning Chen

Spring 2002

In presenting this thesis in partial fulfillment of the requirements for a Doctor of Philosophy degree from the University of Saskatchewan, I agree that the Libraries of this University may make it freely available for inspection. I further agree that permission for copying of this thesis in any manner, in whole or in part, for scholarly purposes may be granted by the professors who supervised my thesis work or, in their absence, by the Head of the Department of Geological Sciences or the Dean of the College of Graduate Studies and Research, in which my thesis work was done. It is understood that any copying or publication or use of this thesis or parts thereof for financial gain shall not be allowed without my written permission. It is also understood that due recognition shall be given to me and to the University of Saskatchewan in any scholarly use which may be made of any material in my thesis.

Requests for permission to copy or to make other use of material in this thesis in whole or in part should be addressed to:

Head of the Department of Geological Sciences
114 Science Place
University of Saskatchewan
Saskatoon, Saskatchewan S7N 5E2

ABSTRACT

Gd-doped fluorapatite, synthesized from CaF_2-rich melts, has been investigated as single crystals and powder samples by using X-band (9.5 GHz) and W-band (95 GHz) electron paramagnetic resonance (EPR) spectroscopy. Gd_2O_3 with natural abundances of isotopes and ^{157}Gd-enriched Gd_2O_3 were used in the crystal synthesis. The X-band spectra obtained for the Gd-doped fluorapatite displayed a well-resolved type of Gd^{3+} centre (the centre 'a') caused by the Gd even isotopes (electron spin: S = 7/2; nuclear spin: I = 0), and suggested the possible presence of a second partly-resolved type of Gd^{3+} centre (the centre 'b') also caused by the Gd even isotopes. The latter was thoroughly disclosed in the W-band spectra.

The single-crystal X- and W- band EPR spectra from three orthogonal rotation planes obtained from the Gd-doped fluorapatite allowed determination of the general spin-hamiltonian parameters for Gd^{3+} centres 'a' and 'b', including the spin terms of type BS (**g** matrix) and S^2 (**D** matrix), and the parameters associated with the high-spin terms of type S^4 and S^6, as well as BS^3 and BS^5. The validity of the spin-hamiltonian parameters was confirmed by agreement between the observed and simulated EPR spectra for both single-crystal and powder samples.

The principal values of the matrices **g** and **D** for the centres 'a' and 'b' indicate that the two Gd^{3+}-occupied sites in the synthetic fluorapatite have rhombic local symmetry. The principal directions of the **D** matrices suggest that the centres 'a' and

'b' correspond to substitutions of Gd^{3+} into Ca2 and Ca1 sites, respectively. These site assignments are supported by the results of pseudo-symmetry analyses using the S^4 parameters. For example, the calculated pseudo-symmetry axes of the centre 'a' coincide with the local rotoinversion axis, site coordinations, as well as the faces of the coordination polyhedra of the Ca2 sites. The local structural environments of the centres 'a' and 'b' also suggest that the Gd^{3+} ions are incorporated into the Ca2 and Ca1 via $Gd^{3+} + O^{2-} \Leftrightarrow Ca^{2+} + F^-$ and $2Gd^{3+} + \square \Leftrightarrow 3Ca^{2+}$, respectively. The vacancy ($\square$) associated the centre 'b' has been shown to be located at a nearest-neighbor Ca2 site, resulting in a Gd^{3+}--$\square$--- Gd^{3+}arrangement, with the cations well separated.

The single-crystal X- and W-band EPR spectra of the ^{157}Gd-doped fluorapatite revealed a well-resolved ^{157}Gd (nuclear spin: I =3/2) hyperfine structure (HFS) of the centre 'a' and a partly-resolved ^{157}Gd HFS of the centre 'b'. The calculated spin-hamiltonian parameters for the hyperfine, nuclear quadrupole, and nuclear Zeeman effects (i.e., matrices **A**, **P** and $\mathbf{g}_n$) provide further evidence for the site assignment of the centres 'a' to ^{157}Gd nuclides at the Ca2 sites, with rhombic local symmetry. The **P** matrix also suggests that the electric-field gradient at the ^{157}Gd nuclides of the centre 'a' is close to uniaxial, with the largest value along the direction of the Ca2-O2 bond and almost isotropic in the horizontal plane. Moreover, single-crystal spectrum simulations have shown that the hyperfine anisotropy of the centre 'a' arises not only from **A**, **P** and $\mathbf{g}_n$ but is also affected by terms BS (**g**), S^2 (**D**), S^4, S^6, BS^3 and BS^5.

ACKNOWLEDGEMENTS

I am grateful to Dr. Yuanming Pan, Department of Geological Sciences, University of Saskatchewan, and Dr. John A. Weil, Department of the Chemistry, University of Saskatchewan, who supervised my doctoral dissertation, and to the members of my advisory committee: Dr. Chris Holmden, Dr. Robert W. Kerrich, Dr. Malcolm J. Reeves, Dr. Robin W. Renaut.

I thank Dr. M. J. Nilges for collaborative work with W-band EPR experiments at Illinois EPR Research Center (IERC), University of Illinois at Urbana-Champaign, and Dr. J. Du of the Department of Chemistry, University of Saskatchewan for assistance with the X-band EPR experiments. I also thank Mr. T. Bonli and Dr. Qianli Xie of the Department of Geological Sciences, University of Saskatchewan, for assistance with the electron microprobe and laser-ablation inductively-coupled plasma mass spectrometry analyses, respectively.

I gratefully acknowledge the Natural Science and Engineering Research Council (NSERC) of Canada for financial support through research grants to Dr. Y. M. Pan. My study was also supported by a 1996-99 Graduate Scholarship (Ph.D.) and a 1999-2000 Graduate Teaching Fellowship (GTF) from the University of Saskatchewan.

TABLE OF CONTENTS

Copyright Statement I
Abstract II
Acknowledgements IV
Table of Contents V
List of Figures VII
List of Tables X

Chapter 1 Introduction 1
1.1 Previous Work 1
1.2 Thesis Outline 2
1.3 Crystal Structure of Fluorapatite 3

Chapter 2 Local Structural Environment and Substitution Mechanism of the Gd^{3+} centre 'a' 6
2.1 Introduction 6
2.2 Spin-hamiltonian 7
2.3 Measurement Methods 12
2.3.1 Synthesis and characterization of fluorapatite crystals 12
2.3.2 Single-axis crystal holder 13
2.3.3 X-band EPR experiments 17
2.4 Results and Discussions 22
2.4.1 X-band EPR spectra 22
2.4.2 EPR lineshapes and linewidths 25
2.4.3 Spin-hamiltonian optimization and EPR data simulation 27
2.4.4 Pseudo-symmetry analysis 36
2.4.5 Substitution mechanism 39
2.4.6 Conclusions 42

Chapter 3 Local Structure Environment and the Neighboring Ca2 Vacancy of the Gd^{3+} centre 'b' 43
3.1 Introduction 43
3.2 Experimental Methods 44
3.2.1 Synthesis and characterization of fluorapatite crystals 44
3.2.2 EPR experiments 45

3.3 Results and Discussions 52
3.3.1 EPR spectra 52
3.3.2 EPR lineshape and linewidths 58
3.3.3 Spin-hamiltonian optimization and spectral simulation 61
3.3.4 Pseudo-symmetry analysis 70
3.3.5 Association between Gd^{3+} and Ca^{2+} vacancy 73
3.3.6 Comparison of the Gd^{3+} centres 'a' and 'b' in fluorapatite 75
3.4 Conclusions 76

Chapter 4 ^{157}Gd Hyperfine Structure Anisotropy and Nuclear Quadrupole Effect of the Gd^{3+} centre 'a' 77
4.1 Introduction 77
4.2 Experimental Methods 81
4.2.1 Synthesis and characterization of ^{157}Gd-doped fluorapatite crystals 81
4.2.2 EPR experiments 81
4.3 Results and Discussions 85
4.3.1 EPR spectra 85
4.3.2 Optimization of matrices **A**, **P** and $\mathbf{g}_n$ 86
4.3.3 X-band spectrum simulation 100
4.3.4 W-band spectrum simulation 100
4.3.5 Hyperfine Anisotropy 101
4.3.5.1 Line-position and total-splitting anisotropy 102
4.3.5.2 Transition-probability anisotropy 110
4.4 Conclusions 116

Chapter 5 Summary 117

Chapter 6 Future Work 121

References 124

Appendix I Computer Software EPR-NMR 133
Appendix II Computer Software ROTSTO 142

LIST OF FIGURES

Figure 1.1	Projection (001) of the fluorapatite structure	4
Figure 1.2	Local environment of the sites $Ca1^1$ and $Ca2^1$	5
Figure 2.1a	Simulated energy levels for the Gd^{3+} centre 'a' when **B//z**	9
Figure 2.1b	Simulated energy levels for the Gd^{3+} centre 'a' when **B//y'**	10
Figure 2.2	Single-axis crystal holder	14
Figure 2.3	Alignment of fluorapatite crystals	15
Figure 2.4	Single-crystal spectra of the Gd-doped Fluorapatite	18
Figure 2.5a	Angular dependence of the X-band EPR spectra in the xy plane for the Gd^{3+} centre 'a'	19
Figure 2.5b	Angular dependence of the X-band EPR spectra in the yz plane for the Gd^{3+} centre 'a'	20
Figure 2.5c	Angular dependence of the X-band EPR spectra in the xz plane for the Gd^{3+} centre 'a'	21
Figure 2.6	Observed and simulated X-band powder EPR spectra for the Gd^{3+} centre 'a'	23
Figure 2.7	Stereographic projection of the principal directions of the D matrix of the Gd^{3+} centre 'a'	32
Figure 2.8a	Observed and simulated single-crystal X-band EPR spectra for the Gd^{3+} centre 'a' with **B//z'** and $\mathbf{B_1//x'}$	33
Figure 2.8b	Observed and simulated single-crystal X-band EPR spectra for the Gd^{3+} centre 'a' with **B//y'** and $\mathbf{B_1//z'}$	34
Figure 2.9	Stereographic projection of the calculated pseudo-symmetry axes for the Gd^{3+} centre 'a'	37
Figure 3.1a	Calculated angular dependence of the W-band EPR spectra in the xy plane for the Gd^{3+} centre 'b'	46
Figure 3.1b	Calculated angular dependence of the W-band EPR spectra in the yz plane	47

Figure 3.1c	Calculated angular dependence of the W-band EPR spectra in the xz plane for the Gd^{3+} centre 'b'	48
Figure 3.2	Observed and simulated W-band single-crystal EPR spectrum for the Gd^{3+} centre 'b' with **B**//**z**' and $\mathbf{B}_1$//**x**'	49
Figure 3.3	Observed single-crystal W-band EPR Spectra the Gd^{3+} centers 'a' and 'b'	50
Figure 3.4a	Simulated energy levels at **B**//**z** for the Gd^{3+} centre 'b' in fluorapatite	54
Figure 3.4b	Simulated energy levels at **B**//**z** for the Gd^{3+} centre 'a' in fluorapatite	55
Figure 3.5	Observed and simulated single-crystal W-band EPR spectra for the Gd^{3+} centre 'a' and 'b' with **B**//**z**' and $\mathbf{B}_1$//**x**' in fluorapatite	57
Figure 3.6	Projection along the crystallographic c axis of the principal directions D_1 and D_2 of the Gd^{3+} centre 'b'	67
Figure 3.7	Observed and simulated Q-band powder Spectrum for the centre 'a' and 'b'	68
Figure 3.8	Stereographic projection (**c**//**z**) of the calculated pseudo-symmetry axes of the Gd^{3+} centre 'b'	69
Figure 4.1	X-band single-crystal spectra of the ^{157}Gd-doped fluorapatite for the Gd^{3+} centre 'a'	83
Figure 4.2	W-band single-crystal spectra of the ^{157}Gd-doped fluorapatite for the the Gd^{3+} centre 'a'	84
Figure 4.3	Hyperfine energy levels and transitions, transition probabilities and simulated hyperfine structure of X-band EPR the Gd^{3+} centre 'a'	88
Figure 4.4	Stereographic projection of the principal directions of the matrices A and P as well as local symmetry axes and faces of the Gd^{3+} centre 'a'	91
Figure 4.5	Observed and simulated X-band HFS the Gd^{3+} centre 'a'	98
Figure 4.6	Observed and simulated ^{157}Gd W-band HFS the Gd^{3+} centre 'a'	99
Figure 4.7	Simulation of the line-position roadmap for hyperfine structure of the $^{157}Gd^{3+}$ centre 'a'	103-6
Figure 4.8	Simulation of total splitting of the X-band hyperfine structure of the $^{157}Gd^{3+}$ centre 'a'	107-8
Figure 4.9	Simulation of the transition probabilities	

of the $^{157}Gd^{3+}$ X-band hyperfine structure
HFS the Gd^{3+} centre 'a' 111-4
Appendix 1.1 Schematic diagram of the program EPR-NMR 134
Appendix 1.2a An example of an input file to EPR-NMR
for optimization of the g matrix 135
Appendix 1.2b An example of an input file to EPR-NMR
for angle correction 136
Appendix 1.3 Flow-chart of the optimization procedure
for the spin-hamiltonian parameters (say)
of the even-isotope Gd^{3+} spectra 137

LIST OF TABLES

Table 2.1 The principal values and directions of matrices **Y** = **g** and **D** (and values of D and E) for the Gd^{3+} centre 'a' at 294.8(13) K 29

Table 2.2 Parameters of the high-spin terms of type S^4, S^6 and BS^3 for the Gd^{3+} centre 'a' at 294.8(13) K 30

Table 3.1 Ideal and calibrated directions of the rotation-plane normals and the crystal reference systems in the W-band EPR experiments 53

Table 3.2 The principal values and directions of the matrix **g** for the Gd^{3+} centre 'b' at ~ 287 K and the centre 'a' at 294.8 K 64

Table 3.3 The principal values (in magnetic-field units) and directions of the matrices **D** for the Gd^{3+} centre 'b' at ~ 287 K and the centre 'a' at 294.8 K 65

Table 3.4 Parameters of the high-spin terms of type S^4, S^6 and BS^3 for the Gd^{3+} centre 'b' at ~ 287 K 66

Table 3.5 Comparison of the calculated pseudo-symmetry elements with the principal directions of the matrix **D** and with selected bonds and faces of the CaO_9 coordination polyhedron of a $Ca1^1$ site 72

Table 4.1 Spin-hamiltonian term labels 80

Table 4.2 Energy levels and t ransition labels a Gd^{3+} centre 94

Table 4.3 Simulated line positions and transition probabilities for HFS for the $^{157}Gd^{3+}$ centre 'a' 95

Table 4.4 Ideal and real experimental reference systems for single-crystal EPR experiment on $^{157}Gd^{3+}$-doped fluorapatite 96

Table 4.5 The principal values and directions of the matrices **A** and **P** for the $^{157}Gd^{3+}$ centre 'a' 97

CHAPTER 1

Introduction

1.1 Previous Work

Apatites [$Ca_{10}(PO_4)_6(F,OH,Cl)_2$] are important host minerals for rare-earth elements (REEs, Z = 57-71) in igneous, metamorphic and sedimentary rocks and in biomasses (e.g., Wright et al., 1984; Fleet and Pan, 1995a; 1997a and references therein). Numerous studies have applied the compositions of the rare-earth elements (REE) in apatites as petrogenetic tools in elucidating the sources and evolution of igneous, metamorphic and sedimentary rocks (e.g., Watson and Green, 1981; Fleet and Pan, 1997a), and as geochemical tracers in paleoenvironmental reconstruction (e.g., Wright et al., 1984; Grandjean-Lecuyer et al., 1993; Pan and Stauffer, 2000). These petrogenetic and paleoenvironmental applications all require understanding of the effects of crystal-chemical and external factors on the uptake of REEs in apatites. The crystal-chemical behaviors of the substitution(s) of REEs in fluorapatite, therefore, became the focus of this thesis work.

EPR spectroscopy is a powerful probe for the local structural environments of paramagnetic ions in minerals (Calas, 1988; Weil et al., 1994). Previous EPR studies of apatite-group minerals included Cr^{5+} and Mn^{2+}, in chlorapatite, fluorapatite and hydroxyapatite (Warren and Mazelsky 1970; Greenblatt, 1980; Pifer et al., 1983), and radiation defects in hydroxyapatite and carbonate apatites (Close et al., 1981; Elliott,

1994 and references therein). In addition, EPR study of Gd^{3+} centres, because of their significance in geology (e.g., McDonough & Frey, 1989; McKay, 1989; Grauch,1989) and laser technology (Elliott, 1994; Gruber et al., 1999 and references therein), has been widely performed for different minerals and synthetic compounds with various crystal symmetries and distinct local structure environments (e.g., Calas, 1988; Al'tshuler and Kozyrev, 1974). To the best of my knowledge, however, no results have been reported for the local structural environments of the Gd^{3+} centres and the hyperfine structure of $^{157}Gd^{3+}$ in single-crystal fluorapatite and which was the focus of this work.

1.2 Thesis Outline

This thesis reports on X-band (9.5 GHz) and W-band (95 GHz) electron paramagnetic resonance (EPR) spectroscopic studies on single crystals and powder samples of Gd-doped fluorapatite. The X-band EPR spectra display a well-resolved type of Gd^{3+} centre (electron spin S = 7/2) and suggest the presence of a second type of Gd^{3+} centre (Chapter 2). The latter is only partly resolved in the X-band EPR, but has been investigated in detail for fluorapatite crystals containing ~57 ppm Gd in a W-band EPR study (Chapter 3). Detailed analyses of the single-crystal X- and W- band EPR spectra allowed determination of the spin-hamiltonian of the two Gd^{3+} centres and their site assignments in the crystal structure of fluorapatite. The local structural information yielded new insight into the substitution mechanism(s) for the incorporation of Gd^{3+}, as a representative of the trivalent REEs, into fluorapatite.

The X- and W-band EPR spectra of the Gd-doped fluorapatite crystals did not show any evidence of hyperfine structures (HFS) of the two paramagnetic centres involving Gd^{3+} nuclides with both even and odd isotopes (^{152}Gd, ^{154}Gd, ^{155}Gd, ^{156}Gd,

^{157}Gd, ^{158}Gd and ^{160}Gd, where ^{155}Gd and ^{157}Gd have I = 3/2). This lack of HFS for the Gd-doped fluorapatite crystals was thought to be related to low natural abundances of the two odd isotopes relative to their even-isotope counterparts. Accordingly, fluorapatite crystals doped with ^{157}Gd-enriched Gd_2O_3 have been synthesized and used for a detailed investigation of the HFS of the Gd centres in this mineral (Chapter 4).

1.3 Crystal Structure of Fluorapatite

Fluorapatite crystallizes in space group $P6_3/m$ and point group 6/m, corresponding to proper rotation group C_6 relevant for the EPR spectroscopy. The crystal structure of fluorapatite is made up of Ca1 and Ca2 coordination-polyhedra linked with PO_4 groups to form a hexagonal network (Fig. 1.1). The F^- ions lie in columns parallel to the c axis, and each F anion is surrounded by six Ca2 cations (three at z = 0.25 and three at z = 0.75). The Ca1 polyhedron is nine-coordinated (i.e., six shorter bonds defining an approximate trigonal prism to anions O1 and O2, and three longer bonds to anions O3; Fig. 1.2a). The environment of Ca2 is an irregular CaO_6F polyhedron formed by a hemisphere of 6 oxygen atom capped by a F^- ion (Fig. 1.2b; Fleet et al., 2000b). The Ca2 site in end-member fluorapatite is characterized by a horizontal mirror plane normal to the c axis (point group m), which is magnetically equivalent to a two-fold rotation axis parallel to **c** (Weil et al., 1973).

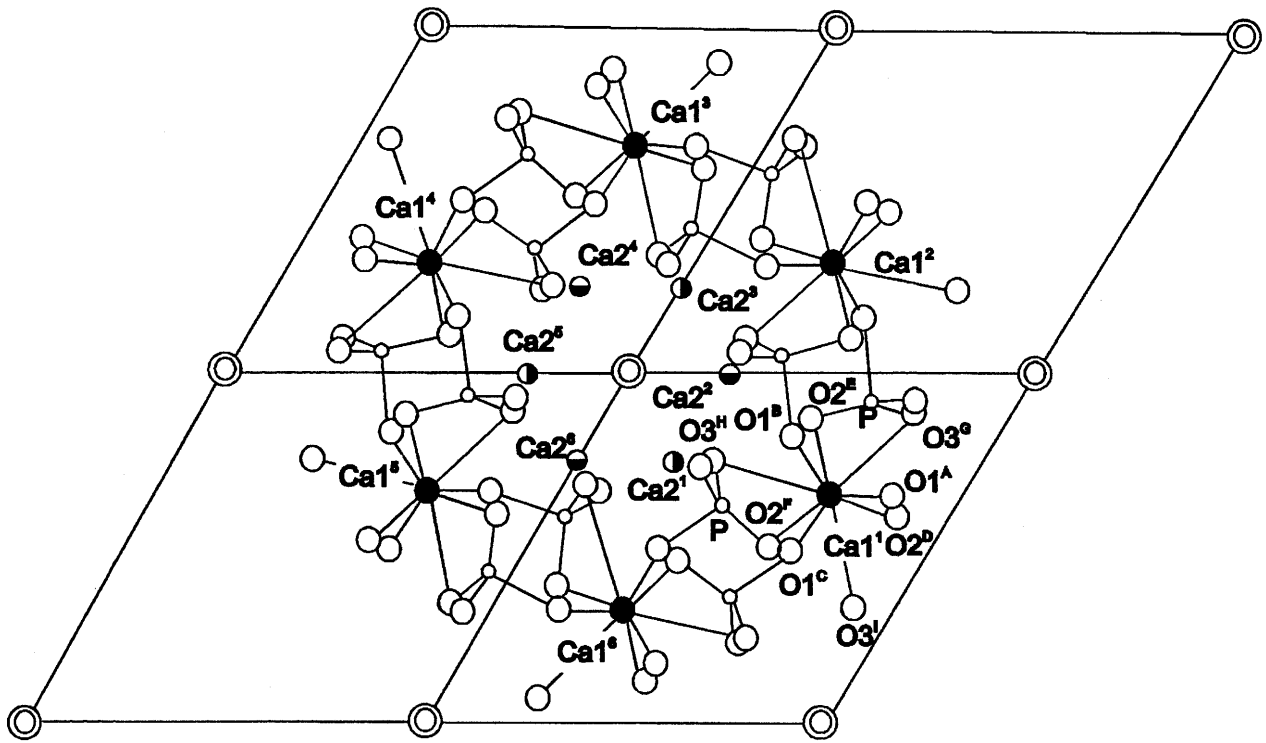

Figure 1.1. Projection (001) of the fluorapatite structure (after Hughes et al., 1989). Note the symmetry-related sites Ca1(labeled $Ca1^1$ to $Ca1^6$) and Ca2 ($Ca2^1$, $Ca2^3$ and $Ca2^5$ at z = 3/4; whereas $Ca2^2$, $Ca2^4$ and $Ca2^6$ are at z = 1/4). Also labeled are nine nearest-neighbor oxygen atoms (from $O1^A$ to $O3^I$) of the $Ca1^1$ site.

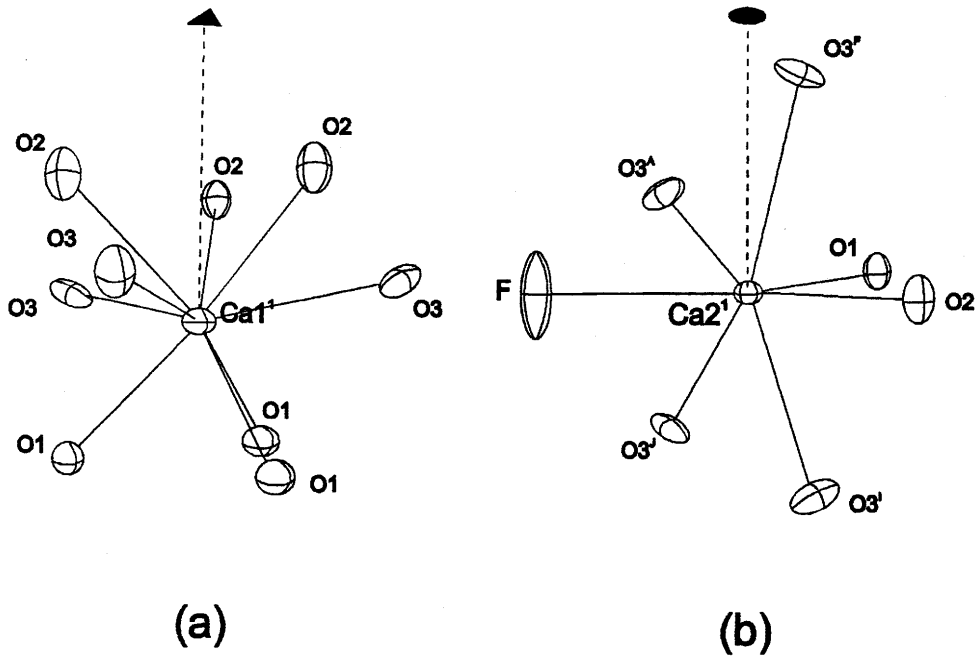

Figure 1.2. Local environments of the Ca sites in fluorapatite: (a) the nearest-neighbor environment of the $Ca1^{I}$ site. Note that the 3-fold axis (solid triangle) is parallel to the c axis; (b) the nearest-neighbor environment of the $Ca2^{I}$ site. Note that the horizontal mirror plane is magnetically equivalent to a vertical 2-fold rotation axis (solid ellipse) along the c axis.

CHAPTER 2

Local Structural Environment and Substitution Mechanism of the Gd^{3+} Centre 'a'

2.1 Introduction

The crystal chemistry of REEs in apatites, as in other Ca-rich minerals, is controlled largely by their accommodation in the Ca sites (Fig. 1.1; Fleet and Pan, 1995a; Pan and Fleet, 1996). Fluorapatite contains two types of Ca sites with distinct stereochemistry (Ca1, Fig. 1.2a; and Ca2, Fig. 1.2b; Hughes et al., 1989), both of which are able to accommodate REEs and a wide variety of other cations (e.g., Hughes et al., 1991; Fleet and Pan, 1995b; 1997a). Previous studies produced contradictory results in the site preference of REEs in apatites (e.g., Ca1, Urusov and Khudolozhkin, 1974; Ca2, Borisov and Klevtsova, 1963). More recently, high-precision x-ray structure refinement of natural and synthetic apatites revealed that REEs generally prefer the Ca2 site and that the site-occupancy ratios (REE_{Ca2}/REE_{Ca1}) decrease monotonically with atomic number through the 4f transition series (Hughes et al., 1991; Fleet and Pan, 1995b; Fleet et al., 2000a,b). Also, Gaft et al. (1997) assigned laser-induced time-delayed luminescence spectra of natural apatites to three distinct types of Eu^{3+} centres: two at the Ca2 site and one at the Ca1 site.

The present contribution reports on results of an X-band (9.5 GHz) electron paramagnetic resonance (EPR) spectroscopic study of single crystals and powder

samples of Gd-doped fluorapatite. Synthetic fluorapatite was used in this study because of the generally low abundances of Gd and the common occurrences of other paramagnetic impurities (e.g., Mn^{2+}) in natural crystals. The X-band EPR spectra display a well-resolved type of Gd^{3+} centre (electron spin S = 7/2;) and suggest the possible presence of a second type of Gd^{3+} centre (assigned as the Gd^{3+} centre 'b'), which is only partly resolved at this frequency but has been investigated in detail in fluorapatite crystals containing 57 ppm Gd in a W-band (94 GHz) EPR study (Ning Chen et al., 2001b). Detailed analysis of the single-crystal X-band EPR spectra allows determination of the spin-hamiltonian of the well-resolved Gd^{3+} centre 'a' and its site assignment in the crystal structure of fluorapatite. More importantly, the results of this EPR study provide important insight into the local structural environment of the centre 'a', which is not available from x-ray structure refinement. In addition, the local structural information yields new insight into the substitution mechanism(s) for the incorporation of Gd^{3+}, as a representative of the trivalent REEs, into fluorapatite.

2.2 Spin-hamiltonian

Gadolinium (Z = 64) includes both even and odd isotopes, but the latter have relatively low natural abundances (i.e., ^{155}Gd = 14.8% and ^{157}Gd = 15.7%, both having nuclear spin of I = 3/2). The spin-hamiltonian for the even isotopes of Gd (Mombourquette et al., 1986; McGavin, 1987; Weil et al., 1994) can be expressed as:

$$\mathcal{H}_S = \sum_{l_1,l_2} \sum_{l} \sum_{m=-l}^{+l} a_{l,m}^{l_1,l_2} \; T_{l,m}^{l_1,l_2}(\mathbf{B},\mathbf{S}), \qquad (1)$$

where the first factors are the coefficients of the double spherical tensor operators $T(\mathbf{B}, \mathbf{S})$. The latter can be expanded (Mombourquette et al., 1986) in terms of other (single) spherical tensor operators as follows:

$$T_{l,m}^{l_1,l_2}(\mathbf{B},\mathbf{S}) = \sum_{m_1,m_2} (2l+1)^{1/2}(-1)^{l_1-l_2-m} \begin{pmatrix} l_1 & l_2 & l \\ m_1 & m_2 & -m \end{pmatrix} T_{l_1,m_1}(\mathbf{B})\ T_{l_2,m_2}(\mathbf{S}). \qquad (2)$$

In Equations 1 and 2, l are even integers ranging from $|l_1-l_2|$ to l_1+l_2; here $l_1 \geq 0$ and $0 \leq l_2 \leq 2S$; m is equal to the sum of m_1 and m_2; m_k has values $-l_k, \ldots, +l_k$ (k = 1, 2). Terms with $l_2 = 0$ are of no spectroscopic interest. The term in Equation 1 with $l_1 = l_2 = 1$ can be expressed as the electronic Zeeman term $\beta_e \mathbf{B}^T \bullet \mathbf{g} \bullet \mathbf{S}$ (referred to as the BS term hereafter); here β_e is the Bohr magneton, $\mathbf{B}^T$ is the row vector of the external magnetic field (i.e., the Zeeman field), $\mathbf{g}$ is a 3×3 parameter matrix and $\mathbf{S}$ is the electron spin column vector operator. Here the superscript ^{T} indicates transposition of a column vector to the same vector expressed as a row vector, while the symbol • indicates the operation of a scalar product. The terms with $l_1 = 0$ and $l_2 = 2$ can be written as $\mathbf{S}^T \bullet \mathbf{D} \bullet \mathbf{S}$ (i.e., the S^2 term); here $\mathbf{S}^T$ is again a row vector and $\mathbf{D}$ is a traceless 3×3 parameter matrix representing the electronic quadrupole effect causing the seven-line fine structure of the Gd^{3+} EPR spectra (Fig. 2.1). The major contributions to this quadrupole effect are the electron-electron magnetic dipole interaction, the electronic exchange and the spin-orbit interaction, which cannot be differentiated experimentally by EPR. Moreover, crystal-field and covalency effects are also involved. Herein, matrices $\mathbf{g}$ and $\mathbf{D}$ are taken as being symmetric. The energy levels (line positions) of the fine structure will be shifted by the magnetic-field-independent high-spin terms of type S^4 ($l_1 = 0$, $l_2 = 4$) and

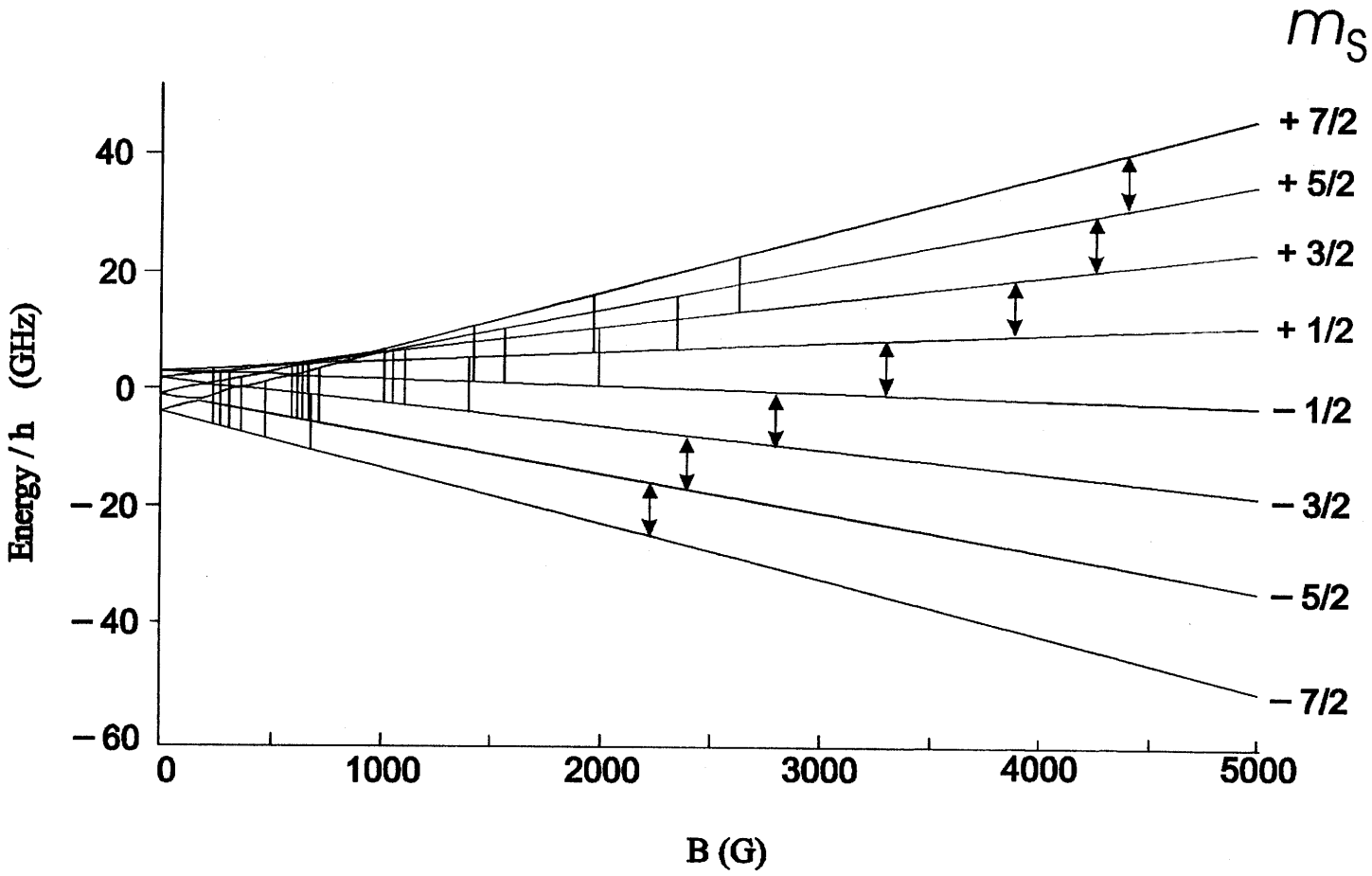

Figure 2.1a. Simulated energy levels for the Gd^{3+} centre 'a' in fluorapatite at **B//z** at the experimental frequency $\nu = 9.21258(6)$ GHz and temperature T = 295.0 K. The seven "allowed" transitions are labeled as single lines with arrows, and the "forbidden" transitions are labeled as single lines without arrows and have not been detected in X-bnad EPR experiments.

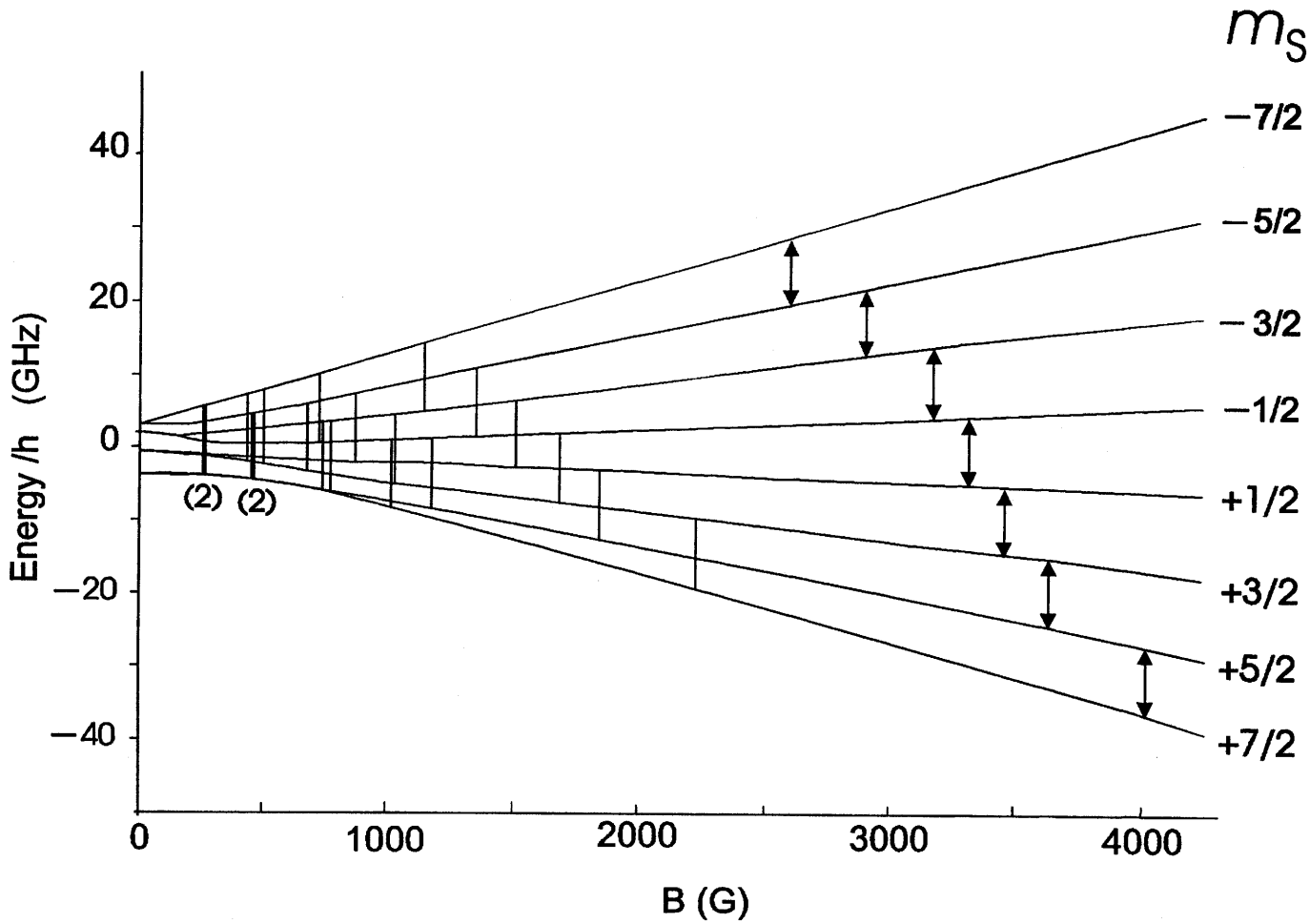

Figure 2.1b. Simulated energy levels for the Gd^{3+} centre 'a' in fluorapatite at **B//y** at the experimental frequency $\nu = 9.1966(2)$ GHz and temperature T = 293.5 K. The seven "allowed" transitions are labeled as single lines with arrows, and the "forbidden" transitions are labeled as single lines without arrows and have not been detected in X-bnad EPR experiments.

S^6 ($l_1 = 0$, $l_2 = 6$), as well as the magnetic-field-dependent terms of type BS^3 and BS^5 with $l_2 = 3$ and 5 (i.e., $l = 2$, 4 and 4, 6, respectively). A detailed discussion on the form of the "generalized" spin-hamiltonian can be found in Buckmaster et al. (1972), Al'tshuler and Kozyrev (1974) and in Mombourquette et al. (1986).

2.3 Experimental Methods

2.3.1 Synthesis and characterization of fluorapatite crystals

Synthesis of Gd-doped fluorapatite crystals followed the flux method of Prener (1976). Briefly, starting materials of high-purity chemicals (≥ 99.99%), including CaO obtained from decomposition of $CaCO_3$ at 900 °C, and P_2O_5, CaF_2 and Gd_2O_3, from the Sigma-Aldrich Chemical Company, were weighed and mixed thoroughly to form the composition of fluorapatite having approximately 1 wt% Gd_2O_3. This mixture (27.5 g) together with flux materials (22.5 g CaF_2) were then placed in a tightly-covered 50 mL platinum crucible. Synthesis was carried out under atmospheric pressure in a Thermolyne Muffle Furnace 46100 equipped with a programmable controller, at the Department of Geological Sciences, University of Saskatchewan. The mixture was first heated to 1375 °C and held there for 24 hours to ensure complete melting and homogenization, and was then cooled down to 1220 °C at a rate of 2 °C/hr and quenched in water. The resulting products typically contained several large crystals (up to 1 cm in length and ≥ 1 mm in diameter) and numerous smaller grains of fluorapatite in a quenched melt of CaF_2. The CaF_2 was removed by boiling in an aqueous 20% solution of $Al(NO_3)_3 \cdot 9H_2O$.

The large crystals of fluorapatite typically are in the form of hexagonal prisms and are terminated by $\{1\ 0\ \bar{1}\ 1\}$. Most of these contain inclusions of CaF_2 flux materials, which occur as small rods parallel to the c axis. A few large crystals that were clear under microscopic examination and thus thought to be free of melt inclusions were

selected for further optical characterization and electron microprobe analysis. Back-scattered electron imaging and quantitative analyses on a JEOL JXA-8600 Superprobe, equipped with one energy-dispersion and three automated wavelength-dispersion spectrometers, allowed the selection of compositionally homogeneous crystals (i.e., 1.2±0.2 wt% Gd_2O_3) for the EPR measurements.

2.3.2 Single-axis crystal holder

A single-axis crystal holder, with internal powder (concentrated free radical 2,2-diphenyl-1-picrylhydrazyl: DPPH), was designed for X-band EPR work at the University of Saskatchewan. For X-band work in this thesis, DPPH powder was adopted as the standard for the EPR line-position calibration. The experiment indicated that for any observed sample (e.g., Gd^{3+}-doped powder or single-crystal samples of fluorapatite) containing even a speck of DPPH, the single EPR line from DPPH was strong enough to swamp the signal of the actual sample being observed (e.g., signal of Gd^{3+}). This effect is also likely to happen for other EPR work involving DPPH as a standard. Furthermore the DPPH crystals show appreciable g anisotropy ($0 < \Delta g < 0.001$; Yablokov, 1960), as well as of the linewidth, so that it is not safe to reduce the quantity of DPPH used (i.e., when rotating a crystal sample relative to the applied magnetic field **B**).

In this situation, a single-axis crystal holder was developed with self-contained DPPH as standard for line-position calibration in X-band EPR work. The kernel of the design is that the holder must contains enough quantity of DPPH powder to eliminate the anisotropic effects from g and lineshape, and at the same time the signal intensity

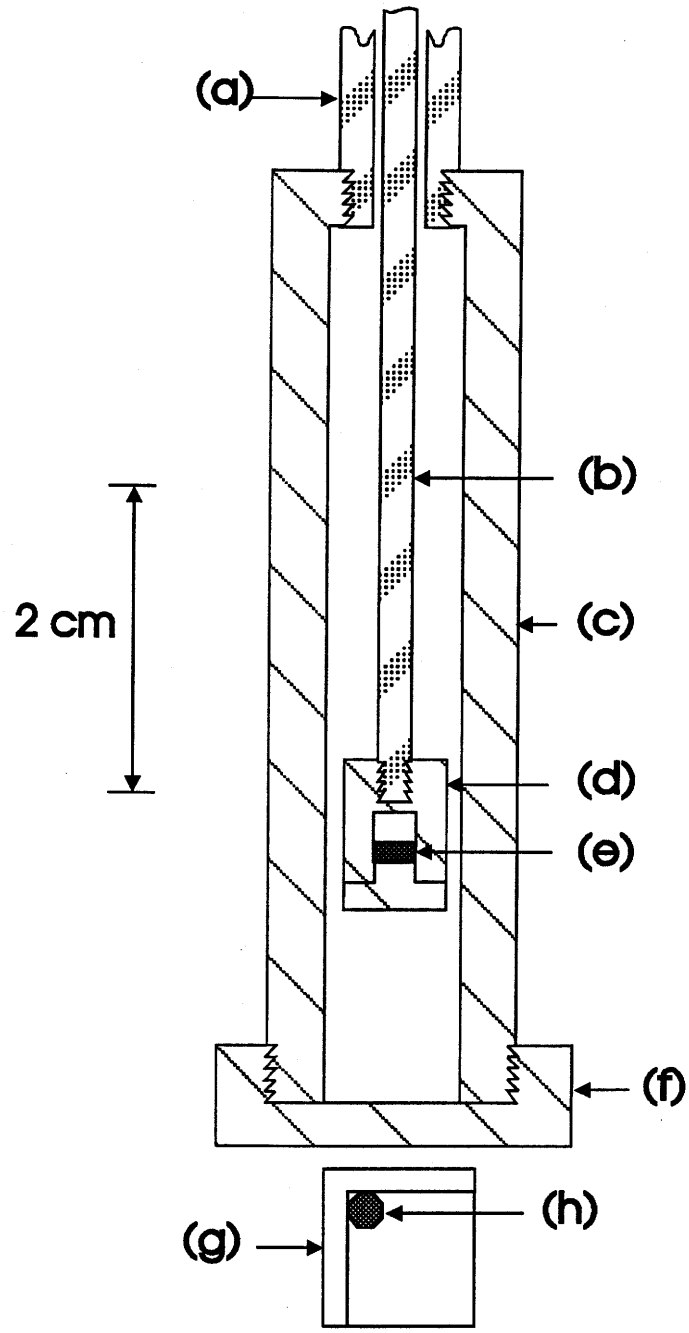

Figure 2.2. The single-axis crystal holder containing DPPH standard.

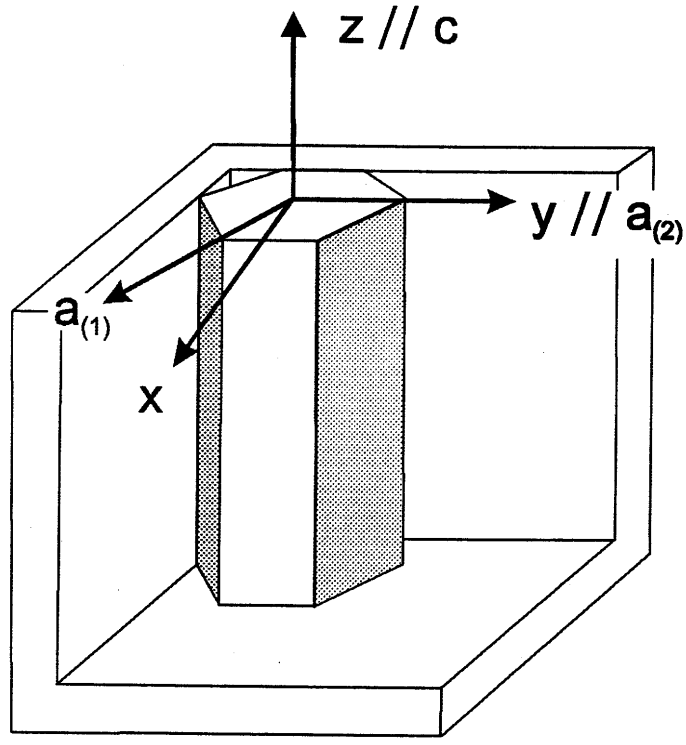

Figure 2.3. Alignment of the fluorapatite crystal on an acrylic three-sided holder (Chen et al., 1999). Note the relationships between the three orthogonal rotation axes (x, y and z) of the holder's cube faces and the crystallographic axes ($a_{(1)}$, $a_{(2)}$ and c).

from DPPH needs to be adjustable to make it not too strong compared to the signal(s) from the paramagnetic species under study.

Figure 2.2 shows the following components of the holder. Threaded brass tube (a) was fitted to a 360° dial mounted above (ca. 20 cm) the resonator. The brass tube then holds a slip-fit rod (b) and is designed to hold a cylindrical virgin teflon jacket (c). The jacket is screwed onto the bottom end of the tube and hollowed to contain a two-piece teflon DPPH standard holder (d) screwed to the bottom of the rod (b). The standard holder contains DPPH powder. The rod is movable up and down, and the length of the rod extruding from the top of the tube (a) allows measurement of the position of the standard holder relative to the resonator. The teflon bottom plate (f), screwed onto the jacket (c), has a flat bottom perpendicular to the axis of the holder. A three-sided acrylic holder (g), with right angles between their sides (error $\leq 0.5°$), was used to hold the single-crystal samples (h), and was attached to the bottom of the single-axis crystal holder (f).

The single-axis crystal holder solved the difficulties concerning application of DPPH as standard. The fairly massive amount of DPPH powder (ca. 0.2 mg) guarantees adequate orientational averaging of the large amount crystallites included, and thus the DPPH sample can act as completely isotropic. Secondly, when the standard is needed, the DPPH standard could be located at an appropriate position (i.e., almost out of the resonator) so as to obtain simultaneously only a suitably small standard signal and the signal coming from the paramagnetic species under investigation. If only the signal coming from the paramagnetic species under study is wanted, the standard can be simply

moved out of the cavity. Therefore, observations can be made with or without standard to meet the special experimental requirements.

2.3.3 X-band EPR experiments

Single-crystal X-band EPR spectra of the Gd-doped fluorapatite were obtained on a Bruker ESP300 spectrometer with a field modulation frequency of 100 KHz, at the Department of Chemistry, University of Saskatchewan. Each selected crystal was mounted on the acrylic three-sided holder (Fig. 2.3; error in cubicity = ±0.5°) by using the Laue method (Amoros et al., 1975). The x-ray diffraction analysis also confirmed that the selected crystals of fluorapatite were free of twinning. The holder was then attached to the flat end of a cylindrical teflon jacket of a goniometer containing an adjustable EPR standard (Fig. 2.2; Chen et al., 1999). This made it possible for simultaneous EPR measurement and standardization by use of DPPH. Field-swept EPR experiments were performed at 5° and 10° intervals with the magnetic field **B** in three orthogonal rotation planes by consecutively attaching the three sides of the holder to the goniometer by use of an appropriate vacuum grease (Chen et al., 1999). In these three rotations, the axes **y** and **z** of the ideal experiment system are chosen along the crystallographic axes **a** and **c**, and thus the direction of the axis $\mathbf{x} = \mathbf{y} \otimes \mathbf{z}$ is defined. However, the axes of the actual experimental system are not exactly equal to the axes of the ideal system, and therefore were referred to as **x'**, **y'**, and **z'** (i.e., the rotation planes x'y', y'z' and x'z'; Figs. 2.4 and 2.5). All single-crystal X-band spectra were collected at ~295 K. The spectral resolution was 2.0 G (i.e., 1024 field data points over 2000 G in

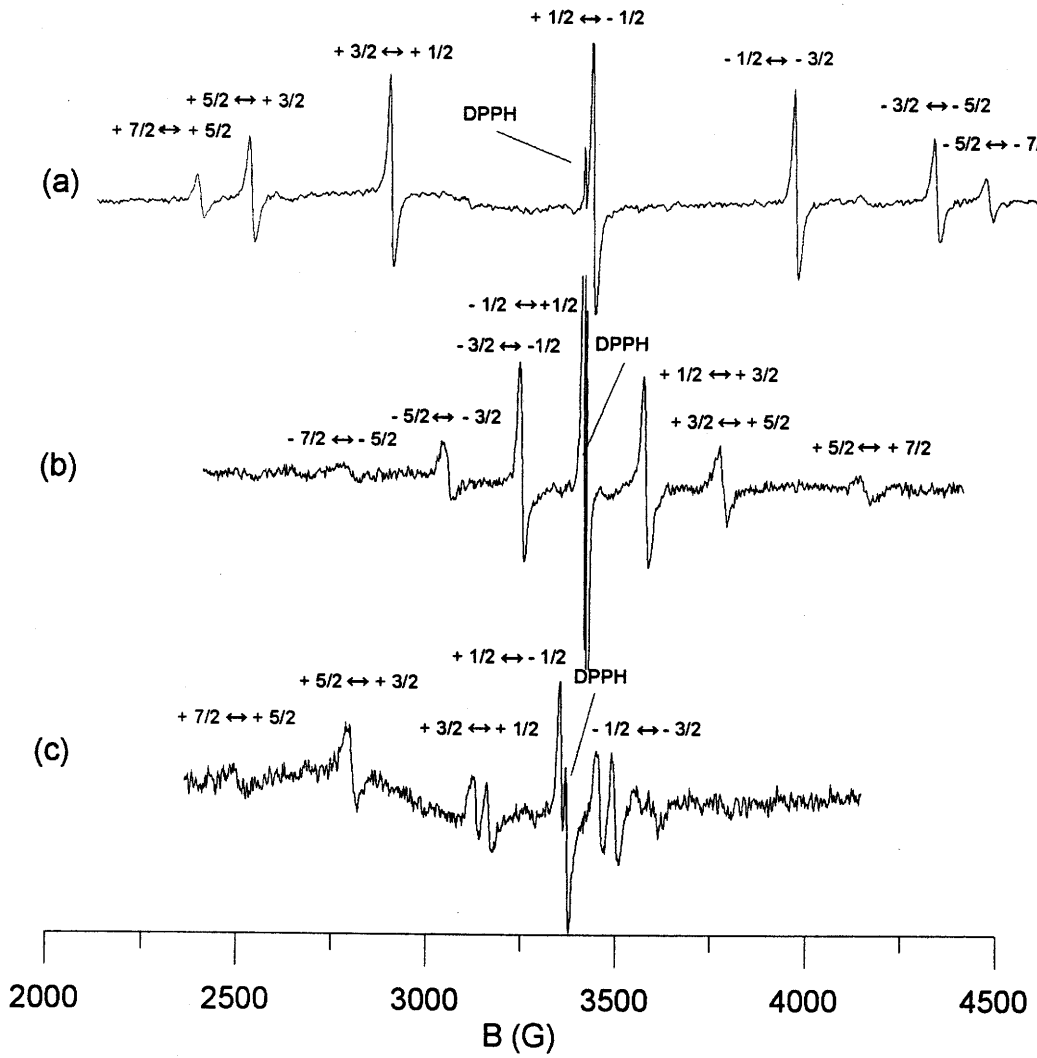

Figure 2.4. Single-crystal spectra of the Gd-doped fluorapatite: (a) $\mathbf{B}//\mathbf{z}'$ and $\mathbf{B}_1//\mathbf{x}'$, at ν = 9.21258(6) GHz and T= 295.0 K; here $\mathbf{B}_1$ is the excitation field; (b) $\mathbf{B}//\mathbf{y}'$ and $\mathbf{B}_1//\mathbf{z}'$, ν = 9.1966(2) GHz and T= 293.5 K; and (c) $\mathbf{B}$ located in the x'y' plane and 35° away from the axis z', at ν = 9.1857454(2) GHz and T = 260.0K. Note that a magnetic site splitting is visible for the transitions $-1/2 \leftrightarrow +1/2$ and $+3/2 \leftrightarrow +1/2$ in the x'z' plane.

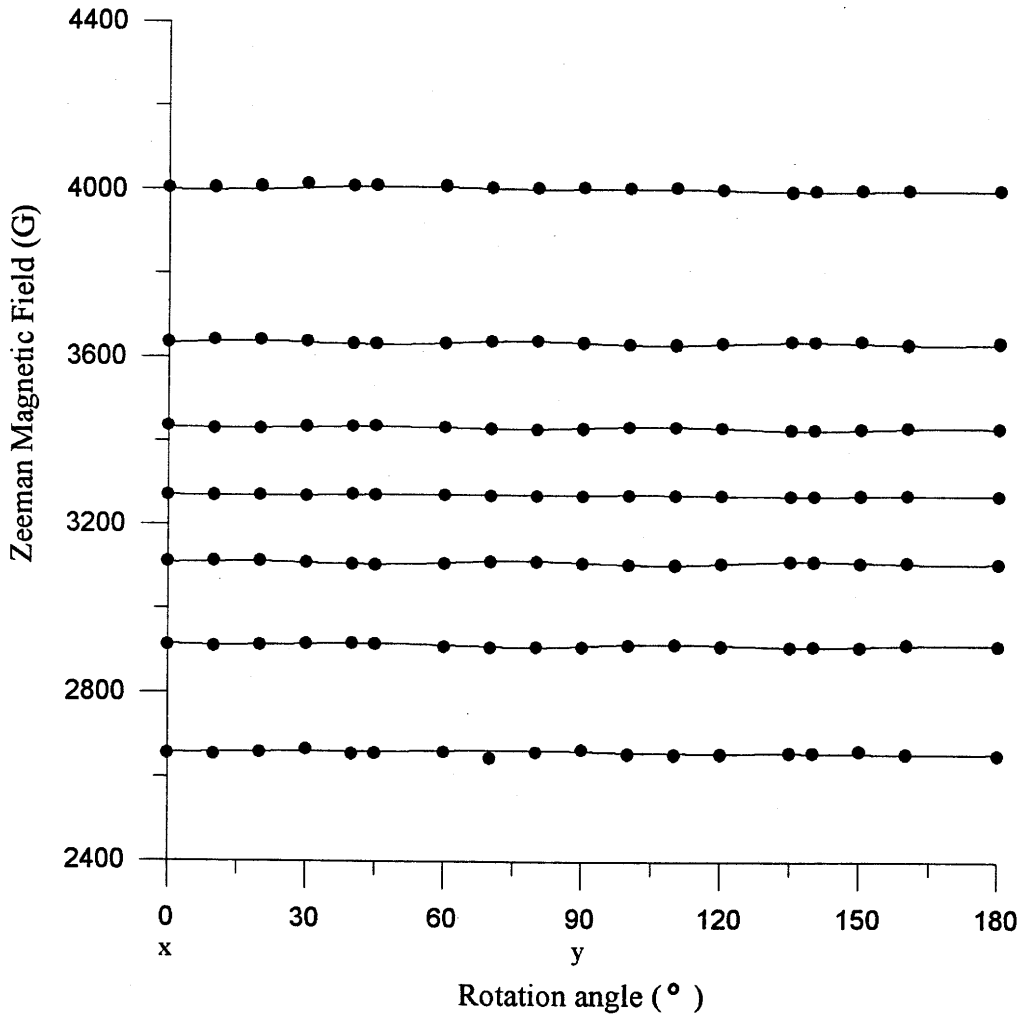

Figure 2.5a. Angular dependence of line positions ("roadmap") of the EPR spectrum for Gd^{3+} centre 'a' in fluorapatite with the Zeeman field **B** rotated in the plane x'y'. Effectively, each curve is six-fold degenerate. The solid circles indicate the observed data points. The solid line is the angular dependence of the line positions predicted by the spin-hamiltonian obtained for the Gd^{3+} centre 'a'.

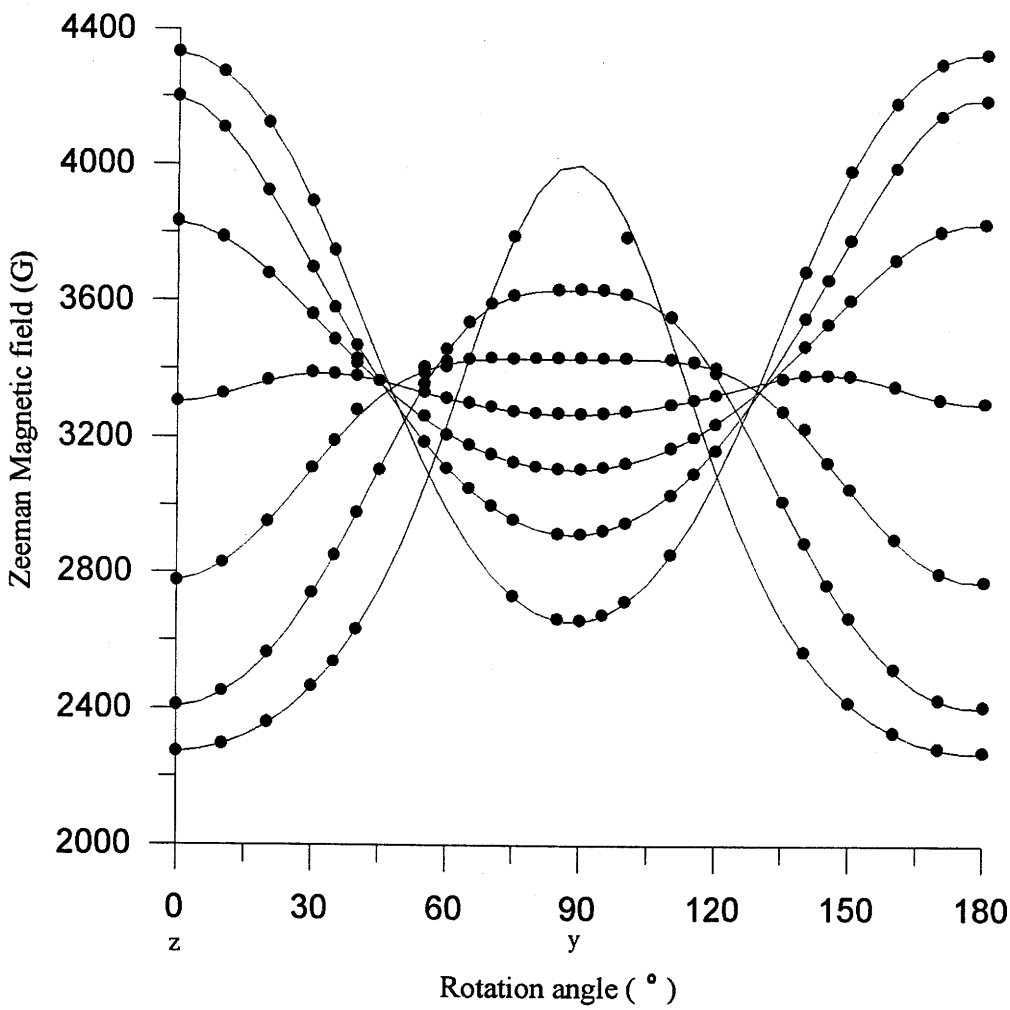

Figure 2.5b. Angular dependence of line positions ("roadmap") of the EPR spectrum for a Gd^{3+} centre 'a' in fluorapatite with field **B** rotated in the plane y'z'. Effectively, each curve is six-fold degenerate. The solid circles indicate the observed data points. The solid lines are the angular dependence of the EPR line positions predicted by the spin-hamiltonian obtained for Gd^{3+} centre 'a'.

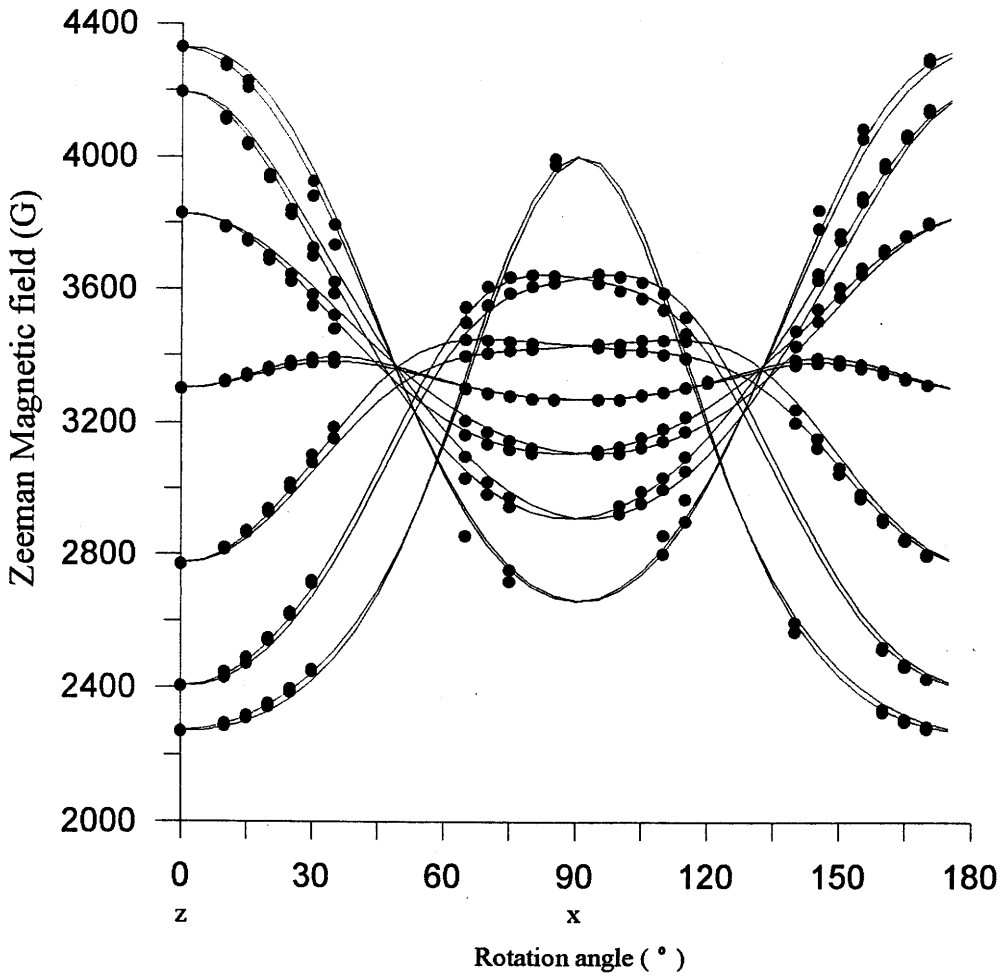

Figure 2.5c. Angular dependence of the line positions ("roadmap") of the EPR spectrum for Gd^{3+} centre 'a' in fluorapatite with the Zeeman **B** rotated in the the plane x'z'. Effectively, each curve is triply degenerate. The solid circles indicate the observed data points. The solid lines are the angular dependence of the EPR line positions predicted by the spin-hamiltonian obtained for for the Gd^{3+} centre 'a'.

each spectrum), except 0.1 G (1024 points over 100 G) for the three most central (narrowest) lines among the seven. The average microwave frequencies were 9.199(1) GHz for the x'y' plane, 9.205(2) GHz for the y'z' plane and 9.187(2) GHz for the x'z' plane. The numbers of line-position data points collected were 127, 285 and 127 for **B** in planes x'y', x'z' and y'z', respectively.

Single-crystal Q-band (36 GHz) and W-band (94 GHz) EPR spectra of synthetic fluorapatite containing approximately 57 ppm Gd were obtained at 287 K on a Mark-II spectrometer at the Illinois EPR Research Centre (IERC), University of Illinois at Urbana-Champaign to test the results for X-band EPR described herein (Chapter 3).

Powders of the Gd-doped fluorapatite were obtained by grinding single crystals in an agate mortar and were investigated on the Bruker ESP300 X-band spectrometer at both 295 and 120 K. Except for differences in the absolute intensities of signals, the two spectra are indistinguishable in both the peak positions and peak relative intensities.

2.4 Results and Discussions

2.4.1 X-band EPR spectra

The single-crystal X-band EPR spectra of the Gd-doped fluorapatite mostly consist of seven anisotropic lines from the primary "allowed" transitions (Figs. 2.1 and 2.4), consistent with the presence of primarily a single Gd^{3+} paramagnetic centre (the centre 'a') with electron spin of 7/2. The X-band powder spectra of the Gd-doped fluorapatite at 120 and ~295 K are also consistent with presence of the Gd^{3+} centre 'a' (Fig. 2.6). A few single-crystal X-band EPR spectra with **B** close to the y axis, however, contain additional lines at the low- and high-magnetic field regions, which have been shown by a separate EPR study at higher frequencies (i.e., Q- and W-bands at IERC)

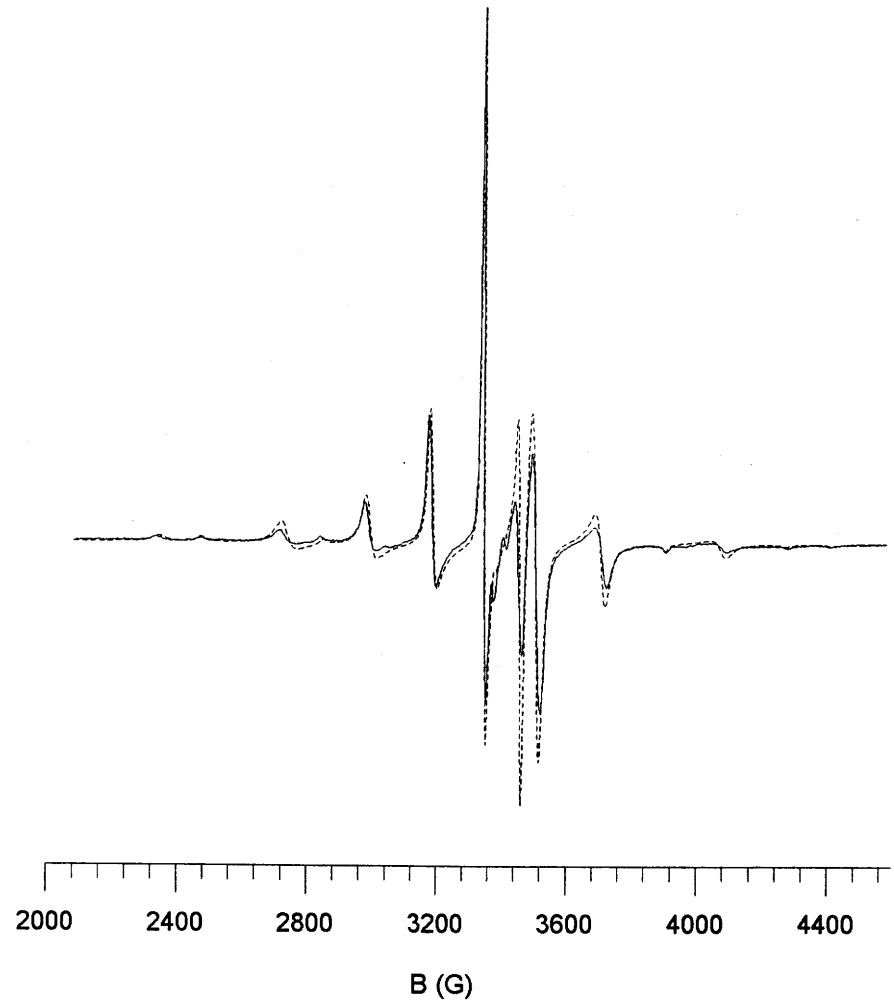

Figure 2.6. Observed (solid line) and simulated (dashed line) powder EPR spectrum of the Gd-doped fluorapatite for centre 'a' at the experimental frequency ν = 9.397523(3) GHz and temperature T = 120 K [simulation: lorentzian lineshape and various effective linewidths for the various "allowed" transitions].

caused by a second major Gd^{3+} centre (the Gd^{3+} centre 'b'; Chapter 3). The Q- and W-band spectra showed that the Gd^{3+} centre 'b' has a large fine structure and hence is generally not detectable in the X-band experiments. Moreover, quantitative analysis of the single-crystal W-band spectra of the centre 'b' revealed that it corresponds to occupancy of Gd^{3+} at the Ca1 site (Chapter 3).The lines from the "forbidden" transitions of centre 'a' (Fig. 2.1) are not observed in the X-band experiment and have been shown by simulation to be very weak (up to only 0.2% of those of the "allowed" transitions). Figure 2.5 shows the angular dependence of the primary spectra. Line-position crossovers of the EPR transitions occur with **B** in the x'z' and y'z' planes but not in the x'y' plane. A magnetic site splitting into 2 lines was detected with **B** in the plane x'z' (Fig. 2.4c).

The absence of any hyperfine structures in the X-band EPR spectra of the Gd-doped fluorapatite is probably related to the low natural abundances of ^{155}Gd and ^{157}Gd relative to the even isotopes. At natural abundances, the intensity of each individual hyperfine line of ^{155}Gd or of ^{157}Gd is nearly twenty times lower than that of the single EPR line of the even isotopes. Another factor may be peak interference between the the ^{155}Gd and ^{157}Gd spectra, since only small difference is to be expected in the hyperfine parameters of these isotopes (Weil et al., 1994; Table G.4). Furthermore, appreciable nuclear quadrupole effects are known to be present, which has been estimated for the single-crystal spectrum for $^{157}Gd^{3+}$-doped fluorapatite, and the spin-hamiltonian terms of type **A** and **g**(n) were also estimated (see Chapter 4). At any rate, simulation of individual peaks at field orientations where no magnetic-site splittings are present yielded well-fitting lorentzian lines (see below) with no other satellite peaks visible in the difference spectra.

2.4.2 EPR lineshapes and linewidths

The basic EPR lineshape is of the lorentzian type, as confirmed by simulation of several of the EPR spectral lines. These were done for the transition between spin-projection eigenvalues m_S: −1/2 and +1/2 with the Zeeman field **B//z'** and the excitation field $\mathbf{B}_1$**//x',** at a frequency of 9.200385 GHz and at a temperature of 295.0 K, using a simulation linewidth (max-min of the 1st derivative) of 6.41 G. The same lorentzian result was obtained for the transition +3/2 ↔ +1/2, with **B//x'** and $\mathbf{B}_1$**//z'** at a frequency of 9.197972 GHz and at a temperature of 293.0 K, as well as for the same transition with **B//y'** and $\mathbf{B}_1$**//z'** at a frequency of 9.200101 GHz and at a temperature of 294.0 K, using a linewidth of 11.5 G for both.

Because of the C_6 effective crystal symmetry, Gd^{3+} ions at the six symmetry-related sites (Fig. 1.1) contribute as many as 6 "symmetry-related" EPR lines for each transition. For **B//z',** approximate superposition of all 6 lines is observed and has also been proved by the single-crystal spectrum simulation with all of the six symmetry-related sites included. Therefore, the inherent EPR linewidth (6.41 G) is detected here. The inherent linewidth may arise from D-strain effects (distributions of the spin-hamiltonian parameters, especially in **D**, due to crystal imperfections; Wenzel and Kim, 1965; Lee and Brodbeck, 1977) and from a mosaic-structure effect (small crystallites with their axes **c** slightly away from the average axis **c** of the crystal sample; Shaltiel and Low, 1961; Wenzel and Kim, 1965; and Lee and Brodbeck, 1977), and possibly also from superhyperfine interactions between the Gd cation and its next-nearest-neighbor nuclides (e.g., ^{19}F and ^{31}P in adjacent polyhedra).

The experimental results indicate that the linewidths are a function of transitions (between $m_S \leftrightarrow m_S+1$, $-7/2 \leq m_S \leq 5/2$) and increase with increasing $|m_s|$. If the line position splitting (due to strain and mosaic effects, etc.) is not sufficiently large to be resolved, then the result is line broadening. This effect can be qualitatively explained by use of second-order perturbation theory (Weil et al., 1994; p.189). An expression for the line splitting can be derived from the equation of the second-order energies, and shows that the positional splitting (determined by the matrices **g** and **D**) is proportional to $(2m_S+1)m_S$. Therefore, for a given strength of the strain and mosaic effect, the linewidths increase with $|m_S|$. This agrees with the X-band observations.

At all field orientations other than **B//z**, partial degeneracy (splitting into 2, 3 or 6 lines) is present but not necessarily resolved. Thus, an effective linewidth greater than the inherent one is generally observed. This has been proved by the single-crystal spectrum simulation, in which all symmetry-related sites were included, showing that there is a weak site-splitting effect even in the plane x'y'. This splitting is caused mainly by the slight deviation of the orientation of the principal direction $\mathbf{D}_3$ from the c axis.

The effective linewidth in the plane x'y' is approximately isotropic. This linewidth (e.g., for $-1/2 \leftrightarrow +1/2$) in the y'z' plane has a minimum of 6.4 G when **B//z'** and is 7.4 G when **B//y'**. The lineshape thus represents an effective lineshape exhibiting the contribution from all unresolved site splittings and strains. With **B** in the planes y'z' and x'z', the linewidths are anisotropic due to the (line-position) contributions arising from the different magnetic sites. The effective linewidths in the x'z' and y'z' planes were found to be linear with the magnetic-site-splitting line positions predicted by the spin-hamiltonian obtained in this study. The same effect occurs in the plane x'y'.

2.4.3 Spin-hamiltonian optimization and EPR data simulation

The optimization of spin-hamiltonian parameters by use of a non-linear least-squares algorithm, determination of the energy eigenvalues by matrix diagonalization, angle corrections for the Zeeman-field directions and the simulation of X-band EPR spectra were all performed by using the software package EPR-NMR (Mombourquette et al., 1996). Initially an effective C_2 crystal symmetry was assumed during the spin-hamiltonian optimization because of the magnetic site splitting observed in the x'z' plane (Figs. 2.4c and 2.5c). Afterwards, all of the spectrum fittings and simulations were performed using C_6 symmetry to match the actual magnetic crystal symmetry.

Two types of computations were performed: a) optimization of the spin-hamiltonian parameters, and b) calibrations of the crystal alignments in the three rotations. During the process of optimization, separate fitting for each of the spin-hamiltonian terms [i.e., the BS term (**g** matrix), the S^2 term (**D** matrix) and the terms of type BS^3, S^4, BS^5 and S^6] and the Zeeman field directions, as well as simultaneous fitting for all terms were performed iteratively. In each fitting step, iteration was continued until no changes at the last decimal point (the machine accuracy) of the root-mean-sum-of-squares of weighted differences (RMSD) between the calculated and observed line positions. Different weighing factors were adopted for the various transitions, according to the estimated accuracy of each line-position measurement. Thus, the data points of the central lines and the lines away from the transition-crossing regions were weighted higher than those of the outer lines and the lines within the transition-crossing regions (Figs. 2.5b and 2.5c). The final RMSD for line positions is 2.7 G, which is less than half of the average linewidth for the central line ($-1/2 \leftrightarrow +1/2$) of the observed spectra.

The errors in the alignment of the crystal were estimated after EPR measurement by using the software package EPR-NMR. The normals to the planes x'y', x'z' and y'z' were found to be ($\theta = 0.362°$, $\phi = 1.050°$), (89.973°, 90°), and (90°, 0°), respectively. Note that no error was detected for the y'z' plane. The final spin-hamiltonian parameters were expressed in the ideal reference system xyz [Tables 2.1(polar coordinates) and 2.2].

As shown below, the six symmetry-related matrices **g** and **D** (effective magnetic point group C_6) of the centre 'a' (corresponding to centres denoted by 'a^1', 'a^2', ..., 'a^6', respectively) can be assigned as the occupancy of the Gd^{3+} ions at the six symmetry-related Ca2 sites (i.e., the sites $Ca2^1$, $Ca2^2$, ..., $Ca2^6$, respectively, Fig. 1.1). The matrices **g** and **D** for the centre 'a^1' (corresponding to a Gd^{3+} ion at the site $Ca2^1$; Fig. 1.2) are given in Table 2.1, and the corresponding parameters for the S^4, S^6 and BS^3 terms are summarized in Table 2.2.

The contributions to the parameter optimization from individual terms of the spin-hamiltonian were estimated by artificially setting the parameters of each term to be zero, while all other terms were kept to be those of the optimized results. The terms BS^3, S^4, BS^5 and S^6 contributed to an improvement of the RMSD by 0.34, 50.31, 0.10 and 0.10 G, respectively. The calculated parameters for the term BS^3 have a magnitude of 10^{-5} (Table 2.2). The parameters for the term BS^5, of magnitude of 10^{-7} G, are not reported herein. The parameters for the term BS^7 are expected to be even smaller and therefore were not included in the optimization.

TABLE 2.1 The principal values and directions of matrices **Y** = **g** and **D** (and values of D and E) at 294.8(13) K for the Gd^{3+} centre 'a'. The estimated errors are given in parentheses.

	Matrices **Y**			k	Principal values Y_k	Principal directions θ_k (°)	φ_k (°)
	1.9914(2)	–0.0003(2)	0.0003(2)	1	1.9916(2)	73(8)	345(7)
g		1.9900(2)	–0.0003(2)	2	1.9903(2)	14(2)×10	5(2) ×10
			1.9902(2)	3	1.9898(2)	6(2)×10	9(1) ×10
In magnetic-field units:							
$\mathbf{D}/g_e\beta_e$ (G)	67.07(5)	0.06(6)	6.23(7)	1	67.37(6)	88.1(1)	36(8)
		67.13(6)	2.83(8)	2	67.06(6)	90.4(3)	125(8)
			–134.19(4)	3	–134.43(4)	1.94(2)	204.4(7)

$D/g_e\beta_e = 201.64(4)$ G, $E/g_e\beta_e = 0.15(4)$ G [a]

[a] $D = 3D_3/2$, $E = (D_1 - D_2)/2$ (Weil et al., 1994)

TABLE 2.2 Parameters of the high-spin terms of type S^4, S^6 and BS^3 at 294.8(13) K for the Gd^{3+} centre 'a'. For indices l_1, l_2, l, m_2 and m as well as symbol $g_{l,m,3}$, see Mombourquette et al., 1986.

S^4 ($l_1 = 0$)		S^6 ($l_1 = 0$)		BS^3 ($l_1 = 1$)		
M_2	$B_{l_2=4}^{m_2}$ [a] (G)	m_2	$B_{l_2=6}^{m_2}$ [a] $\times 10^{-4}$ (G)	l	m	$g_{l,m,3}$ $\times 10^{-5}$
0	0.1568(4)	0	−4.6(3)	2	0	−2.6(7)
1	−0.098(4)	1	10(4)	2	1	−1.3(7)
2	−0.005(2)	2	2(2)	2	2	3.2(9)
3	−0.02(2)	3	−4(7)	2	−1	−7(7)
4	−0.005(2)	4	−1(3)	2	−2	−7(6)
−1	−0.002(4)	5	−25(2)	4	0	−1.6(8)
−2	0.006(3)	6	10(3)	4	1	−5(4)
−3	0.59(2)	−1	−4(3)	4	2	−4(1)
−4	0.006(4)	−2	4(4)	4	3	−3(9)
		−3	−49(8)	4	4	8.2(9)
		−4	−5(4)	4	−1	−4(4)
		−5	47(2)	4	−2	2(8)
		−6	−31(4)	4	−3	−10(9)
				4	−4	−2(1)

[a] Conventional Stevens parameters (Mombourquette et al., 1986).

Figures 2.1a and 1b show that the calculated energy levels for **B//z'** and **B//y'** are in close agreement with the results in our EPR experiments. The "allowed" transitions ($|\Delta m_S| = 1$) occur in magnetic field regions mostly different (below) those occupied by the "forbidden" transitions ($|\Delta m_S| > 1$). The simulated and observed single-crystal spectra, for example with **B//z'** (Fig 2.8a) and **B//y'** (Fig. 2.8b), are in excellent agreement. Here the central line positions (i.e., transition $+1/2 \leftrightarrow -1/2$) of the two spectra agree within the resolution limit.

Figure 2.5 shows that the observed line-position roadmaps of the three orthogonal crystal rotations are in agreement with the calculated ones, and that the magnetic-site splittings in the x'z' plane are successfully reproduced. Similarly, the validity of the calculated spin-hamiltonian parameters has been confirmed by the excellent matches between the simulated powder spectrum with the observed one (Fig. 2.6). Furthermore, the spin hamiltonian from the present X-band EPR study has been shown to give excellent predictions for the line positions of the Gd^{3+} centre 'a' at W-band (see Fig. 3.2.; Chapter 3). To the best of our knowledge, this is the first demonstration for a successful prediction of the W-band EPR spectrum by the spin-hamiltonian obtained from X-band experiments for the Gd^{3+} nuclide occupying the Ca2 site.

The three principal values of **g** for 'a' are almost equal to each other and are slightly smaller than the free-electron value, but in fact are distinct (i.e., rhombic local symmetry). These g values are typical of Gd^{3+} (Al'tshuler and Kozyrev, 1974, App.

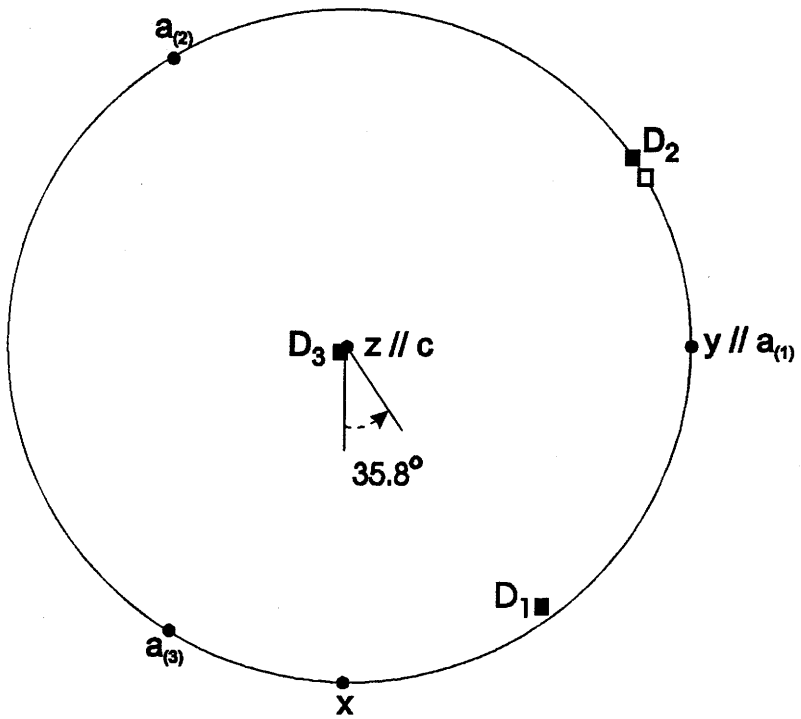

Figure 2.7. Stereographic projection illustrating the principal axes (see Table 1) of the electronic quadrupole matrix **D** for the Gd^{3+} centre 'a'. Note that the principal direction of D_3 is almost parallel to the c axis. Here solid squares are the principal directions of D_i (i = 1, 2 and 3). The solid circles are directions of the axes of of crystallograpy and experimental system. The open square is a a horizontal bisector of O3 - Ca2 - O3.

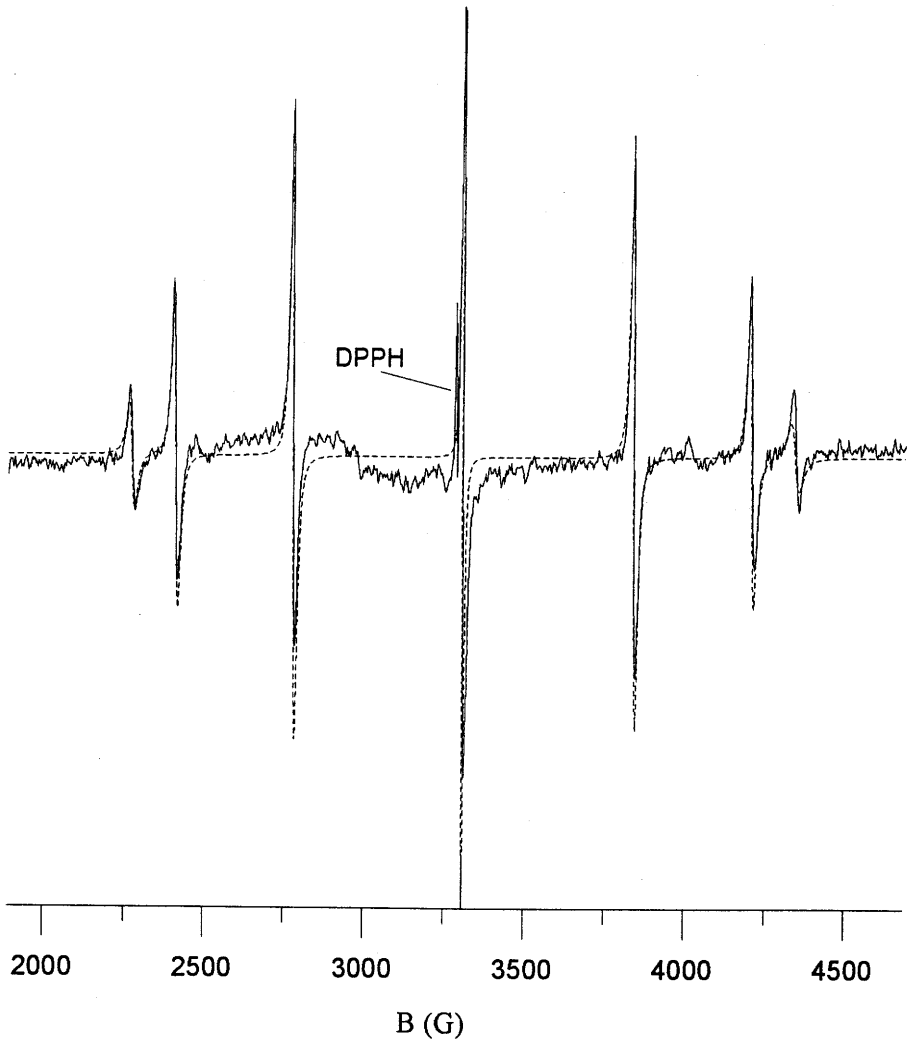

Figure 2.8a. Observed (solid line) and simulated (dashed line) single-crystal spectrum of Gd^{3+} in fluorapatite with $\mathbf{B}//\mathbf{z}$ and $B_1//\mathbf{x}$, at $\nu = 9.2126$ GHz and T = 295 K. The linewidths (G) used in the simulation for different transitions are 17.5 ($-7/2 \leftrightarrow -5/2$), 15.3 ($-5/2 \leftrightarrow -3/2$), 13.0 ($-3/2 \leftrightarrow -1/2$), 6.4 ($-1/2 \leftrightarrow +1/2$), 13.2 ($+1/2 \leftrightarrow +3/2$), 15.4 ($+3/2 \leftrightarrow +5/2$) and 19.8 ($+5/2 \leftrightarrow +7/2$), respectively. The lorentzian lineshape was used in the simulation (see text for explanation).

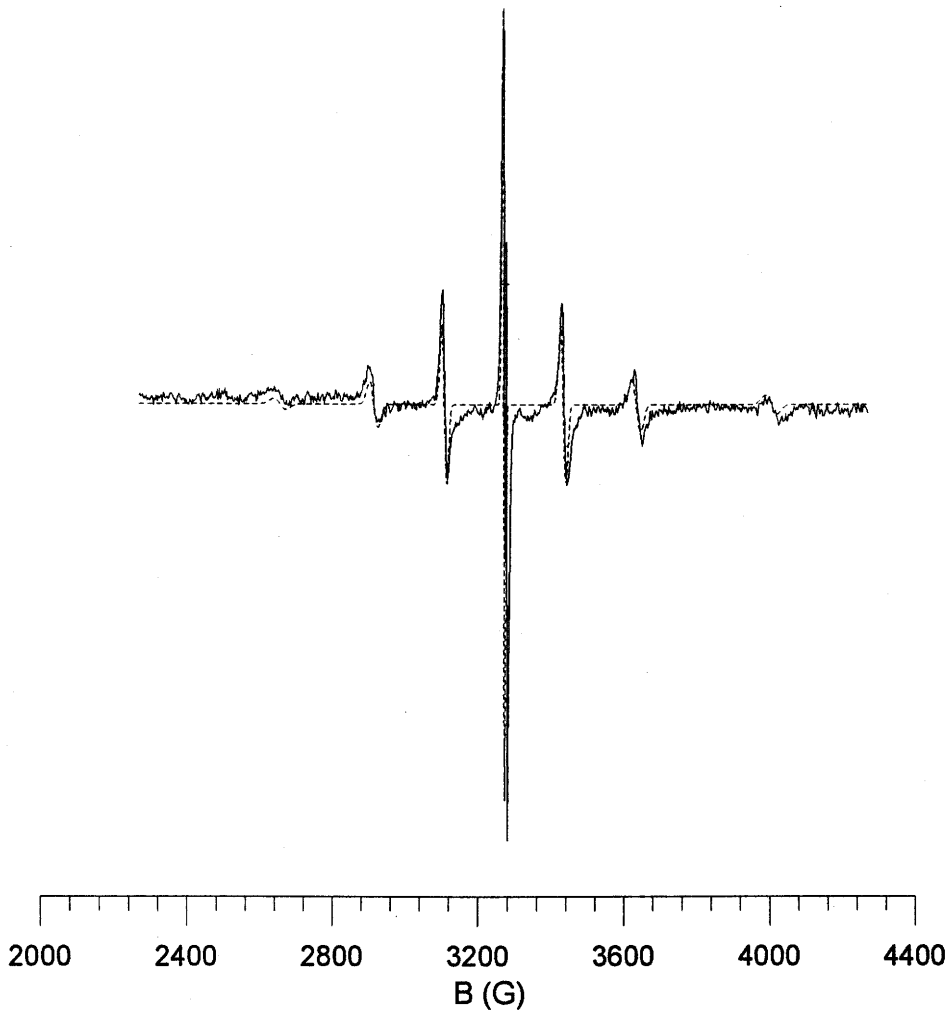

Figure 2.8b. Observed (solid line) and simulated (dashed line) single-crystal spectrum of Gd^{3+} in fluorapatite with $\mathbf{B}//\mathbf{y}$ and $\mathbf{B}_1//\mathbf{z}$, at ν = 9.1699 GHz and T = 293.5 K. The linewidths (G) used in the simulation for different transitions are 33.6 (−7/2 ↔ −5/2) 22.3 (−5/2 ↔ −3/2), 13.7 (−3/2 ↔ −1/2), 6.5 (−1/2 ↔ +1/2), 14.6 (+1/2 ↔ +3/2), 23.2 (+3/2 ↔ +5/2) and 31.2 (+5/2 ↔ +7/2), respectively. The lorentzian lineshape was used in the simulation (see text for explanation).

I - §14). The principal axis directions of the matrix **D** differ from those of the matrix **g**, also indicative of a relatively low symmetry at the Gd^{3+} centre 'a' (see below).

In particular, the principal axis $\mathbf{D}_3$ for centre 'a^1' is almost parallel to the c axis (Fig. 2.7), whereas D_1 and D_2 (not quite equal) have axes close to the two $O3^A$-$Ca2$-$O3^J$ and horizontal bisector direction of bond angle $O3^F$-$Ca2^1$-$O3^I$ (Fig. 1.2b), strongly suggesting that the Gd^{3+} ion substitutes into the Ca2 site. The validity of the principal directions of D_1 and D_2 has been confirmed by a spin-hamiltonian optimization artificially assuming $D_1 = D_2$ while varying all other parameters. The RMSD for line positions here was 3.08 G (i.e., an increase by about 10%). A further optimization, holding $D_1 = D_2$ and forcing the D_3 axis to be parallel to **z** yielded a relatively large RMSD value of 10.77 G, indicating that the deviation of axis $\mathbf{D}_3$ from **z** of the ideal experimental system is real. This deviation has also been confirmed by an optimization assuming $\mathbf{D}_3//\mathbf{z}$, with no other constraints imposed. The RMSD value increased considerably to 10.49 G.

The site assignment is further supported by the values of the reported parameters of the S^4 terms (Table 2.2). The relatively large value of B_4^{-3} (in the xyz system) indicates the existence of "triad" axes, which correspond to the directions of the relevant 4 plane normals of three atom arrangements in the approximate (six-atom) coordination polyhedron of the Ca2 site (Fig. 1.2b). In accordance with the common conventions (McGavin, 1987), the value of B_4^{-3} (or B_4^{+3}) will reach a maximum when the primary axis (z") of the reference system is parallel to any "triad". Therefore, Euler rotations were made (for the parameters of the S^4 terms) to place the z" axis parallel, in turn, to the four 3-fold pseudo-symmetry axes (See below). The resulting values of B_4^{-3} (or B_4^{+3}) all

increased dramatically, indicating the actual directions of the "triad", which match the local symmetry of the site $Ca2^1$ rather than that of the site $Ca1^1$, and thus strengthening the conclusion of the site assignment for centre 'a'.

2.4.4 Pseudo-symmetry analysis

The assignment of the Gd^{3+} centre 'a^i' (i = 1, 2, ..., 6) to the six symmetry-related sites $Ca2^i$ has also been evaluated by using the pseudo-symmetry method (e.g., Michoulier and Gaite, 1972; Gaite, 1980; 1987; Gaite et al., 1985a,b; Mombourquette et al., 1986). The method makes use of the fourth-degree terms of type S^4 of the spin-hamiltonian, because of their sensitivity to the immediate environment of paramagnetic ions. Test functions, which were developed to determine the symmetry and/or pseudo-symmetry axes (Michoulier and Gaite, 1972), will have a value of zero when the axis of the reference system is along a local symmetry axis, or will attain a minimum when the axis is along a local pseudo-symmetry axis. With the estimated local symmetry information, it is possible to assign the paramagnetic ion's surroundings by comparing the calculated symmetry or pseudo-symmetry elements and their orientations with those of the known sites in the crystal structures. As mentioned above, the Ca1 and Ca2 sites in fluorapatite are characterized by vertical three-fold and two-fold axes, respectively (Figs. 1.2a and b). Therefore, our pseudo-symmetry analysis involved searching for two- and three-fold axes by using the program ROTSTO (Tennant et al., 2000). An initial search with angle interval of 1.0° was attempted to determine the approximate orientations of the symmetry or pseudo-symmetry axes, and was followed by a more precise search with an interval of 0.05°.

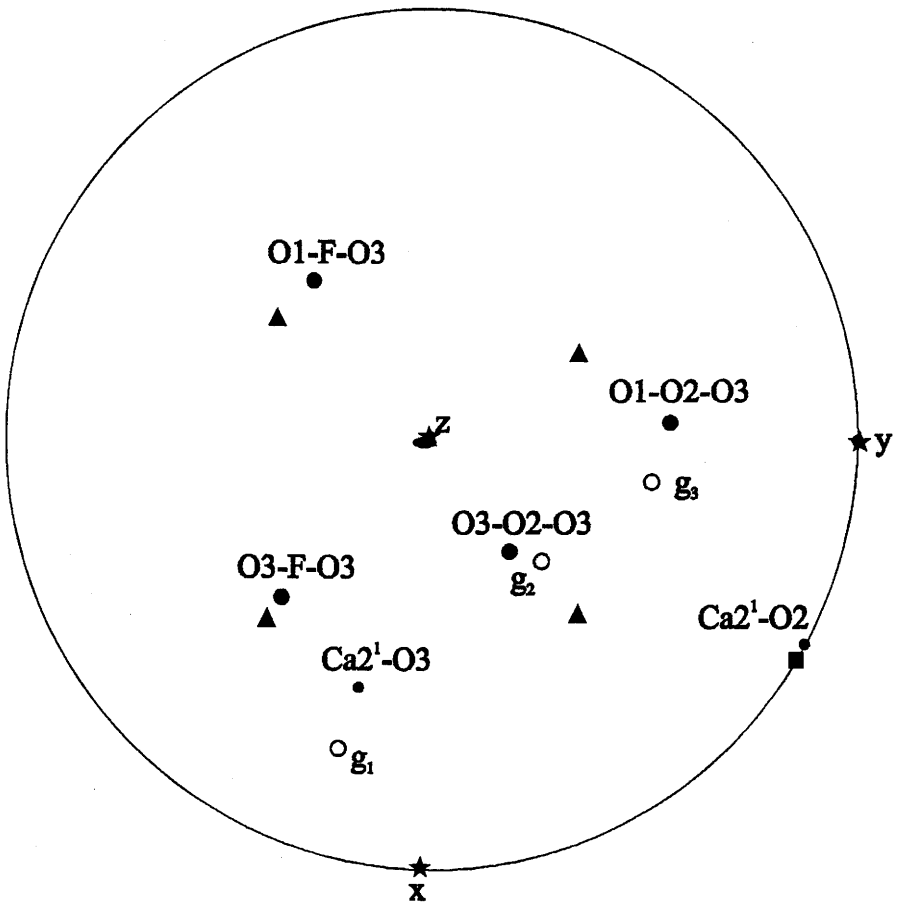

Figure 2.9. Stereographic projection of the calculated pseudo-symmetry axes (solid ellipse, 2-fold; solid triangles, 3-fold; solid square, 4-fold) and corresponding bonds (small solid circles), plane normals (solid circles) and principal directions of the g matrix (open circles) of the Gd^{3+} centre 'a'. Note that the directions of the experimental systems are expressed as small solid stars.

The results of the pseudo-symmetry analysis for the Gd^{3+} centre 'a^1' are shown in Figure 2.9. A two-fold pseudo-symmetry axis ($\theta = 2°$, $\varphi = 257°$), rather than a three-fold axis, is present and matches closely to the vertical 2-fold rotoinversion axis at $\theta = 0°$ of the $Ca2^1$ site (Hughes et al., 1989). Also, other pseudo-symmetry elements have been found but are much weaker than the two-fold pseudo-symmetry axis. For example, four weak three-fold pseudo-symmetry axes on the upper hemisphere (Fig. 2.9) correspond approximately to the plane-normals of the O1-O2-$O3^F$, $O3^F$-O2-$O3^A$, $O3^F$-F-$O3^A$ and $O3^F$-O1-F faces of the $Ca2^1$ polyhedron (Fig. 1.2b). Also, a weak four-fold pseudo-symmetry axis is present approximately along the F-Ca2-O2 direction; this apparently corresponds to the arrangement of the four O3 atoms (Fig. 1.2), further supporting the assignment of the Gd^{3+} ion to the Ca2 site for centre 'a'.

The orientations of the calculated pseudo-symmetry axes allow an estimation of distortion of the Gd-substituted CaO_6F polyhedron. For example, the absence of any true symmetry axes in the pseudo-symmetry analysis suggests that the local symmetry of the Gd^{3+} centre 'a' is rhombic, consistent with the form of the matrices **g** and **D**. It is noteworthy that rhombic (i.e., triclinic) symmetry is well-known for the Ca2 site in chlorapatite and hydroxyapatite, and is attributable respectively to the ordering of Cl and OH groups along the c axis (Elliott et al., 1973; Hughes et al., 1989; Fleet et al., 2000a,b). Similarly, Fleet et al. (2000a) noted abnormal thermal behavior of the F anions in the x-ray structure refinement of REE-substituted fluorapatites (Fleet and Pan, 1995b; 1997b) and attributed it to displacement of F ions along the c axis. Another possible cause is distortion of the REE-substituted sites (i.e., partial substitution of F^- by O^{2-}; see below).

The assignment of the centre 'a' to Gd^{3+} in site Ca2 was further strengthened by the fact that the local symmetry at the ideal Ca1 site is not consistent with the principal directions of the D matrix and pseudo-symmetry of the S^4 terms of the observed spin-hamiltonian. The local structural environment of the Ca1 site (i.e., the two Ca1-O3 bonds; Fig. 1.2a) doesn't match the principal directions of the D matrix (See Chapter 3). The local symmetry environment at the Ca1 also mismatched the pseudo-symmetry of the S^4 terms.

Admittedly, the basis for the calculated pseudo-symmetry elements of this study may be relatively weak (e.g., compared to those of Mombourquette et al., 1986), because the ideal Ca2 site in fluorapatite deviates significantly from cubic or almost cubic symmetry for which the pseudo-symmetry analysis is best suited (Michoulier and Gaite, 1972; Gaite, 1980; 1985; Mombourquette et al., 1986). However, our results appear to be rational. Some of the angles between the calculated pseudo-symmetry axes and the bonds and faces of the ideal CaO_6F coordination polyhedron as well as the principal directions of D_1 and D_2 are probably attributable to minor distortion in the local symmetry of the Gd^{3+}-occupied Ca2 site.

2.4.5 Substitution mechanism

Fleet and Pan (1995b; 1997a) discussed the following possible mechanisms for the incorporation of REEs into the Ca sites in fluorapatite:

$$REE^{3+} + Si^{4+} \Leftrightarrow Ca^{2+} + P^{5+}, \quad Ca_{10-x}\,REE_x(P_{1-x}Si_xO_4)_6F_2 \qquad (3)$$

$$REE^{3+} + Na^{+} \Leftrightarrow 2Ca^{2+}, \quad Ca_{10-2x}\,Na_xREE_x(PO_4)_6F_2 \qquad (4)$$

$$2REE^{3+} + \square \Leftrightarrow 3Ca^{2+}, \quad Ca_{10-3x}\,REE_{2x}\square_x(PO_4)_6F_2 \qquad (5)$$

$$REE^{3+} + O^{2-} \Leftrightarrow Ca^{2+} + F^{-}, \quad Ca_{10-x}REE_x(PO_4)_6(F_{2-x}O_x). \qquad (6)$$

Equations 3 and 4 can be ignored for the present fluorapatite, because neither Si nor Na is present in any significant quantities. Equation 5 involving a Ca^{2+} vacancy (i.e., □) is also unlikely for 'a'. Local charge-balance requirement dictates that the vacancy occurs at a nearby Ca2 site either in the mirror plane or along the c axis, both of which would have caused significant distortion in the local symmetry of the Gd^{3+} centre 'a'. According to the superposition model (Brodbeck and Bukrey, 1981; Kliava, 1982; Gaite et al., 1985a; Mombourquette and Weil, 1987), the principal direction associated with D_3, which indicates the direction of the largest distortion, is expected to either lie in the mirror plane or be inclined at high angles to the mirror plane, if a vacancy is present in the immediate vicinity of the Gd^{3+} ion. Table 2.1 and Figure 2.7 show that the principal direction $\mathbf{D}_3$ is almost parallel to the c axis, inconsistent with the presence of such a vacancy.

Therefore, the remaining possible mechanism for the incorporation of Gd^{3+} into the Ca2 site in fluorapatite is Equation 6, which involves a simultaneous substitution of O^{2-} for F^{-} to maintain the local charge balance. A substitution of the larger O^{2-} (r = 1.40 Å) for F^{-} (r = 1.33 Å) would cause distortion of the Gd-substituted Ca2 site and, hence, the observed rhombic local symmetry. Also, a GdO_6O centre model is consistent with the absence of any superhyperfine structures in the single-crystal EPR spectra, which might be present for a GdO_6F polyhedron owing to magnetic interaction between Gd^{3+} and $^{19}F^{-}$ (I = 1/2). The approximately uniaxial feature of matrix **D** (Table 2) also supports this substitution mechanism. A replacement of F^{-} by O^{2-} will tend to equalize

the bond distance between the substituting Gd and O2 and that between Gd and the O ion at the F site; (Fig. 1.2b), giving rise to a nearly uniaxial site symmetry (Table 2.1).

A comparison of the F bond valences (cf. Brown, 1981) between the REE-substituted fluorapatites (Hughes et al., 1991; Fleet and Pan, 1995b; 1997b) and the end-member fluorapatite (Hughes et al., 1989) further supports this mechanism for the incorporation of trivalent REEs into the Ca2 site. For example, the calculated F bond valences of La-, Nd-, Sm- and Dy-substituted fluorapatites are 0.950, 0.932, 0.911 and 0.902 v.u., respectively (Fleet and Pan, 1995b), whereas that of the end-member fluorapatite is 0.895 (Hughes et al., 1989). The higher values of the F bond valence in the REE-substituted fluorapatites are consistent with partial substitution of F^- by O^{2-}. Fleet and Pan (1995b) also noted that the REE site occupancy ratio decreases systematically from La- to Dy-substituted fluorapatite, and shows an inverse correlation with the F bond valence. It is clear now that the partial substitution of O^{2-} for F^- contributes to expansion of the Ca2 site and, hence, increased preference for the larger REEs such as La. Therefore, the present study provides further support for important roles of volatile components in controlling the uptake of REEs in apatites (Fleet and Pan, 1997a and references therein). We note that, although the processes of Gd^{3+} uptake in fluorapatite may differ because of changes in the conditions of the fluorapatite crystallization, they don't determine the resulting site symmetry of the Gd-occupied Ca sites for a given substitution mechanism, i.e., our reported result has general significance.

Finally, MacKie and Young (1973) reported that minor amounts of Nd substitute for Ca in the Ca2 position only in Nd_2O_3-doped fluorapatite, but in both Ca1 and Ca2 in NdF_3-doped crystals. The Gd_2O_3–doped fluorapatite crystals of this study were prepared

under similar conditions to the Nd_2O_3-doped fluorapatite of MacKie and Young (1973). However, this study showed that there are two major Gd^{3+} centres (the centre 'a' and 'b') in the Gd_2O_3–doped fluorapatite and that one of them corresponds to Gd^{3+} at the Ca2 site. The Gd^{3+} centre 'b' has been proved to correspond to occupancy of Gd^{3+} at the Ca1 site (Chapter 3).

2.4.6 Conclusions

A general spin-hamiltonian, including the matrices **g** and **D** and the high-spin terms of type S^4, S^6 as well as BS^3 and BS^5, has been determined for the Gd^{3+} centre 'a' in synthetic fluorapatite by analyzing well-resolved single-crystal X-band EPR spectra taken in three orthogonal-rotation planes. The validity of this spin-hamiltonian has been confirmed by agreement between the simulated and observed spectra of both single crystals and powder samples. The matrices **g** and **D** and the results of a pseudo-symmetry analysis all suggest that the Gd^{3+} centre 'a' in the synthetic fluorapatite corresponds to a substitution of Gd^{3+} into the Ca2 site and that the local symmetry of the centre 'a' is rhombic. Moreover, the information about the local structural environment of the Gd^{3+} ion suggests that the substitution mechanism for the incorporation of Gd into the Ca2 site in the synthetic fluorapatite is $Ca^{2+} + F^- \Leftrightarrow Gd^{3+} + O^{2-}$.

CHAPTER 3

Local Structure Environment and the Neighboring Ca2 Vacancy of the Gd^{3+} Centre 'b'

3.1 Introduction

In chapter 2, results were reported for the X-band (9.5 GHz) electron paramagnetic resonance (EPR) spectroscopic study of synthetic fluorapatite containing 1.2±0.2 wt % Gd_2O_3, and the well-resolved spectrum of the Gd^{3+} centre 'a' assigned to the Ca2 site (Fig. 1.2b) were described. Being different from the information obtained by high-precision x-ray structure refinement of natural and synthetic REE-bearing apatites (e.g., Hughes et al., 1991; Fleet and Pan, 1995; Comdi et al., 1999; Fleet et al., 2000a; 2000b), the X-band EPR study provided significant information for the local structural environment of the Gd^{3+}-occupied Ca2 site. Moreover, the local structural environment of the Gd^{3+} centre 'a' furnished important insights into the substitution mechanism for incorporating this ion (as a representative of the trivalent rare-earth elements, REEs) into the Ca2 site in fluorapatite. The X-band EPR spectra also suggested the possible presence of another major Gd^{3+} centre ('b'), which at this frequency is only partly observed in the single-crystal spectra. The centre 'b' is the primary subject of this chapter.

The present study was initiated for the following reasons. Firstly, a new synthesis experiment was conducted to produce fluorapatite single crystals containing only approximately 57 ppm Gd to take advantage of the EPR technique for investigating this paramagnetic ion at trace levels of concentration, which are commonly encountered in natural apatites (e.g., Pan et al., 1993; Pan and Breaks, 1997). Secondly, the single-crystal EPR study was performed at the W-band frequency (94 GHz) in order to investigate the Gd^{3+} centre 'b' that cannot be investigated at X-band EPR, although it was partly observed in the X-band experiments. Furthermore, the results reported herein allow independent testing for the spin-hamiltonian of the Gd^{3+} centre 'a' at the Ca2 site, obtained from the X-band study (Chapter 2), and determination of the spin-hamiltonian for the Gd^{3+} centre 'b'. The optimized spin-hamiltonian parameters, together with a pseudo-symmetry analysis using the S^4 parameters, permit an evaluation of the local structural environment of the Gd^{3+} centre 'b'. In particular, these results showed that Gd^{3+} of the centre 'b' corresponds to a substitution into the Ca1 site, which has a different stereochemical environment from the Ca2 site (Fig. 2.1; cf. Hughes et al., 1989). Moreover, the local structural environment of the Gd^{3+} centre 'b' provided insights into a different mechanism of substitution for incorporating REEs into fluorapatite, which (unlike that for the Gd^{3+} centre 'a' at the Ca2 site) involves a vacancy.

3.2 Experimental Methods

3.2.1 Synthesis and characterization of fluorapatite crystals

The synthesis of the Gd-doped fluorapatite single crystals of this study was similar to that described in Chapter 2, except that the starting material contained only approximately 100 ppm Gd rather than ~10,000 ppm Gd. The experimental product,

including the size, morphology and optical properties of the fluorapatite crystals, was similar to that described in Chapter 2. X-ray fluorescence microprobe analysis at the University of Saskatchewan (cf. Cheburkin et al., 1997), using other Gd-doped fluorapatite crystals that have been analyzed by electron microprobe and laser ablation inductively coupled plasma mass spectrometry (Fleet and Pan, 1997; Chapter 2) as standards, revealed that the synthetic fluorapatite crystals of this study contain 57±4 ppm Gd.

3.2.2 EPR experiments

Single-crystal EPR spectra of the Gd-doped fluorapatite were obtained at ~287 K on the MARK II W-band (94 GHz) EPR spectrometer (Nilges et al., 1999) at the Illinois EPR Research Center (IERC), University of Illinois at Urbana-Champaign. As in the previous single-crystal experiments at X-band (Chapter 2), field-swept W-band EPR experiments were performed with the Zeeman field **B** in three orthogonal rotation planes. The axes **y** and **z** of the ideal experimental coordinate system were chosen along the crystallographic axes **a** and **c**, and the direction of the axis $\mathbf{x} = \mathbf{y} \otimes \mathbf{z}$ is defined. However, the axes of the actual experimental system were not exactly the axes of the ideal system, and are therefore referred to as **x'**, **y'**, and **z'** (i.e., the rotation were planes x'y', y'z' and x'z'; see Table 3.1), because precise alignment of single crystals with respect to **B** (e.g., Chen et al., 1999) is difficult on the W-band instrument owing in part to its small resonant cavity (~2.4 mm in diameter). In this study, we mounted a prismatic crystal of the Gd-doped fluorapatite in a quartz tube of 0.7 mm internal diameter, which was then aligned inside the resonant cavity under binoculars for measurements in plane

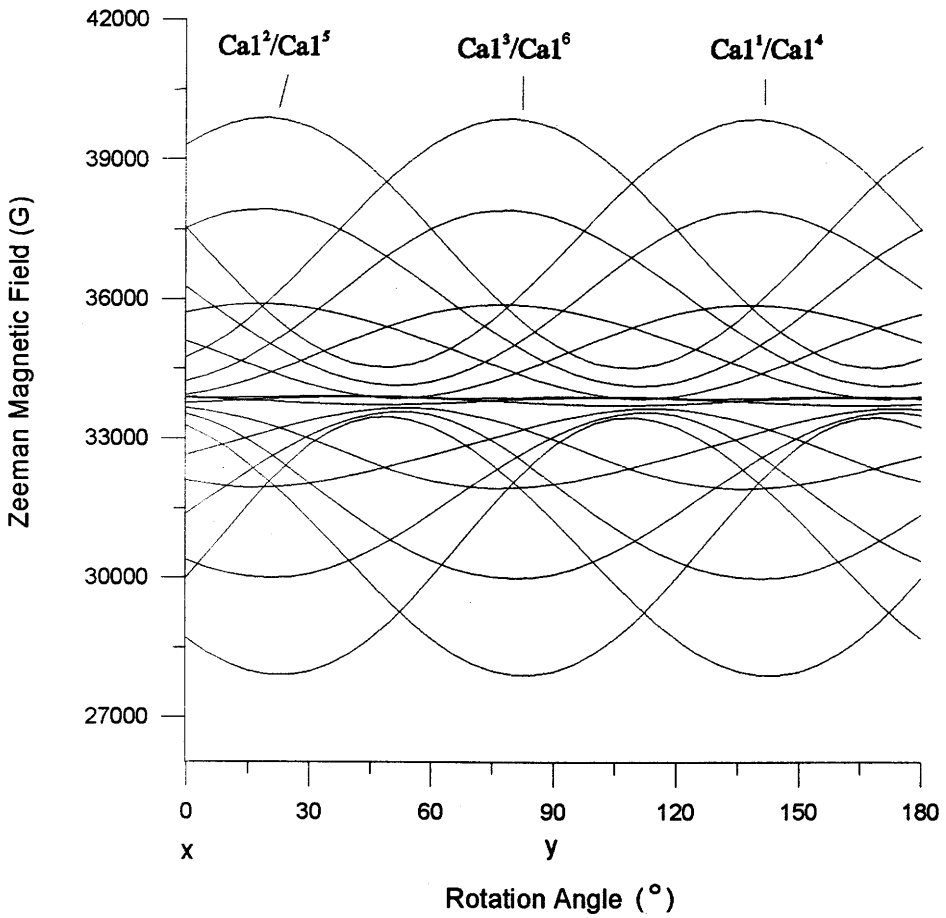

Figure 3.1a. Calculated angular dependence ("line-position roadmap") of the EPR spectrum for the Gd^{3+} centre 'b' in fluorapatite with Zeeman field **B** rotated in the plane xy of the ideal experimental system. Effectively, each curve is two-fold degenerate.

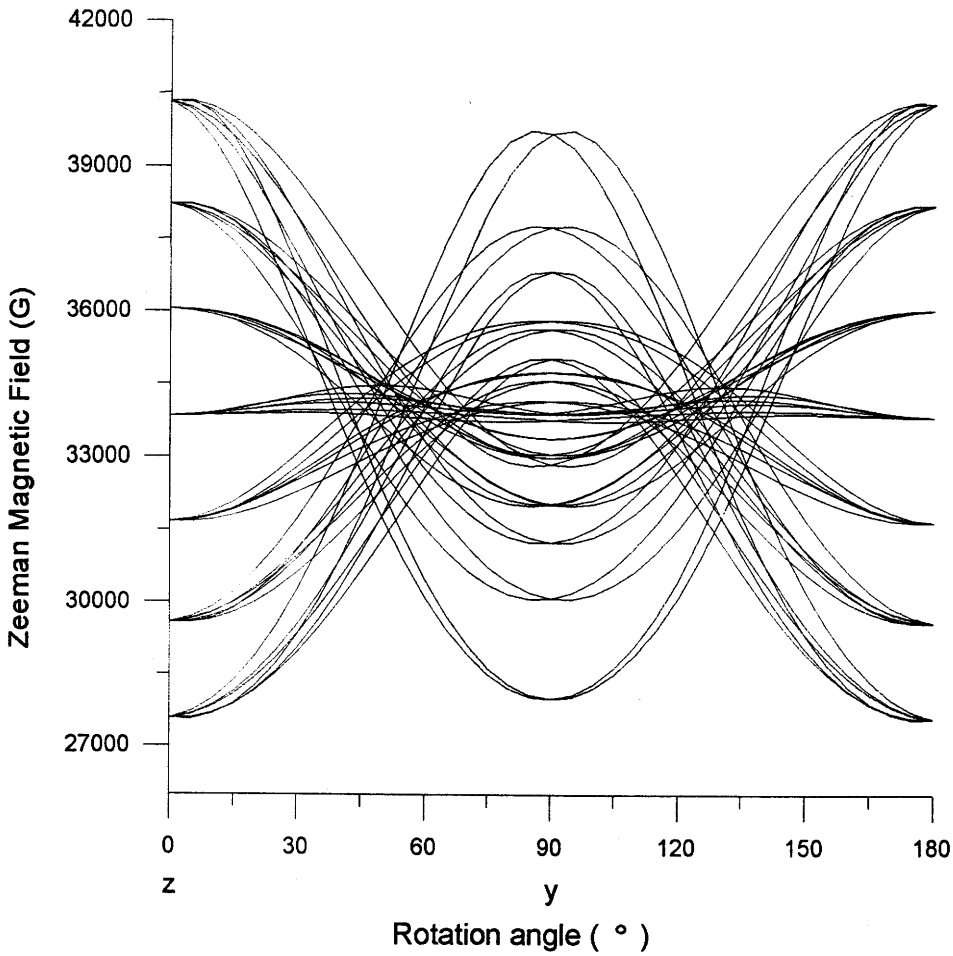

Figure 3.1b. Calculated angular dependence ("line-position roadmap") of the EPR spectra for the Gd^{3+} centre 'b' in fluorapatite with the Zeeman field **B** rotated in the plane yz of the ideal experimental system. The six Ca1 sites are magnetically equivalent at **B**//**z**.

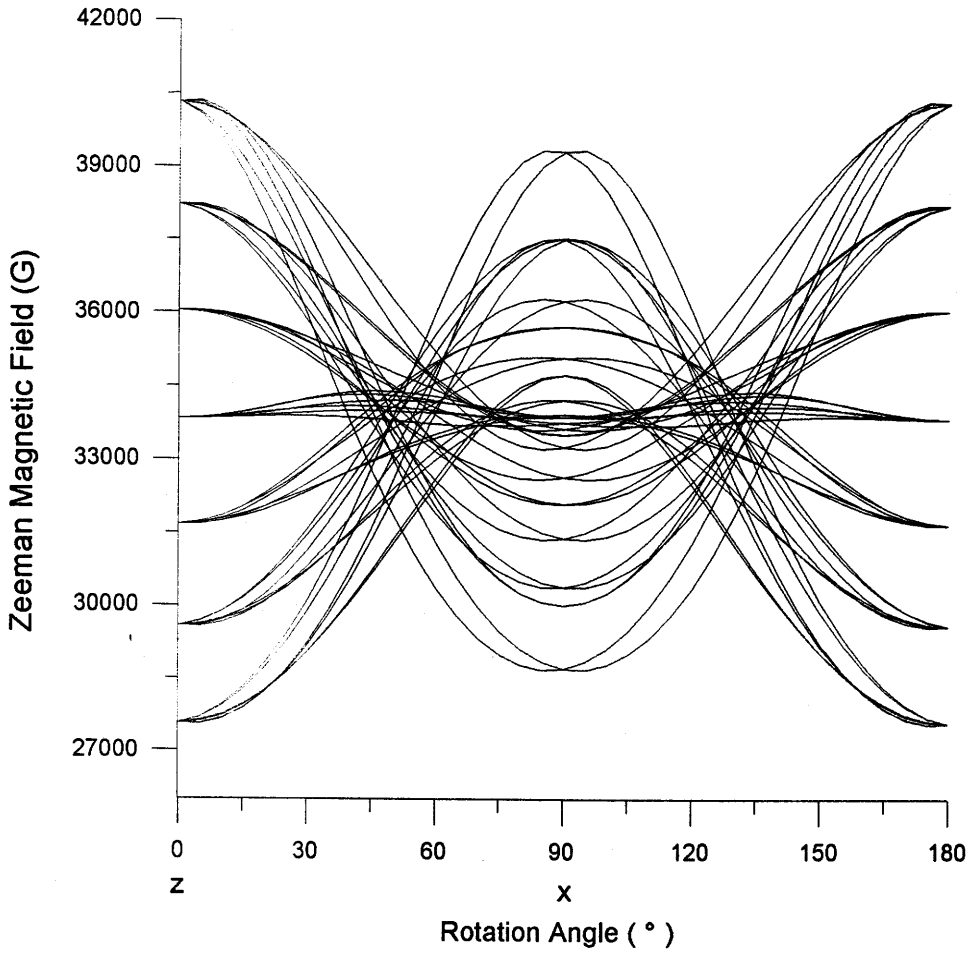

Figure 3.1c. Calculated angular dependence ("line-position roadmap") of the EPR spectrum for the Gd^{3+} centre 'b' in fluorapatite with the Zeeman field **B** rotated in the plane xz of the ideal experimental system. The six Ca1 sites are magneticlly equivalent at **B//z**.

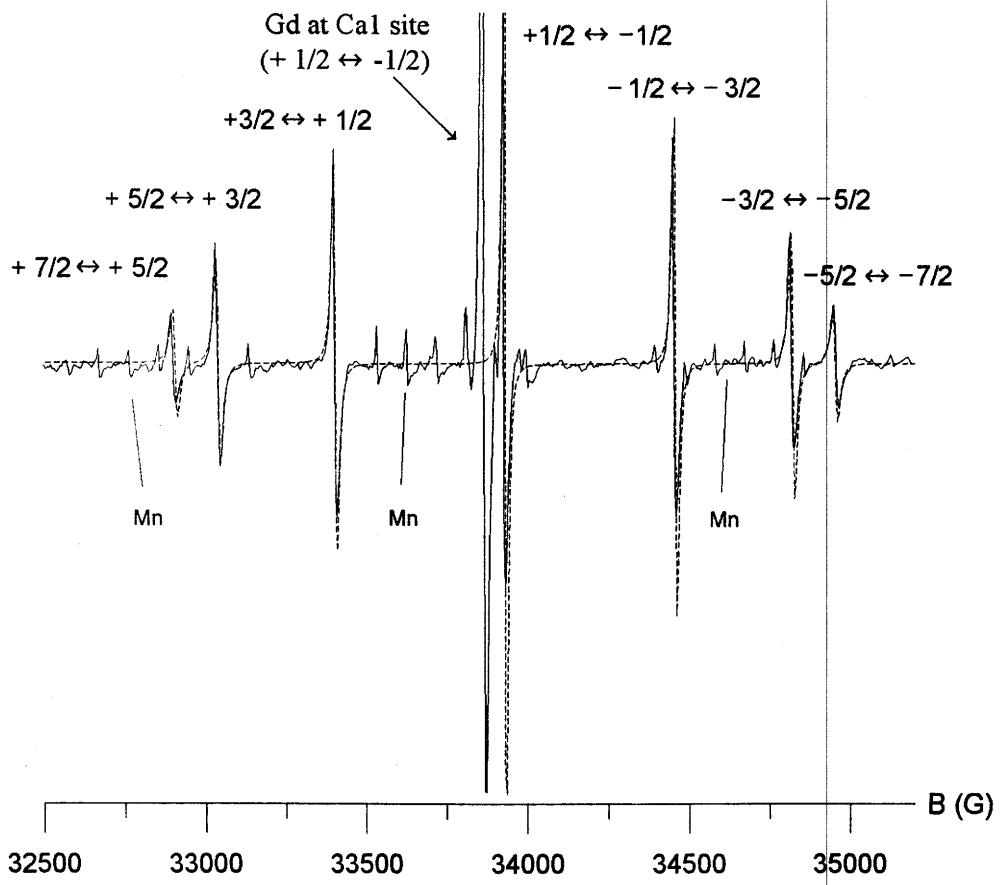

Figure 3.2. Observed (solid line) and simulated (dashed line) single-crystal spectrum of Gd^{3+} at the Ca2[1] site in fluorapatite with **B** // **z'** and $\mathbf{B}_1$// **x'**, at ν = 94.5017 GHz and T =~295.0 K. The linewidths (G) used in the simulation for different transitions are 15.0 (−7/2 ↔ −5/2), 13.5 (−5/2 ↔ −3/2), 11.8 (−3/2 ↔ −1/2), 9.6 (−1/2 ↔ +1/2), 11.8 (+1/2 ↔ +3/2), 13.5 (+3/2 ↔ +5/2) and 15.0 (+5/2 ↔ +7/2), respectively. The lorentzian lineshape was used in the simulation (see text for explanation).

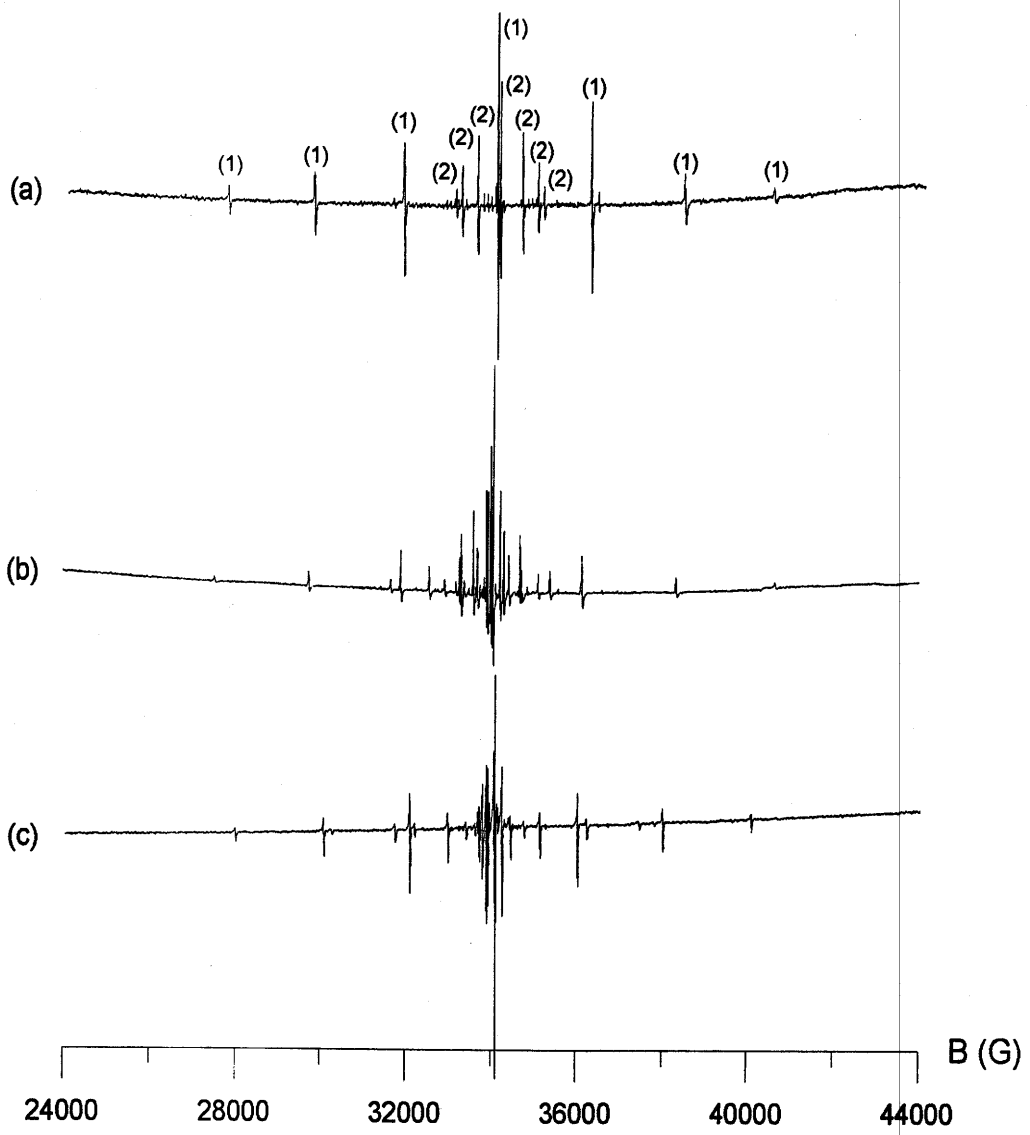

Figure 3.3. Single-crystal W-band EPR spectra of the Gd-doped fluorapatite at ~287 K: (a) with **B** //z' and $\mathbf{B}_1$//x', at ν = 94.5017 GHz; note that the lines related to the Gd^{3+} centre 'b' are labeled as "1" and those for 'a' at the Ca2 sites as "2"; (b) with **B** //x' and $\mathbf{B}_1$//y', at ν = 94.4682 GHz; (c) with **B**//y' and $\mathbf{B}_1$//x', at ν = 94.4579 GHz. Note that magnetic site splitting is visible when **B**//x' and **B**//y'.

x'y' (i.e., $\mathbf{B} \perp \mathbf{z}'$). For measurements in the x'z' and y'z' planes, the crystal of fluorapatite was mounted using Duco cement on a quartz rod (0.78 mm diameter), which was glued directly to the resonant cavity using such cement. Alignment was made approximately by use of a well-developed crystal face and a crystal edge of the hexagonal prism as references for planes x'z' and y'z', respectively. Not surprisingly, relatively large errors in crystal alignment existed (e.g., ~15° in the x'y' plane; Table 3.1). These errors were corrected for, initially, according to the line-position roadmaps in the three orthogonal rotations and were corrected further during the spin-hamiltonian optimization by using the software package EPR-NMR (Mombourquette et al., 1996). Figures 3.1 show the roadmaps of the three rotations in the ideal experimental system. The validity of the calibrations of the crystal alignment has been confirmed by excellent agreement between the observed and predicted single-crystal spectra from all transitions of the Gd^{3+} ions (S = 7/2) at the six symmetry-related Ca2 sites when **B//z'**, as well as by agreement between the observed and calculated single-crystal spectra for selected transitions (e.g., between spin-projection quantum number m_S values −1/2 and +1/2) of the Gd^{3+} ions at the six Ca2 sites, when **B//x'** and when **B//y'**.

The field-swept EPR experiments with the Zeeman field **B** rotated in the three orthogonal planes were carried out at average frequencies 94.467(8), 94.480(3) and 94.460(8) GHz for planes x'y', x'z' and y'z', respectively (Figs. 2.1a, 3.1b, and 3.1c). The spectral resolution was 4.9 G (i.e., 4,096 field data points over 20,000 G in each spectrum), and the angle intervals were 10° and 20° in plane x'y', and 10° in the x'z' and y'z' planes. The numbers of line-position data points were 163, 234 and 254 in planes x'y', x'z' and y'z', respectively. The B-field calibration of the W-band spectrometer was

done by use of a Metrolab NMR Gaussmeter PT2025 (Nilges et al. 1999). The standard deviations of the line-position errors between the values observed and values obtained from the spin-hamiltonian parameters for centre 'b' were found to be 13 (15 lines), 11 (16 lines), and 10 G (7 lines) at **B//x'**, **B//y'**, and **B//z'**, respectively. The further field calibration was made by comparison, for centre 'a', of the observed line positions in the W-band experiments and those predicted by the spin-hamiltonian parameters derived from the well-calibrated X-band experiments (Chapter 2). The standard deviations of the line-position errors for 'b' were thereby reduced to 7, 5, and 3 G at **B//x'**, **B//y'**, and **B//z'**, respectively.

Powder samples of the Gd-doped fluorapatite were obtained by grinding single crystals in an agate mortar, and were investigated at Illinois on the MARK II W-band EPR spectrometer at ~287 K and on a Q-band Varian E-15 EPR spectrometer at ~295 K. The powder W-band spectrum shows that, except for the very strong central peak (transition $-1/2 \leftrightarrow +1/2$), the signals from the other transitions are not well defined. The powder Q-band spectrum shows better resolution for the other transitions but, as was shown by simulation, is dominated by contributions from the Gd^{3+} centre 'a' at the Ca2 sites.

3.3 Results and Discussions

3.3.1 EPR spectra

The single-crystal W-band EPR spectra of the Gd-doped fluorapatite display two distinct centres of Gd^{3+} ($S = 7/2$). The first one (centre 'a') corresponds to Gd^{3+} located at

TABLE 3.1 Ideal and calibrated directions of the rotation-plane normals and the crystal reference systems in the W-band EPR experiments.

Plane	x (or x')		y (or y')		z (or z')	
	θ	ϕ	θ	ϕ	θ	ϕ
xy	90.00[a]	0.00[a]			0.00[c]	0.00[c]
	92.72[b]	15.14[b]			5.00[d]	52.22[d]
yz	90.00[c]	180.00[c]			0.00[a]	0.00[a]
	89.48[d]	179.98[d]			0.54[b]	14.40[b]
xz			90.00[c]	90.00[c]	0.00[a]	0.00[a]
			89.78[d]	90.22[d]	0.22[b]	95.59[b]

[a] Ideal directions of the experimental system, i.e., the xyz-axis system
[b] Actual directions of the experimental system, i.e., the x'y'z'-axis system, estimated by the program EPR-NMR
[c] Ideal directions of the rotation planes (plane normals), i.e., the xyz-axis system
[d] Actual directions of the rotation planes (plane normals), i.e., x'y'z'-axis system, estimated by the program EPR-NMR

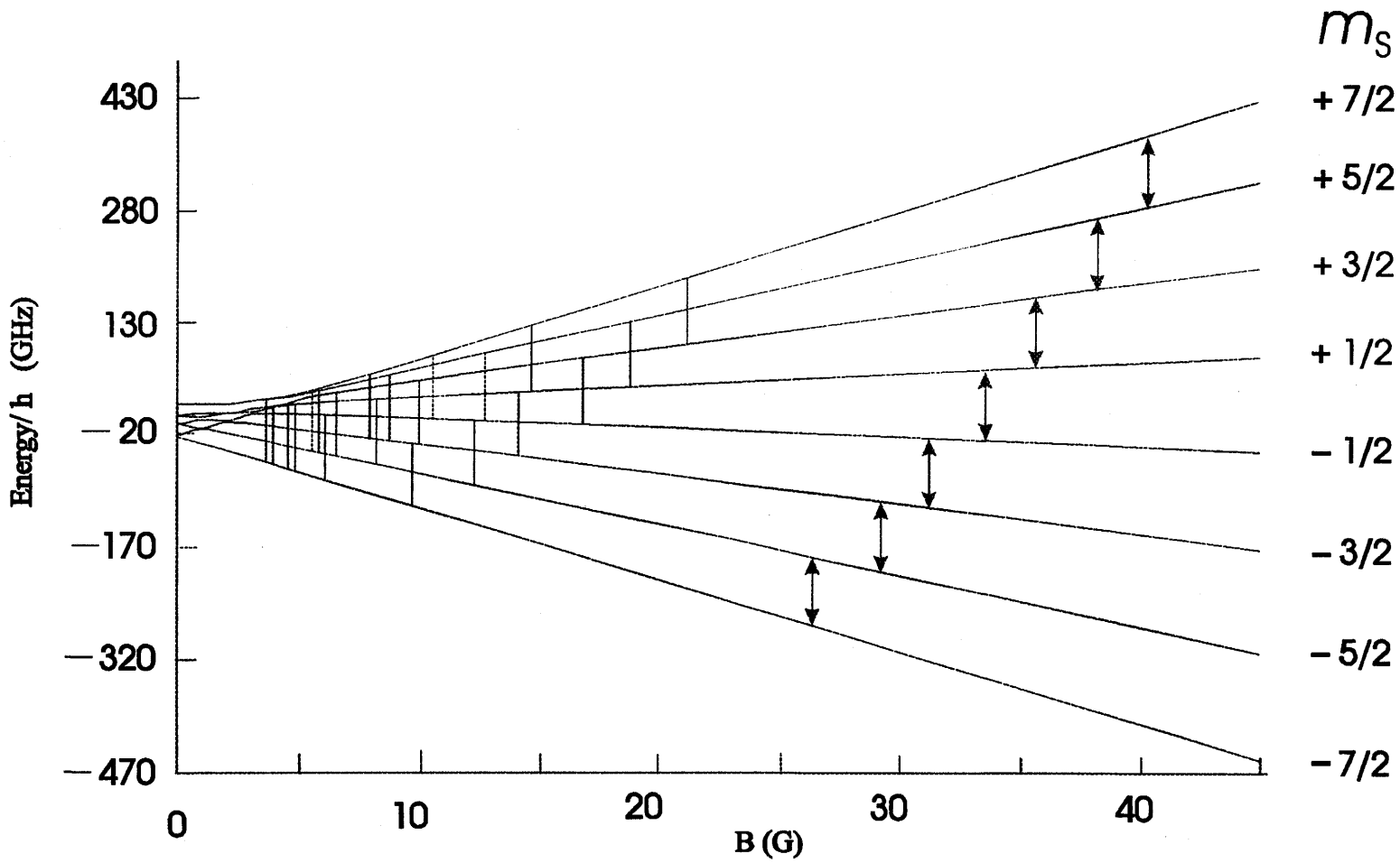

Figure 3.4a. Simulated energy levels for the Gd^{3+} centre 'b' in fluorapatite at T = 278 K when and **B//z**. The seven "allowed" transitions at $\nu = 94.5017$ GHz are labeled as single lines with arrows, and the "forbidden" transitions are labeled as single lines without arrows but have not been detected in EPR experiments.

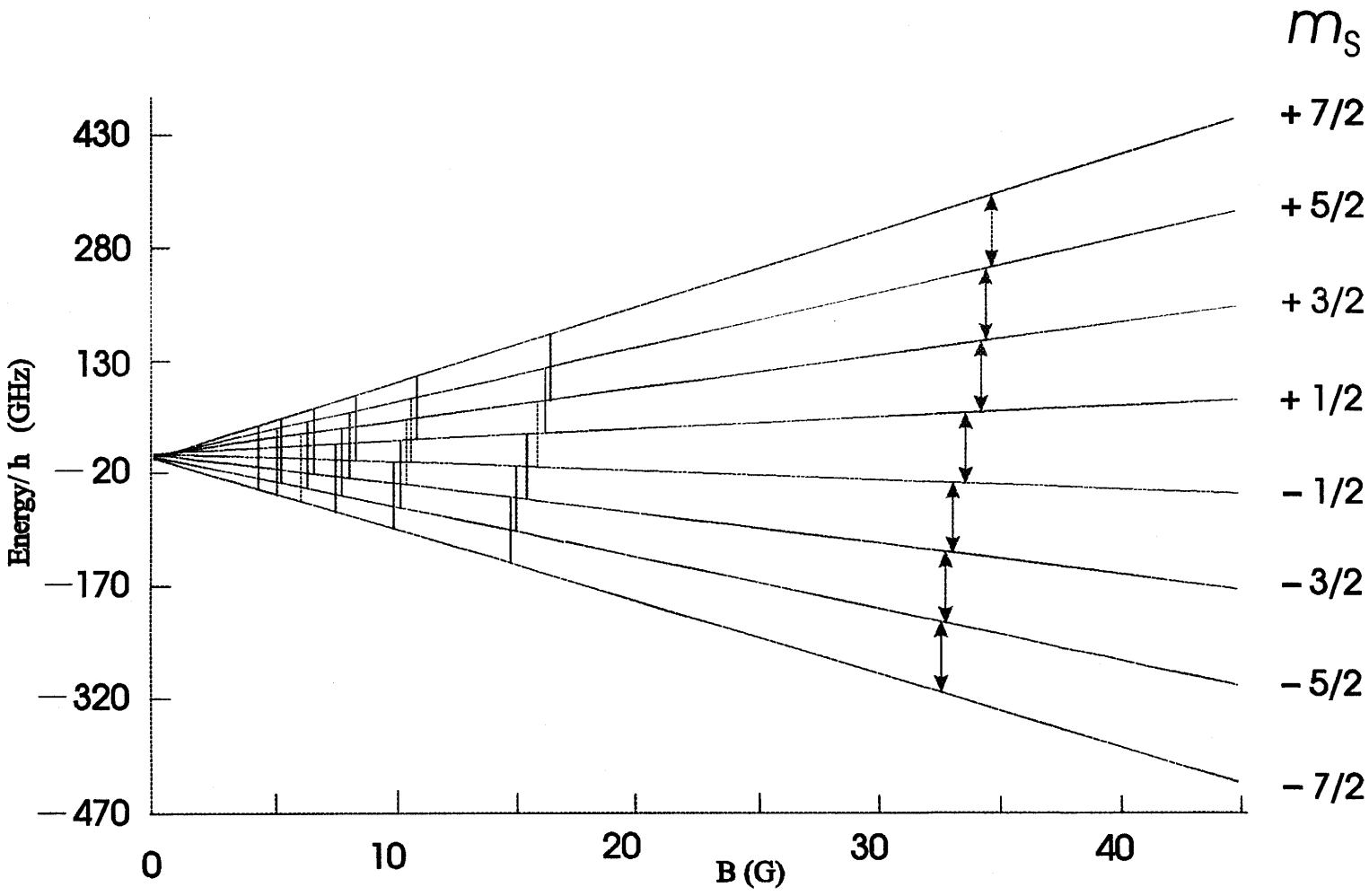

Figure 3.4b. Simulated energy levels for the Gd^{3+} centre 'a' in fluorapatite at T = 278 K when **B//z**. The seven "allowed" transitions at $\nu = 94.5017$ GHz are labeled as single lines with arrows, and the "forbidden" transitions are labeled as single lines without arrows but have not been detected in EPR experiments.

the Ca2 sites, which has been investigated in detail in the previous X-band EPR study (Chapter 2). It is noteworthy that the line positions of the Gd^{3+} centre 'a' in the W-band single-crystal spectrum match well with those predicted by the reported spin-hamiltonian (i.e., Equation 1 in Chapter 2) estimated by the X-band experiments (Fig. 3.2), further supporting the validity of this spin-hamiltonian. The EPR signals from the centre 'b', which could be observed only partly in the single-crystal X-band spectra and was proved, by the X-band single-crystal spectrum simulation, caused by a new centre, are now clearly detected in the W-band spectra and are characterized by a larger fine-structure splitting than that of the Gd^{3+} ions at the Ca2 sites (centre 'a'). As discussed in the following section, the Gd^{3+} ions of the centre 'b' can be assigned to being at Ca1 sites.

Figure 3.3a shows that the spectral fine structures of the two Gd^{3+} centres in fluorapatite are clearly observed at W-band spectrum for **B//z'**. The seven anisotropic lines assigned to the Gd^{3+} centre 'b' are from its primary "allowed" transitions (Fig. 3.4). The lines from the "forbidden" transitions (Fig. 3.4) were shown by simulation using the final spin-hamiltonian to be very weak (≤ 0.01 % of the "allowed" transitions for both centres), and thus were not measured.

At field orientations other than **B//z'**, magnetic-site splittings from Gd^{3+} in the six symmetry-related sites $Ca1^i$ ($i = 1, 2, \ldots, 6$; Fig. 2.1) shown as the multiple line structure for the same transition are well resolved for the new centre (Fig. 3.3). For example, the simulation of the line-position roadmap indicates the presence of the three seven-line fine structures (two-fold degenerate, Fig. 3.1a) in the ideal rotation plane xy indicates a C_3 effective proper rotation group, which is a subgroup of the C_6 crystal symmetry group

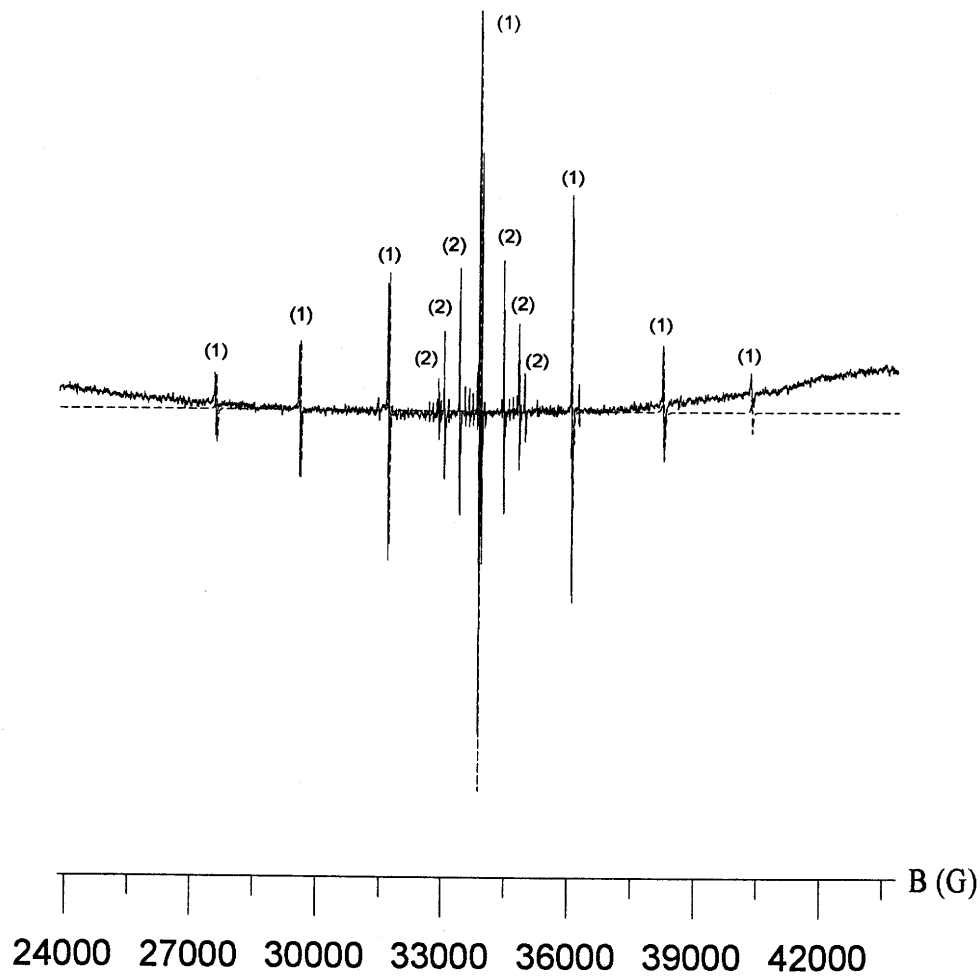

Figure 3.5. Observed (solid line) and simulated (dashed line) single-crystal spectrum of Gd^{3+} in fluorapatite with **B//z'** and $\mathbf{B}_1$//x', at ν = 94.5017 GHz and T = 287.0 K. The linewidths (G) used in the simulation for different transitions are 21.5 (−7/2 ↔ −5/2), 18.0 (−5/2 ↔ −3/2), 14.1 (−3/2 ↔ −1/2), 12.5 (−1/2 ↔ +1/2), 14.6 (+1/2 ↔ +3/2), 18.0 (+3/2 ↔ +5/2) and 21.5 (+5/2 ↔ +7/2), rerspectively. The lorentzian lineshape was used (see text for explanation). Note that the simulation also included the spectrum of the Gd^{3+} centre 'a' (labeled as "2"), which was shown separately with a larger scale in Fig. 3.2

(Fig. 2.1). Furthermore the simulation of the line-position roadmap also indicates that strongly angular dependence and crossovers of the EPR transitions exist in the spectra in all three rotations (Fig. 3.1).

The W-band EPR spectra do not show any evidence of hyperfine structure for either of the two Gd^{3+} centres. We also noted the absence of any hyperfine structure for the Gd^{3+} ions at the Ca2 sites in the X-band experiments (Chapter 2) and attributed this primarily to the low natural abundances of ^{155}Gd and ^{157}Gd relative to their even isotopic counterparts. Simulation for each of the individual lines of the Gd^{3+} centre 'b' at **B//z'**, where no magnetic-site splittings are visible (see below), yielded no evidence for the presence of any satellite hyperfine peaks. Measurements of ^{157}Gd-enriched fluorapatite have been made. The matrices **A**, **P** and $\mathbf{g}_n$ as well as the terms of type S^3I and and SI^3 were estimated for the Gd^{3+} ion located the Ca2 site for centre 'a', and will be discussed in the Chapter 4.

3.3.2 EPR lineshapes and linewidths

The basic EPR lineshape for the Gd^{3+} centre 'b' is of the lorentzian type, as confirmed by simulation for the seven EPR spectral lines with **B//z'** and excitation field $\mathbf{B}_1$**//x'** (Fig. 3.5). At **B//z'**, only near-degeneracy is expected. This has been confirmed by single-crystal spectrum simulation (Fig. 3.5), using the final spin-hamiltonian, which revealed that here the six components of the central line (i.e., transition between m_S $-1/2 \leftrightarrow +1/2$) arising from the symmetry-related Ca1 sites become 3 doubly degenerate line sets (with spacings 0.51 and 0.54 G, and internal splittings of 0.18, 0.14 and 0.05 G, respectively), resulting in a total broadening effect of 1.3 G. The measured

width of the single unresolved line is 12.5 G. Thus the inherent EPR linewidth, observable at **B//z**, will be approximately 10.2 G. Possible cause(s) for the inherent linewidths of the Gd^{3+} centres have been discussed in Chapter 2.

The inherent linewidth for the spectra of centre 'a' (Gd^{3+} ion occupying a Ca2 site) was found to be 8.7 G at W-band, which is slightly greater than that (6.4 G) found at X-band (Chapter 2). This difference in linewidth for the same centre between W- and X-band experiments may be due to the different spectral resolutions used (i.e., 0.1 and 4.9 G, respectively).

It is worth noting that, in the W-band experiments, the inherent linewidth for the centre 'b' is 1.5 G broader than that for centre 'a', suggesting additional effect(s) affecting 'b'. For example, there may exist slight differences in the principal values and directions of the matrices **D** for the two Gd^{3+} ions at Ca1 sites thought to be situated between a nearby vacancy at a Ca2 site (see below).

At all field orientations other than **B//z**, the degeneracy is lifted, i.e., splitting into 2, 3 or 6 lines occurs but is not necessarily detectable. Hence an effective linewidth greater than the inherent one is generally observed. This too has been confirmed by simulations of the central lines ($-1/2 \leftrightarrow +1/2$), including all 6 Ca1 sites. In plane xy, the roadmap (Fig. 3.1a) as well as the simulations of the single-crystal spectra indicates two-fold degeneracy for each of the three separated line sets.

At **B//x** and **B//y**, the single-crystal spectrum simulation revealed again that the six components of the central line ($-1/2 \leftrightarrow +1/2$) become 3 doubly degenerate line sets (with spacing of 3.05 and 121.53 G at **B//x**, and 24.33 and 129.25 G at **B//y**). These calculated spacings indicate that one of the doubly degenerate lines will be completely

separated from the lines arising from other symmetry-related Ca1 sites and makes it possible to estimate the inherent linewidths in this plane, similar to the estimation done at **B//z'**. As stated, our measurements were not taken exactly in the plane xy because of the deviation in the crystal alignment. Additional site splittings occur with **B** away from this plane, resulting in observed linewidths (i.e., effective widths) greater than the inherent ones.

With **B** in planes x'z' and y'z', the linewidths are anisotropic owing to the (line-position) contributions arising from the different magnetic sites. The measured linewidth of the central line (transition $-1/2 \leftrightarrow +1/2$) in plane x'z' has a minimum value of 12.5 G at **B//z'** but has a higher value of 13.3 G at **B//x'**, whereas the linewidths in plane y'z' are 12.9 and 14.2 G at **B//z'** and **B//y'**, respectively. The simulation for the single-crystal spectra in plane x'z' revealed that the observed effective linewidths are proportional to the magnetic-site splitting. This result can explain why the measured linewidth at **B//z'** is larger in plane y'z' than those observed in plane x'z' at **B//z'**. This difference in linewidth is most likely attributable to the considerably larger errors in the crystal alignment for the y'z' plane, which results in magnetic site splitting (Table 3.1). This conclusion matches those simulations made for the line-position roadmaps in planes xz and yz (Fig. 3.1b and 3.1c), which predict that the magnetic site splitting depends on the angular deviation of the actual experimental system x'y'z' from that of the crystal system.

The experimental results at W-band indicate that the linewidths of the Gd^{3+} centre 'b' are a function of the transition (between $m_S \leftrightarrow m_S+1$, $-7/2 \leq m_S \leq 5/2$), increasing with increasing $|m_S|$. This effect also is seen in the W-band spectra for Gd^{3+} at the Ca2 sites, but is smaller that was observed at X-band (Chapter 2) because of the

increased microwave frequency. This observation agrees semi-quantitatively with that predicted by the splitting expression derived from the energy equation of second-order perturbation theory (Weil et al., 1994; p. 189). The continuous distribution in the principal directions of the matrix **D** and in the high-order electronic quadrupole energy (and higher) terms causes banding effects for the energy levels, resulting in a line-position band for each transition. This banding causes broadening of the linewidth. Since the effect is inversely proportional to the experimental frequency, a smaller linewidth is observed at W-band EPR than at X-band.

3.3.3 Spin-hamiltonian optimization and spectral simulation

Program EPR-NMR (Mombouquette et al., 1996) was used in the optimization of the spin-hamiltonian parameters for the W-band spectra. On the basis of the magnetic-site splitting observed in plane x'y' (Fig. 3.1a), the spin-hamiltonian optimization was attempted first by assuming an effective C_3 symmetry. Subsequently, C_6 symmetry was adopted in fitting to match the actual magnetic crystal symmetry, and the same results were obtained as those generated with C_3. During the course of the optimization, iterative fittings were made separately for each of the spin-hamiltonian terms [i.e., the BS term (**g** matrix), the S^2 term (**D** matrix) and the terms BS^3, S^4, BS^5 and S^6], and were followed by a simultaneous fitting for all terms, and by corrections for the directions of the magnetic field. In each step of these fittings, iteration was continued until no changes at the last decimal point (the machine accuracy) of the root-mean-sum-of-squares of weighted differences (RMSD) between the calculated and observed line positions. The same weighting criteria as those used in optimization of the spectra for 'a' (Chapter 2, Chen et al., 2001b) were adopted when optimizing the W-band spectra for 'b'. The final

RMSD for line positions was 7.0 G, which is approximately half of the observed linewidth (12.5 G) of the central line, i.e., the transition $-1/2 \leftrightarrow +1/2$ at **B//z'**.

The six symmetry-related matrices **g** and **D** for the effective magnetic point group C_6 can be assigned to the six Ca1 sites (Fig. 1.1). Matrices **g** and **D** for one of the Ca1 sites (i.e., the one labeled $Ca1^1$ in Fig. 1.1) are given in Tables 3.2 and 3.3, and the corresponding parameters for the terms of type S^4, S^6 and BS^3 are summarized in Table 3.4. The contribution from each spin-hamiltonian term (i.e., Equation 1 in Chapter 2) to the overall RMSD has been evaluated by setting that term to zero while keeping all other terms at the optimized values. The resulting calculated contributions from terms BS^3, S^4, BS^5 and S^6 to the RMSD are 18.47, 21.16, 1.88 and 0.84 G, respectively. The magnitude of the parameters in the term BS^3 is 10^{-5} (Table 3.4), whereas the magnitude of the parameters in the term BS^5 is 10^{-6} (not included in Table 3.4). An even smaller magnitude is expected for the parameters in the term BS^7, which therefore were not included in the optimization.

The three principal values of **g** (Table 3.2), although very close to being equal to each other and slightly smaller than that of a free electron, are distinct and thus indicate rhombic local symmetry. These g values are similar to those of other Gd^{3+} centres (Al'tshuler and Kozyrev, 1974, App. I - §14).

Now considering parameter matrix **D**, one notes that the orientation of the principal D_3 axis is almost parallel to the crystallographic **c** axis (Table 3), while those of D_1 and D_2 are close to the directions of two Ca1-O3 bonds (see below), strongly suggesting that the Gd^{3+} ion occupies the Ca1 sites (Fig. 1.1). Figure 3.6 shows the directions $\mathbf{D}_1$ and $\mathbf{D}_2$ for the six symmetry-related Gd^{3+}-occupied Ca1 sites. A separate

optimization, in which the direction $\mathbf{D}_3$ was forced to be parallel to the axis **z** (i.e., **B//c**) and without imposing any other constraints, resulted in a considerably larger RMSD value of 76.7 G, confirming that the deviation of $\mathbf{D}_3$ from **c** is significant. The fact that **g** and **D** have different sets of principal directions (Tables 3.2 and 3.3) also suggests that the Gd^{3+} ion in centre 'b' has a low local symmetry.

Figure 3.4a illustrates that the calculated energy levels at **B//z** are in close agreement with the results of the W-band EPR experiments. The "allowed" transitions ($|\Delta m_S| = 1$) tend to occupy higher magnetic field regions than do the "forbidden" transitions ($|\Delta m_S| > 1$). The roadmap predicted by the estimated spin-hamiltonian for the xy plane in the ideal experimental coordinate system clearly shows that there is a three-fold symmetry axis along the crystallographic axis **c** (Fig. 3.1a), and the roadmaps for the xz and yz planes are indicative of six-fold degeneracy at **B//z** (Figs. 3.1b and 3.1c). The observed and simulated single-crystal spectra at **B//z'** (Fig. 3.5) and **B//x'** and **B//y'** are in excellent agreement, supporting the validity of the calculated spin-hamiltonian (Tables 3.2, 3.3 and 3.4).

Moreover, the validity of the determined spin-hamiltonian parameters for 'b' and 'a' (Chapter 2, Chen et al., 2001a) has also been demonstrated by the excellent agreement between the observed and simulated Q-band powder spectra (Fig. 3.7). In this simulation, the concentration ratio between the centres 'a' and 'b' was 3.42, evaluated by single-crystal spectrum simulation (Fig. 3.7), providing further supporting for the feasibility of multi-frequency EPR as a useful tool to determine the REE site occupancy in fluorapatite.

TABLE 3.2 The principal values and directions of the matrices **g** for the Gd^{3+} centre 'b' at ~ 287 K and the Gd^{3+} centre 'a' at the $Ca2^{1}$ site at 294.8 K.

Y	Matrices			k	Principal values Y_k	Principal directions θ_k (°)	φ_k (°)
	1.99075(7)	0.00133(5)	−0.00010(6)	1	1.99160(6)	36(3)	37(3)
g^{Ca1} [1]		1.98686(7)	0.00123(6)	2	1.99098(6)	122(3)	6(7)
			1.99107(3)	3	1.98610(6)	104(1)	106(1)
	1.9914(2)	−0.0003(2)	0.0003(2)	1	1.9916(2)	73(8)	345(7)
g^{Ca2} [1] [a]		1.9900(2)	−0.0003(2)	2	1.9903(2)	14(2)×10	5(2) ×10
			1.9902(2)	3	1.9898(2)	6(2)×10	9(1) ×10

[a] Chapter 2;
The estimated errors are given in parentheses.

TABLE 3.3 The principal values and directions of the matrices **D** for the Gd^{3+} centre 'b' at ~ 287 K, and the Gd^{3+} centre 'a' at Ca2[1] [a] at 294.8 K.

Centre	Matrix $\mathbf{D}/g_e\beta_e$ (G)			k	Principal values $D_k/g_e\beta_e$ (G)	Principal directions θ_k (°) [c]	φ_k (°) [c]
	409.0(2)	−300.4(2)	−59.0(2)	1	664.3(2)	87.40(1)	140.01(2)
Ca1[1]		303.9(2)	30.5(2)	2	51.7(2)	89.06(2)	230.06(2)
			−713.0(1)	3	−716.0(2)	2.73(1)	340.0(3)
	$D/g_e\beta_e$ = 1069.2(1) G, $E/g_e\beta_e$ = 52.4(3) G [b]						
	67.07(5)	0.06(6)	6.23(7)	1	67.37(6)	88.1(1)	36(8)
Ca2[1] [a]		67.13(6)	2.83(8)	2	67.06(6)	90.4(3)	125(8)
			−134.19(4)	3	−134.43(4)	1.94(2)	204.4(7)
	$D/g_e\beta_e$ = 201.64(4) G, $E/g_e\beta_e$ = 0.16(6) G [b]						

[a] Chapter 2

[b] $D = 3D_3/2$, $E = (D_1 - D_2)/2$ (Weil et al., 1994)

[c] Relative to the ideal experimental coordinate system

TABLE 3.4 Parameters of the high-spin terms of type S^4, S^6 and BS^3 at ~ 287 K for the Gd^{3+} centre 'b'.

S^4 ($l_1 = 0$)		S^6 ($l_1 = 0$)		BS^3 ($l_1 = 1$)		
m_2	$B_{l_2=4}^{m_2}$ (G)	m_2	$B_{l_2=6}^{m_2}$ $\times 10^{-3}$ (G)	l	m	$g_{l,m,3}$ $\times 10^{-5}$
0	0.0593(8)	0	−0.36(4)	2	0	2.0(2)
1	−0.10(1)	1	4.4(7)	2	1	−7.0(4)
2	0.067(9)	2	5.0(7)	2	2	−3.8(4)
3	3.31(6)	3	3(2)	2	−1	21.8(6)
4	0.02(1)	4	−5(1)	2	−2	8.8(4)
−1	0.35(1)	5	−2(65)	4	0	−3.3(2)
−2	−0.143(8)	6	3(1)	4	1	0.9(3)
−3	−1.16(4)	−1	−6.9(8)	4	2	−12.7(4)
−4	−0.53(1)	−2	3(7)	4	3	18.3(5)
		−3	−18(3)	4	4	−10.1(3)
		−4	−9(9)	4	−1	5.9(3)
		−5	−23(7)	4	−2	−14.7(3)
		−6	7(1)	4	−3	−17.3(1)
				4	−4	−12.9(1)

For indices l_1, l_2, l, m_2, symbol $g_{l,m,3}$ as well as the conventional Stevens parameters ($B_{l_2=4}^{m_2}$ and $B_{l_2=6}^{m_2}$), see Mombourquette et al. (1986).

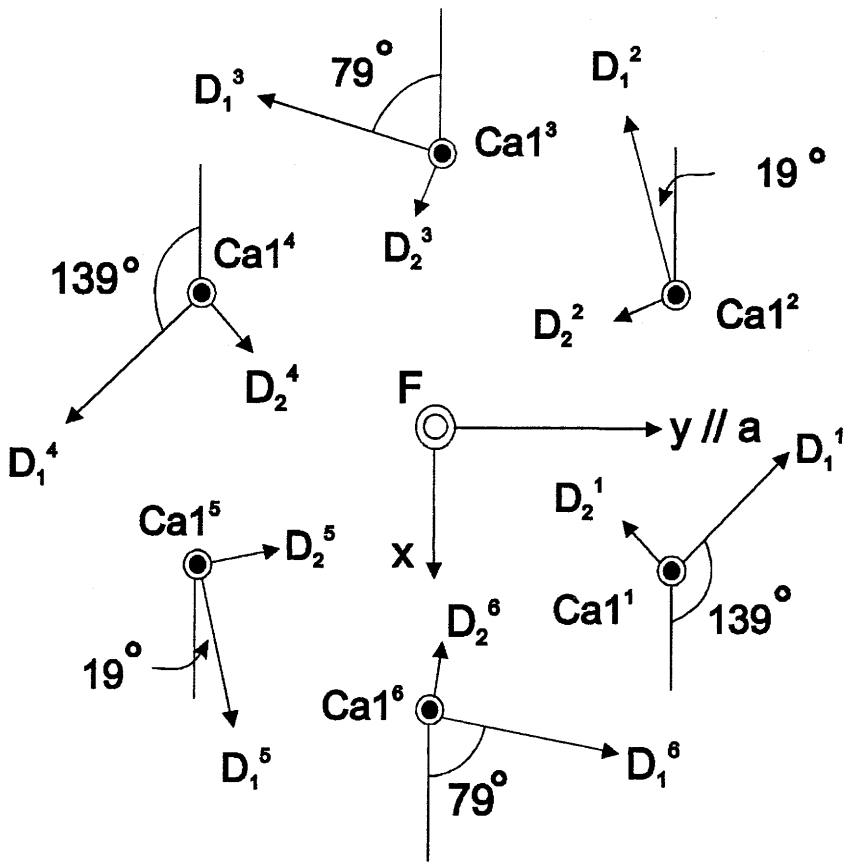

Figure 3.6. Projection along the crystallographic c axis of the principal directions of D_1 and D_2 of the six symmetry-related matrices **D** of the centre 'b' at T = 287 K at the six symmetry-related Ca1 sites (Fig. 2.1). Note that the sites $Ca1^1$ and $Ca1^4$, $Ca1^2$ and $Ca1^5$, and $Ca1^3$ and $Ca1^6$ are magnetically equivalent in the xy plane.

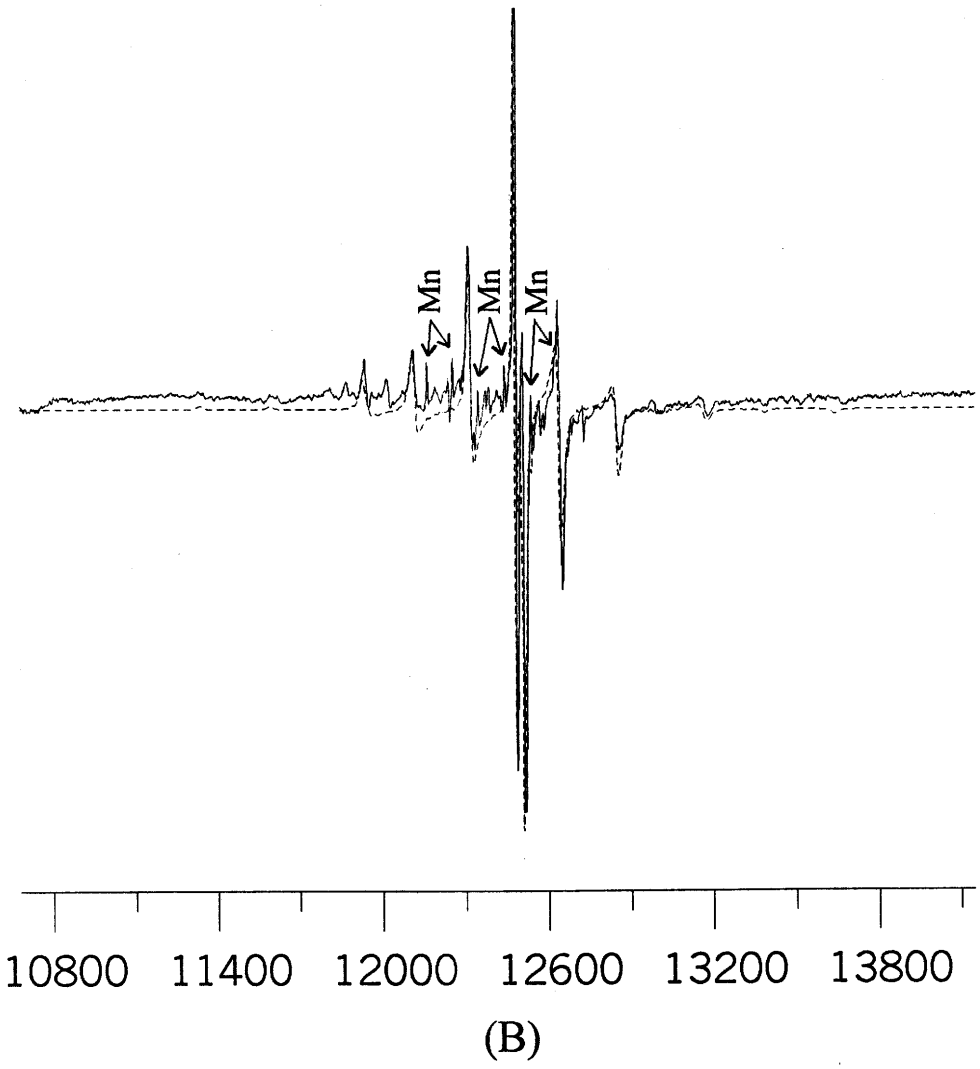

Figure 3.7. Observed (solid line) and simulated (dashed line) Q-band powder EPR spectrum of Gd-doped fluorapatite at the experimental frequency ν = 34.7983 GHz and temperature 298 K [simulation: lorentzian lineshape and various effective linewidths for the "allowed" transitions for the centres 'a' and 'b', concentration ratio a/b = 3.32] Note that one set of impurity Mn^{2+} sextets is shown explicitly.

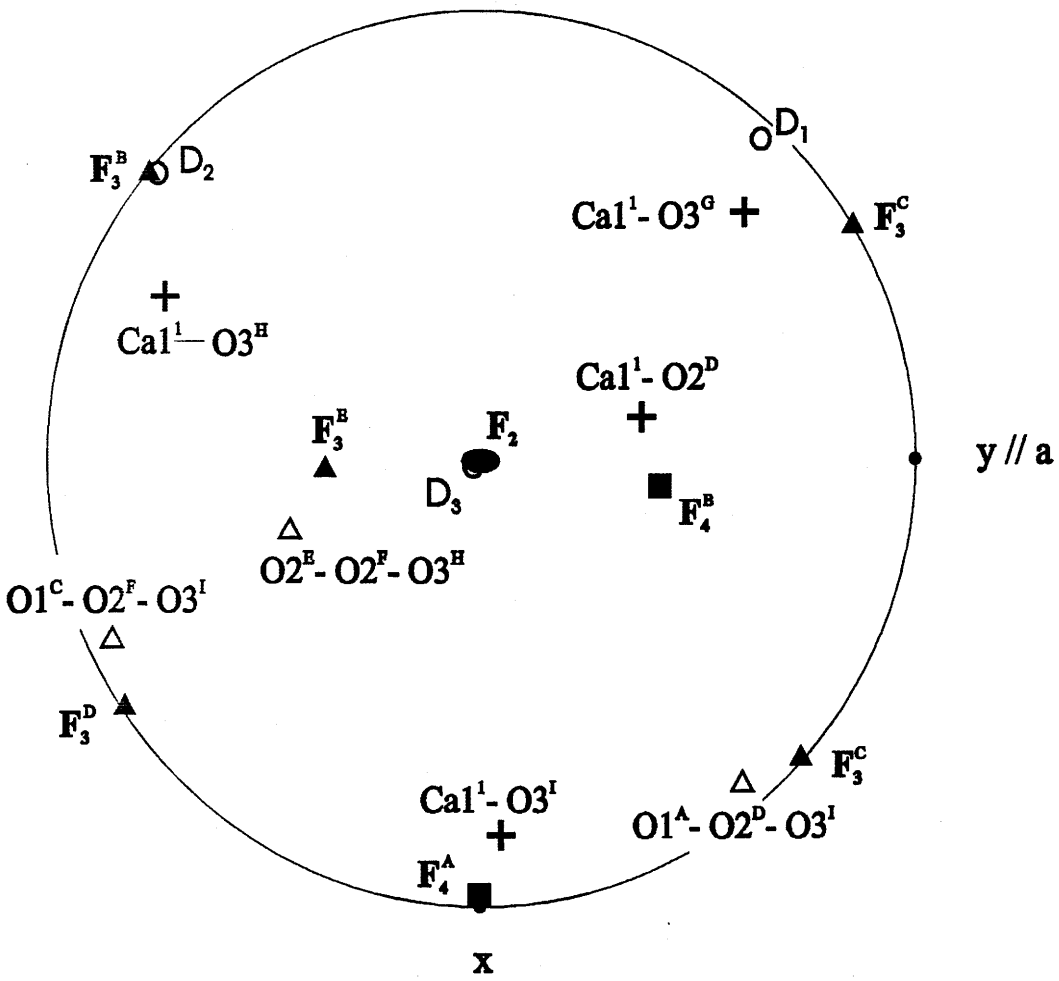

Figure 3.8. Stereographic projection(c//z) of the calculated pseudo-symmetry axes (solid ellipse, two-fold; solid triangles, three-fold; solid square, four-fold) of the Gd^{3+} centre 'b'. Note that the calculated pseudo-symmetry axes match closely to the principal directions of the matrix **D** (open circles), selected bonds (pluses) $Ca1^{1}$-$O2^{D}$, $Ca1^{1}$-$O3^{I}$ $Ca1^{1}$-$O3^{G}$ and $Ca1^{1}$-$O3^{H}$, and the normal directions of the faces (open triangles) $O1^{A}$-$O2^{D}$-$O3^{I}$, $O1^{C}$-$O2^{F}$-$O3^{I}$ and $O2^{E}$-$O2^{F}$-$O3^{H}$ of the $Ca1^{1}$ coordination polyhedron (Fig. 2.2b).

3.3.4 Pseudo-symmetry analysis

The assignment of the Gd^{3+} ions of the centre 'b' to the Ca1 sites has been evaluated further by a pseudo-symmetry analysis of the fourth-degree term S^4 of the spin-hamiltonian (e.g., Michoulier and Gaite, 1972; Gaite, 1980; 1987; Gaite et al., 1985; Mombourquette et al., 1986), using the program ROTSTO (Tennant et al., 2000) and following the method discussed in Chapter 2. The pseudo-symmetry analysis (i.e., the pseudo-cubic method), which was originally developed to study the deviation from a cubic symmetry, i.e., so-called pseudo-cubic site symmetry, has been applied here to the study of the highly rhombic local environment of the Gd^{3+} centre 'b' in fluorapatite. Figure 3.8 summarizes the results of the pseudo-symmetry analysis for the Gd^{3+} centre 'b', in the upper hemisphere ($0 \leq \theta \leq 90°$, $0 \leq \varphi < 360°$) of a stereographic projection, along with the direction projections for the bonds and face-normals of the coordination polyhedron of the $Ca1^1$ site (Fig.2.1) calculated from the x-ray data for pure fluorapatite (cf. Hughes et al., 1989). A two-fold pseudo-symmetry axis ($\mathbf{F}_2$) is present near the c axis (at polar coordinates $\theta = 1°$, $\varphi = 178°$). This pseudo-symmetry axis is inconsistent with the three-fold symmetry axis expected for an ideal Ca1 site (cf. Hughes et al., 1989), but can be explained by distortion related to the suggested mechanism for incorporating Gd^{3+} into this site (see below). Four three-fold pseudo-symmetry axes ($\mathbf{F}_3^A$, $\mathbf{F}_3^B$, $\mathbf{F}_3^C$, and $\mathbf{F}_3^D$; Table 3.5) are present on the great circle (Fig. 3.8). The axis $\mathbf{F}_3^A$ matches approximately the directions of the bond $Ca1^1$-$O3^G$ and the D_1 axis. The axis $\mathbf{F}_3^B$ almost coincides with the direction of D_2 but matches approximately the bond $Ca1^1$-$O3^H$. The axes $\mathbf{F}_3^C$ and $\mathbf{F}_3^D$ match approximately the normal directions of the faces $O1^A$-$O2^D$-$O3^I$ and $O1^C$-$O2^F$-$O3^I$, respectively. Another three-fold pseudo-symmetry axis

($\mathbf{F}_3^E$) corresponds approximately to the normal direction of the $O2^E$-$O2^F$-$O3^H$ face (Table 3.5 and Fig. 3.8). Two four-fold pseudo-symmetry axes ($\mathbf{F}_4^A$ and $\mathbf{F}_4^B$) match approximately the $Ca1^1$-$O3^I$ and $Ca1^1$-$O2^D$ bonds, respectively (Table 3.5 and Fig. 3.8). Therefore, the calculated pseudo-symmetry elements (Fig. 3.8) correspond closely to selected bonds and faces of the CaO_9 coordination polyhedron at the $Ca1^1$ sites (Fig. 2.1), as well as the principal directions of the matrix **D**, strongly supporting the site assignment of the Gd^{3+} ions of the centre 'b' to the Ca1 sites.

Admittedly, the basis for the calculated pseudo-symmetry elements of this study may be relatively weak (e.g., compared to those of Mombourquette et al., 1986), because the ideal Ca1 site in fluorapatite deviates significantly from a cubic or pseudo-cubic symmetry for which the pseudo-symmetry analysis is best suited (Michoulier and Gaite, 1972; Gaite, 1980; 1985; Mombourquette et al., 1986; Chapter 2). However, our results appear to be rational. Also, some of the angles between the calculated pseudo-symmetry axes and the bonds and faces of the ideal CaO_9 coordination polyhedron as well as the principal directions of D_1 and D_2 (Table 3.5) are probably attributable to the significant distortion in the local symmetry of the Gd^{3+}-occupied Ca1 site (see below).

TABLE 3.5 Comparison of the calculated pseudo-symmetry elements with the principal directions of the matrix **D** of the Gd^{3+} centre 'b' with selected bonds and faces of the CaO_9 coordination polyhedron at the $Ca1^{1}$ site.

Pseudo-symmetry elements		Directions		Principal D axes [a]	Directions		Ω (°)
		θ (°)	φ (°)		θ (°)	φ (°)	
F_2	2 fold	1	358	D_3	3	340	2
F_3^A	3 fold	90	123	D_1	87	140	17
F_3^B	3 fold	90	231	D_2	89	230	1
				Bond [b]			
F_3^A	3-fold	90	123	$Ca1^1$-$O3^G$	80	133	10
F_3^B	3-fold	90	231	$Ca1^1$-$O3^H$	80	253	24
F_4^A	4-fold	89	356	$Ca1^1$-$O3^I$	80	13	19
F_4^B	4-fold	45	88	$Ca1^1$-$O2^D$	45	112	17
				Polyhedron face [c]			
F_3^C	3-fold	90	51	$O1^A$-$O2^D$-$O3^I$	88	72	9
F_3^D	3-fold	90	304	$O1^C$-$O2^F$-$O3^I$	88	292	13
F_3^E	3-fold	40	270	$O2^E$-$O2^F$-$O3^H$	50	292	18

The Ω is the angle between the directions of the pseudo-symmetry elements and [a] the directions of the principal D axes, [b] the bonds of the site coordination, or [c] the face of the coordination polyhedron (Fig. 3.8).

3.3.5 Association between Gd^{3+} ion and Ca^{2+} vacancy

A likely mechanism for incorporating Gd^{3+} ions into the Ca1 sites in the synthetic fluorapatite is: $2Gd^{3+} + \square \Leftrightarrow 3Ca^{2+}$ (i.e., a Gd^{3+} -- $\square$ --- Gd^{3+} arrangement). The symbol $\square$ indicates a vacancy region arising from the absence of a Ca^{2+} ion. In this region, the missing of a Ca^{2+} ion results in a total charge number of minus two at this ion's equilibrium position. This residual charge meets the necessary local charge-balance requirement. Since the two Gd^{3+} ions do not necessarily have the same distance to the equilibrium position of the vacancy (see below), the symbol -- $\square$ --- is used to indicate the possible difference in distances. As discussed above, the Gd^{3+} ions in centre 'b' is thought to correspond to occupation at the Ca1 sites. An interesting question that then arises is the likely location of $\square$. A location of the vacancy at the nearest Ca1 neighbor (i.e., $Ca1^1$ at z = 1/2) is unlikely, because this arrangement would have preserved the triad axis of the ideal Ca1 site, inconsistent with the rhombic feature of the observed D matrix or the results of the pseudo-symmetry analysis. A possible model is that this vacancy is located at the Ca2 neighbour site nearest to a Gd^{3+}-substituted Ca1 site (e.g., $Ca2^1$ -- $Ca1^1$; Fig. 1.1).

The location of the vacancy associated with the Gd^{3+}-occupied Ca1 site, at the nearest Ca2 site, is supported both by the principal directions of the observed matrix **D** and by the results of the pseudo-symmetry analysis. The coordination polyhedron of the ideal Ca1 site in fluorapatite is elongated parallel to the crystallographic c axis and this closely matches the measured direction $\mathbf{D}_3$. The (small) deviation of $\mathbf{D}_3$ from the c axis (Table 3.3) probably is caused by the vacancy at the nearest Ca2 site. Such a vacancy would cause a substantial displacement of atom $O3^H$ (that is shared by $Ca1^1$ and $Ca2^1$;

Fig. 1.1) away from the $Ca2^1$ site toward the $Ca1^1$ site. This distortion can readily explain the deviation of the D_3 direction from the crystallographic c axis and the large differences in the fitted D_1 and D_2 values ($D_1/D_2 = 13$; Table 3.3), which would be expected to be equal for the ideal Ca1 site (Hughes et al. 1989). Also, the displacement in $O3^H$ results in replacement of the vertical three-fold rotation axis at the ideal Ca1 site (Hughes et al. 1989) by an approximately vertical two-fold pseudo-symmetry axis revealed by the pseudo-symmetry analysis for the centre 'b', which is equivalent to the approximate horizontal mirror plane (Fig. 3.8). The principal $\mathbf{D_3}$ direction also matches the expectation of the superposition model (Brodbeck and Bukrey 1981; Kliava 1982; Gaite et al., 1985; Mombourquette and Weil 1987), which suggests that direction $\mathbf{D_3}$ reflects the elongation of the coordination polyhedron within which the paramagnetic ion resides.

The location of the second Gd^{3+} ion in the proposed Gd^{3+} -- □ --- Gd^{3+} arrangement remains uncertain but this cation must be well separated from the first Gd^{3+} ion, on the basis of absence of any observed magnetic dipolar interactions between neighboring Gd^{3+} ions. Note that the location of the vacancy at a neighboring Ca2 site is expected to lead to slightly different distortions of the two Gd^{3+}-occupied Ca1 sites, and hence different principal directions for their D matrices. This effect may explain the broader inherent linewidth of the W-band EPR spectra for Gd^{3+} at the Ca1 sites, as compared to that of Gd^{3+} at the Ca2 sites, which does not involve any vacancy and hence shows no such effect.

3.3.6 Comparison of the Gd^{3+} centres 'a' and 'b' in fluorapatite

The D and E values of centre 'b' at the Ca1 sites are significantly larger than those of centre 'a' at the Ca2 sites (Table 3.3), although both these Gd^{3+} centres have rhombic local symmetry. Hughes et al. (1989) pointed out that the ideal Ca2 site is an approximate CaO_5F octahedron, although a weak Ca2-O1 bond also exists (Fig. 1.2). The study included in Chapter 2 (Chen et al., 2001a) showed that the substitution of Gd^{3+} into a Ca2 site is accompanied by a replacement of F^- by O^{2-}, which may have increased the resemblance of the Ca2 polyhedron to an octahedron. The ideal CaO_9 polyhedron at the Ca1 sites, on the other hand, is highly elongated along the c axis (Hughes et al. 1989). Moreover, the involvement of a vacancy in the incorporation of Gd^{3+} into the Ca1 sites also introduces substantial distortions. Therefore, the larger D and E values of centre 'b' at the Ca1 sites compared to 'a' at the Ca2 sites presumably are attributable to differences in the local symmetries of the ideal Ca1 and Ca2 sites and to the distortions introduced by the incorporation of Gd^{3+}.

The relative abundance of the two Gd^{3+} centres at the Ca1 and Ca2 sites in fluorapatite has been estimated by simulation of the W-band single-crystal spectrum at **B//z** and $\mathbf{B}_1$**//x**. First each "allowed" transition from the two Gd^{3+} centres was simulated separately, with lorentzian lineshape but different linewidths. Then the lines from the different transitions were summed to obtain the two spectra from the Gd^{3+} centres at the Ca1 and Ca2 sites. Finally the two spectra were added together by trial and error using different intensity ratios to match the measured spectrum (Fig. 3.3a). The intensity ratio between the two Gd^{3+} centres at the Ca2 and Ca1 sites was found to be 0.29, corresponding to a site-occupancy ratio (REE-Ca2/REE-Ca1) of 0.19, since the

multiplicities of the Ca1 and Ca2 sites are 4 and 6, respectively. This site-occupancy ratio from the EPR spectra is similar to that found in a Gd-rich fluorapatite (10.36 wt% Gd_2O_3) from x-ray structure refinement (REE-Ca2/REE-Ca1 = 2.0; Fleet and Pan 1995), although the latter material was synthesized hydrothermally at much lower temperature (~700° C) and contained charge-compensating Na^+ and Si^{4+} ions [eq. (3)-(6), Chapter 2] for the incorporation of Gd^{3+} (Fleet and Pan 1995).

3.4 Conclusions

A general spin-hamiltonian, including the matrices **g** and **D** and the high-spin terms of type S^4, S^6 as well as BS^3 and BS^5, has been estimated for a previously unreported Gd^{3+} centre 'b' in synthetic fluorapatite by analyzing well-resolved single-crystal even-isotope W-band EPR spectra in three orthogonal rotation planes. The validity of this spin-hamiltonian has been confirmed by agreements between the observed and simulated single-crystal spectra. The matrices **g** and **D** and the results of a pseudo-symmetry analysis for the term S^4 all suggest that this Gd^{3+} centre 'b' corresponds to a substitution at the Ca1 site and that its local symmetry is strongly rhombic. Moreover, the principal directions of the matrix **D** and the local structural environment of this Gd^{3+} centre 'b' suggest that the substitution mechanism for the incorporation of Gd into the Ca1 site is $2Gd^{3+} + \square \Leftrightarrow 3Ca^{2+}$ and has an arrangement of the type Gd^{3+} -- □ -- Gd^{3+} with the vacancy at a neighboring Ca2 site next to one of the Gd^{3+}-occupying Ca1 sites (i.e., $Ca2^k$ to $Ca1^k$, k = 1, 2 ...6).

CHAPTER 4

^{157}Gd Hyperfine Structure Anisotropy and Nuclear Quadrupole Effect of the Gd^{3+} Centre 'a'

4.1 Introduction

Hyperfine structure (HFS) arises from magnetic interaction between the electron spin and the nuclear spin of paramagnetic centres that have non-zero nuclear spin numbers (I). Gadolinium, which commonly occurs in the trivalent state with an electron spin S = 7/2, contains the following isotopes: ^{152}Gd, ^{154}Gd, ^{155}Gd, ^{156}Gd, ^{157}Gd, ^{158}Gd and ^{160}Gd. The even-isotope Gd^{3+} nuclides have I = 0, and don't exhibit HFS, whereas $^{155}Gd^{3+}$ and $^{157}Gd^{3+}$ have I = 3/2 and may exhibit HFS in electron paramagnetic resonance (EPR) spectra. Two previous EPR studies of fluorapatite crystals doped with ordinary Gd_2O_3, at X- and W-band frequencies (9.5 and 94 GHz, respectively) yielded the EPR spectral fine structures of the two paramagnetic centres 'a' and 'b' but did not show any evidence of HFS (Chen et al. 2001a,b). This absence of HFS was tentatively attributed to the low natural abundances of the two odd isotopes relative to their even counterparts (Chen et al. 2001a,b). One major objective of the present study is, therefore, to investigate the HFS of the Gd^{3+} EPR spectra of the centres by measuring fluorapatite crystals doped with ^{157}Gd-enriched Gd_2O_3 at both X- and W-band frequencies (cf. Chen et al. 2001a,b).

The full spin-hamiltonian for a paramagnetic centre involving an odd-isotope Gd^{3+} nuclide can be expressed (Buckmaster et al. 1972, 1981) as:

$$\mathcal{H} = \sum_{l_1,l_2,l_3} \sum_{l} \sum_{m=-l}^{+l} a_{l,m}^{l_1,l_2,l_3} \; T_{l,m}^{l_1,l_2,l_3}(\mathbf{B},\mathbf{S},\mathbf{I}). \qquad (1)$$

The parameters of the spin-hamiltonian terms related to the even Gd isotopes (Table 4.1) have been determined quantitatively for the centres 'a' and 'b' from the Gd-doped fluorapatite (Chen et al. 2001a,b). For $^{155}Gd^{3+}$ and $^{157}Gd^{3+}$, the odd-isotope-related terms (Table 4.1) can be derived from equation (1) and expressed as:

$$\mathcal{H}_{HFS} = \mathbf{S}^{T}\cdot\mathbf{A}\cdot\mathbf{I} - \beta_n\mathbf{B}^{T}\cdot\mathbf{g}_n\cdot\mathbf{I} + \mathbf{I}^{T}\cdot\mathbf{P}\cdot\mathbf{I} + \cdots . \qquad (2)$$

where $\mathbf{I}$ is the nuclear spin-vector operator, and $\mathbf{A}$, $\mathbf{g}_n$ and $\mathbf{P}$ are 3×3 real matrices representing the hyperfine, nuclear Zeeman and nuclear electric-quadrupole effects for the nuclide at hand, respectively. Here β_n is the nuclear magneton, and superscript T denotes transposition of matrix. Quantitative determination of these parameters is a powerful tool for providing detailed information about the local geometric configuration of the paramagnetic centres and the distribution of the nuclei and unpaired electron(s) in them (Weil et al. 1994).

The results reported herein show that the ^{157}Gd HFS of centre 'a' is well resolved in both X- and W-band experiments. Therefore, the X-band hyperfine spectra from a well-oriented crystal, together with the spin-hamiltonian parameters obtained from the even isotopes (Chen et al. 2001a), were used to determine the parameter matrices $\mathbf{A}$, $\mathbf{P}$ and $\mathbf{g}_n$. To the best of our knowledge, this is the first determination of $\mathbf{P}$ and $\mathbf{g}_n$ for Gd^{3+} centres in single-crystal EPR studies. These matrices were used to provide further details

on the local geometric configurations of 'a' and the distribution of the nuclei and unpaired electrons of the Gd^{3+} ion in 'a'.

Another major objective of this study is to evaluate the effects of the other spin-hamiltonian terms besides the hyperfine term **A** on the observed hyperfine splitting arising from centre 'a' in ^{157}Gd-doped fluorapatite. Minge and Weil (1989) showed that the "anomalous" behavior (i.e., apparent anisotropy) of the ^{57}Fe HFS given by the centre $[FeO_4/Li]^0$ in α–quartz is caused by the transfer of the effects of the anisotropy due to the matrix **D**. In fact, the hyperfine parameter is isotropic, derived from an 'isotropic matrix' **A** (i.e., **A** = **AU**, where **U** = 3×3 unit matrix). The present study shows, for the first time, that other spin-hamiltonian terms of type S^4, S^6, BS, BS^3 and BS^5 also can make important contributions to the observed angular hyperfine splitting anisotropy.

Although there are a lot of terms allowed by the physical situation of Gd^{3+} (S =7/2 and I = 3/2), we neglect most of them (Table 4.1), assuming that they are negligibly small. One major reason for this is the parameter proliferation among the parameters of these terms, causing difficulties in the fitting convergence.

TABLE 4.1. List of the allowed spin-hamiltonian terms for the case S = 7/2, I = 3/2. Here integers l_1, l_2 and l_3 label the terms involving the Zeeman magnetic field, electronic spin operator, and nuclear spin operator, respectively.

Terms	l_1	l_2	l_3	
BS (**g**)	1	1		Electronic Zeeman term
BS^3	1	3		Electronic Zeeman high-spin term
BS^5	1	5		Electronic Zeeman high-spin term
BS^7	1	7		*
BI ($\mathbf{g}_n$)	1		1	Nuclear Zeeman term
BI^3	1		3	*
S^2 (**D**)		2		Electronic electric quadrupole term
S^4		4		Electronic electric octupole term
S^6		6		Electronic electric hexadecapole term
I^2 (**P**)			2	Nuclear electric quadrupole term
BSI^2	1	1	2	* #
BS^2I	1	2	1	* #
BS^2I^3	1	2	3	* #
BS^3I^2	1	3	2	* #
BS^4I	1	4	1	* #
BS^4I^3	1	4	3	* #
BS^5I^2	1	5	2	* #
BS^6I	1	6	1	* #
BS^6I^3	1	6	3	* #
BS^7I^2	1	7	2	* #
SI (**A**)		1	1	Hyperfine term
SI^3		1	3	*
S^2I^2		2	2	*
S^3I		3	1	*
S^3I^3		3	3	* #
S^4I^2		4	2	*
S^5I		5	1	*
S^5I^3		5	3	* #
S^6I^2		6	2	* #
S^7I		7	1	*
S^7I^3		7	3	* #
Terms quadratic or higher in B ($l_1 > 1$) also exist.				* #

* Term deemed to be negligible and thus was ignored in our work.

\# Here, decomposition algebra does not generally exist, except in some high-symmetry (cubic/tetragonal) cases. This refers to all operator combinations $B^pS^qI^r$ and all perator couples $J_1^qJ_2^r$, where $q + r > 8$.

4.2 Experimental Methods

4.2.1 Synthesis and characterization of ^{157}Gd-doped fluorapatite crystals

Single crystals of ^{157}Gd-doped fluorapatite were synthesized by using procedures similar to those described in Chen et al. (2001a), except that ^{157}Gd-enriched Gd_2O_3 [^{152}Gd 0.02(1)%; ^{154}Gd 0.085(30)%; ^{155}Gd 0.615(30)%; ^{156}Gd 1.76(10)%; ^{157}Gd 93.62(7)%; ^{158}Gd 3.10(3)% and ^{160}Gd 0.82(1)%] obtained from the Oak Ridge National Laboratory, Tennessee, USA, was used to provide a ^{157}Gd concentration of approximately 100 parts per million (ppm). The crystals of the ^{157}Gd-doped fluorapatite are similar in size and optical properties to those described in Chen et al. (2001a,b). Laser ablation - inductively coupled plasma mass spectrometry analyses, using the well-characterized Durango fluorapatite as a standard (Pan et al. 1993), confirmed a homogeneous distribution of ^{157}Gd at 97±6 ppm.

4.2.2 EPR experiments

Single-crystal X-band EPR spectra of the ^{157}Gd-doped fluorapatite were measured on a Bruker ESP300 spectrometer at the Department of Chemistry, University of Saskatchewan. A hexagonal prismatic crystal of the ^{157}Gd-doped fluorapatite was mounted on a three-sided holder and was aligned by use of the Laue x-ray method (Amoros et al. 1975). This x-ray diffraction analysis also confirmed that the selected crystal of the ^{157}Gd-doped fluorapatite is free of twinning. The holder was glued to a cylindrical jacket containing DPPH (i.e., free-radical powder 2,2-diphenyl-1-picrylhydrazyl) as the standard for the magnetic-field calibration, which allowed simultaneous EPR measurements of the standard and the ^{157}Gd-doped fluorapatite crystal (Chen et al. 1999, 2001a).

Field-swept X-band EPR experiments were performed at 5° and 10° intervals with the magnetic field **B** in three orthogonal rotation planes, by consecutively attaching the three sides of the crystal-bearing holder to the goniometer by use of vacuum grease (Chen et al. 1999). In these three rotations, the axes **z** and **y** of the ideal experiment system were chosen along the crystallographic axes **c** and **a** (one of three equivalent axes $\mathbf{a}_1$, $\mathbf{a}_2$, $\mathbf{a}_3$ of the crystal system) and the direction of the axis **x** is defined to be $\mathbf{y} \otimes \mathbf{z}$ with the signs of **c** and **a** chosen arbitrarily. Because of the unavoidable (small but not negligible) error in crystal alignment, the actual experimental axes are herein referred to as **x"**, **y"** and **z"** (i.e., the rotation planes for **B** are x"y", y"z" and x"z"; Fig. 4.1). The X-band spectra with **B** in plane x'y' were collected at an average temperature of 295(1) K and a spectral resolution of 0.05 G (i.e., 1024 field data points over 50 G in each spectrum), whereas those in planes x"z" and y"z" were measured at similar temperatures but lower spectral resolutions of 0.1 G (i.e., 1,024 field data points over 100 G in each spectrum). The average microwave frequencies were 9.023(2), 9.250(1) and 9.246(3) GHz for the planes x"y", y"z" and x"z", respectively. The actual coordinate system was obtained as discussed below.

Single-crystal W-band EPR spectra were obtained on the MARK II W-band (94 GHz) EPR spectrometer (Nilges et al. 1999) at the Illinois EPR Research Center. Similar to the experiment described in Chen et al. (2001b), field-swept measurements in plane x"y" (i.e., $\mathbf{B} \perp \mathbf{z}$") were made on a prismatic crystal of ^{157}Gd-doped fluorapatite, which was mounted in a quartz tube of 0.7 mm internal diameter and aligned inside the resonant cavity viewed under binoculars. Here, coordinates x", y" and z" denote the actual coordinate system in the W-band experiments. For measurements in planes x"z"

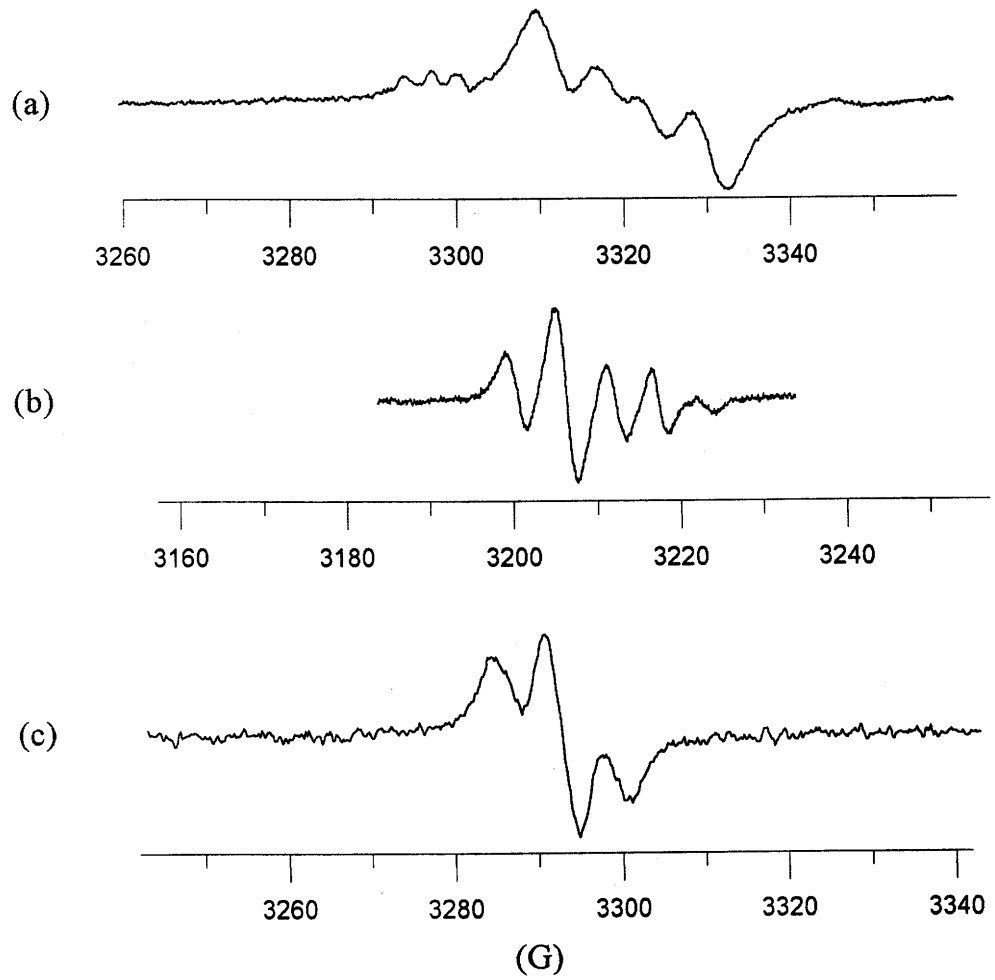

Fig. 4.1. X-band single-crystal spectra of the ^{157}Gd-doped fluorapatite: (a) **B//z "** and $\mathbf{B}_1$**//x"** at 9.247808(1) GHz and 295.0 K; here $\mathbf{B}_1$ is the excitation field; (b) **B//x"** and $\mathbf{B}_1$**//z"**; at 9.022369(2) 117.4 K; and (c) **B//y"** and $\mathbf{B}_1$**//x"** at 9.250159(1) GHz and 295 K. Note that the HFS is visible for m_S values $+1/2 \leftrightarrow -1/2$ at all three directions. Especially along the axes z" and x", the HFS is well resolved, but at **B//x"** existing a four-line structure because of peak interference between two HFS caused by magnetic site splitting (Chapter 3). At **B//y"**, a peak combination caused by the nuclear-quadrupole effect results in a three-line structure.

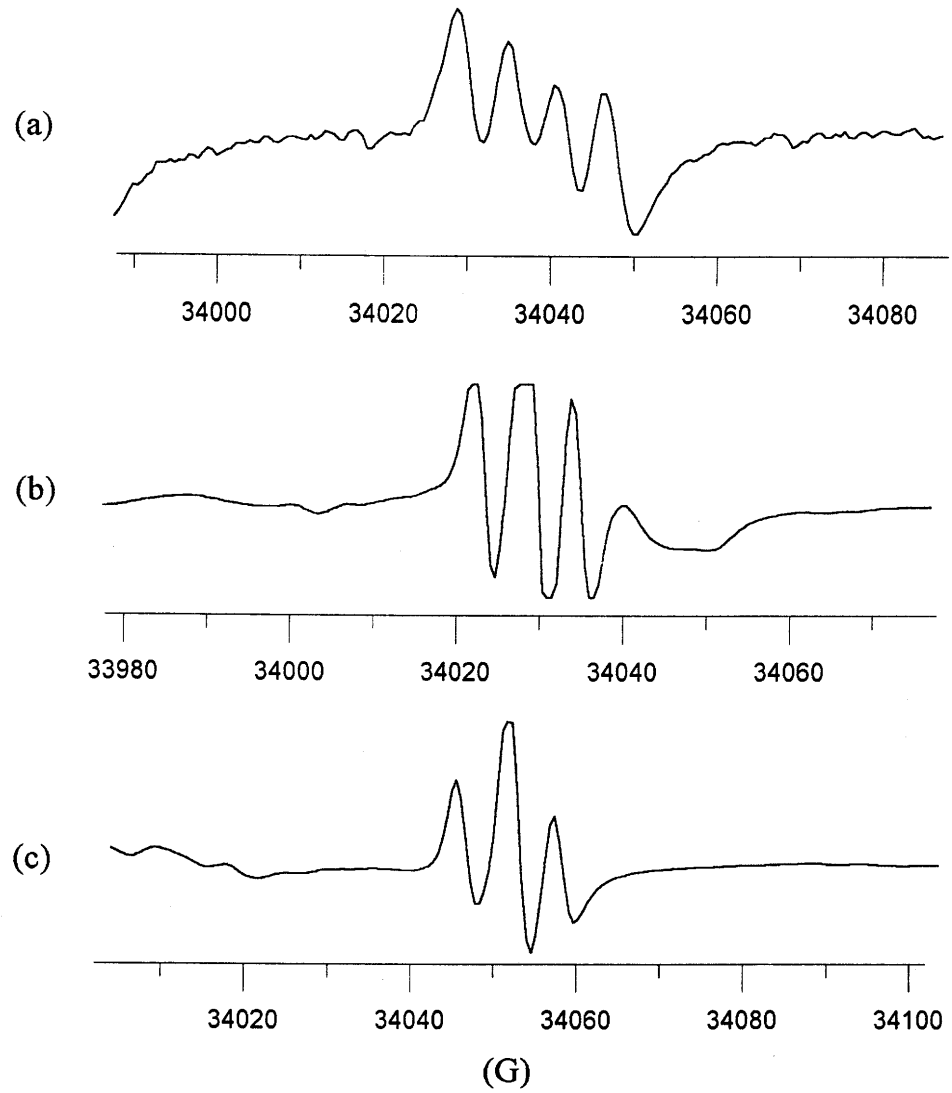

Figure 4.2. W-band single-crystal EPR spectra of the ^{157}Gd-doped fluorapatite at 296K: a) **B**//z" and $\mathbf{B}_1$//x"; at 94.4309 GHz; (b) **B**//x" and $\mathbf{B}_1$//z"; at 94.4162 GHz; and (c) **B**//y" and $\mathbf{B}_1$//x"; 94.4989 GHz. Note that the HFS is visible for the transitions $m_S - 1/2 \leftrightarrow +1/2$ at all three directions in the W-band spectra. The existing four-line- (at **B**//z" and **B**//x") and three-line- (at **B**//y") structures in the W-band spectra similar to that observed in the X-band EPR.

and y"z", the same crystal of ^{157}Gd-doped fluorapatite was mounted using Duco cement on a quartz rod (0.78 mm diameter), which was glued directly to the resonant cavity using the same cement. Alignment was made approximately by use of a well-developed crystal face and a crystal edge of the hexagonal prism as references for planes x"z" and y"z", respectively. Field-swept W-band EPR experiments with the Zeeman field **B** rotated in the three orthogonal planes were carried out at average frequencies 94.40(6), 94.47(1) and 94.45(2) GHz for planes x"y", x"z" and y"z", respectively. The spectral resolution was 0.6 G (i.e., 2048 field data points over 1150 G in each spectrum), and the angle intervals were 10° in all three planes. The initial B-field calibration of the W-band spectrometer was done by use of a Metrolab NMR Telsa Gaussmeter PT2025 (Nilges et al. 1999). This calibration was improved somewhat by comparison, for the centre 'a', of the observed even-isotope line positions in the W-band experiments and those predicted by the spin-hamiltonian parameters derived from the well-calibrated **B** fields in the X-band experiments (Chen et al. 2001a).

4.3 Results and Discussions

4.3.1 EPR spectra

The single-crystal X-band EPR spectra of the ^{157}Gd-doped fluorapatite exhibit a well-resolved four-line HFS when **B** is close to the z axis (Fig. 4.1a). This HFS has been shown by spectrum simulation to arise from the centre 'a', i.e., Gd^{3+} ions at the Ca2 type of sites (cf., Chen et al. 2001a). Minor peak interference from the single-line fine structure of the even isotopes has been observed in the spectra with **B** close to the z axis (Fig. 4.1a) and confirmed by spectrum simulations (see below). At field orientations away from **z**, the HFS generally is reduced to three lines (e.g., Fig. 4.1c), due primarily

to the nuclear quadrupole effect. At **B//x**", interference exists among the HFS-component lines caused by magnetic site splitting (Fig. 4.1b; Chen et al. 2001a).

The HFS has also been observed in the single-crystal W-band EPR spectra of the ^{157}Gd-doped fluorapatite (Fig. 4.2). These peaks in the W-band spectra have narrower linewidths and thus higher spectral resolution than their counterparts in the X-band spectra (Figs. 4.1 and 4.2). Also, peak interference from the even isotopes in the W-band spectra is weaker (Figs. 4.1 and 4.2).

The single-crystal X-band EPR spectra of the ^{157}Gd-doped fluorapatite also disclosed a partly-resolved HFS (Fig. 4.1a), which has been shown by comparison of the fine structure to arise from the substitution of ^{157}Gd nuclide into the Ca1 type of sites (i.e., centre 'b'; Chen et al. 2001b). This HFS is characterized by a relatively weak three-line structure next to the HFS peaks of centre 'a' when **B** is close to **z** (see Fig. 4.1a), and has not been detected with **B** away from **z**.

At W-band, the HFS from centre 'b' displayed 2-line or 3-line structure, indicating strong nuclear quadrupole interaction. Also, for it, the principal directions of the matrices **A** and/or **P** appear to deviate significantly from the crystallographic coordinate system. These effects make quantitative analysis of the HFS for 'b' complicated; it was not attempted in this study.

4.3.2 Optimization of matrices A, P and g_n

The optimization of the spin-hamiltonian parameters for the spectral X-band HFS of the centre 'a' was performed first for matrix **A** and then for **P**, and followed by varying both matrices simultaneously through iterations involving single-crystal spectrum simulations, line-position fittings and angle corrections under the assumption

initially of an isotropic g_n of –0.2253 (Weil et al. 1994). Afterwards, the matrix $\mathbf{g}_n$ was allowed to vary in the parameter optimization (Table 4.2). All these calculations were carried out by use of a non-linear least-squares algorithm in the software package EPR-NMR (Mombourquette et al. 1996). In each step, continuing iteration was made until no changes at the last decimal point (the machine accuracy) of the root-mean-sum-of–squares of weighted differences (RMSD) between the calculated and fitted line positions. Both **A** and **P** were assumed to be symmetric (Mombourquette et al. 1996); thus the upper-triangular elements per matrix were determined. The numbers of line-position data points (transitions) used in the matrix fitting were 32, 80 and 128 for planes x"y", x"z" and y"z", respectively. Because line positions obtained from the single-crystal spectrum simulation were utilized in the fitting, all of the line positions were assumed to have the same level of accuracy, and therefore the same weighing factors were assigned to them in the optimization.

The optimization for the matrix **A** started from a rhombic diagonal matrix with the initial values of 5.25, 3.87 and 6.10 G for parameters A_{11}, A_{22} and A_{33}, respectively. These values were estimated by trial and error from single-crystal spectrum simulations with **B//x"**, **B//y"** and **B//z"** at experimental frequencies 9.022369, 9.250159 and 9.247808 GHz, respectively. All parameters in the initial matrix **P** were set artificially to zero. The spin-hamiltonian parameter set for the even-isotope Gd^{3+} nuclides occupying the $Ca2^1$ site [i.e., the terms of type BS (**g** matrix) and S^2 (**D** matrix) and the high-spin terms of type S^4, S^6 as well as BS^3 and BS^5 from Chen et al. (2001a)] was used throughout the single-crystal hyperfine spectrum simulations.

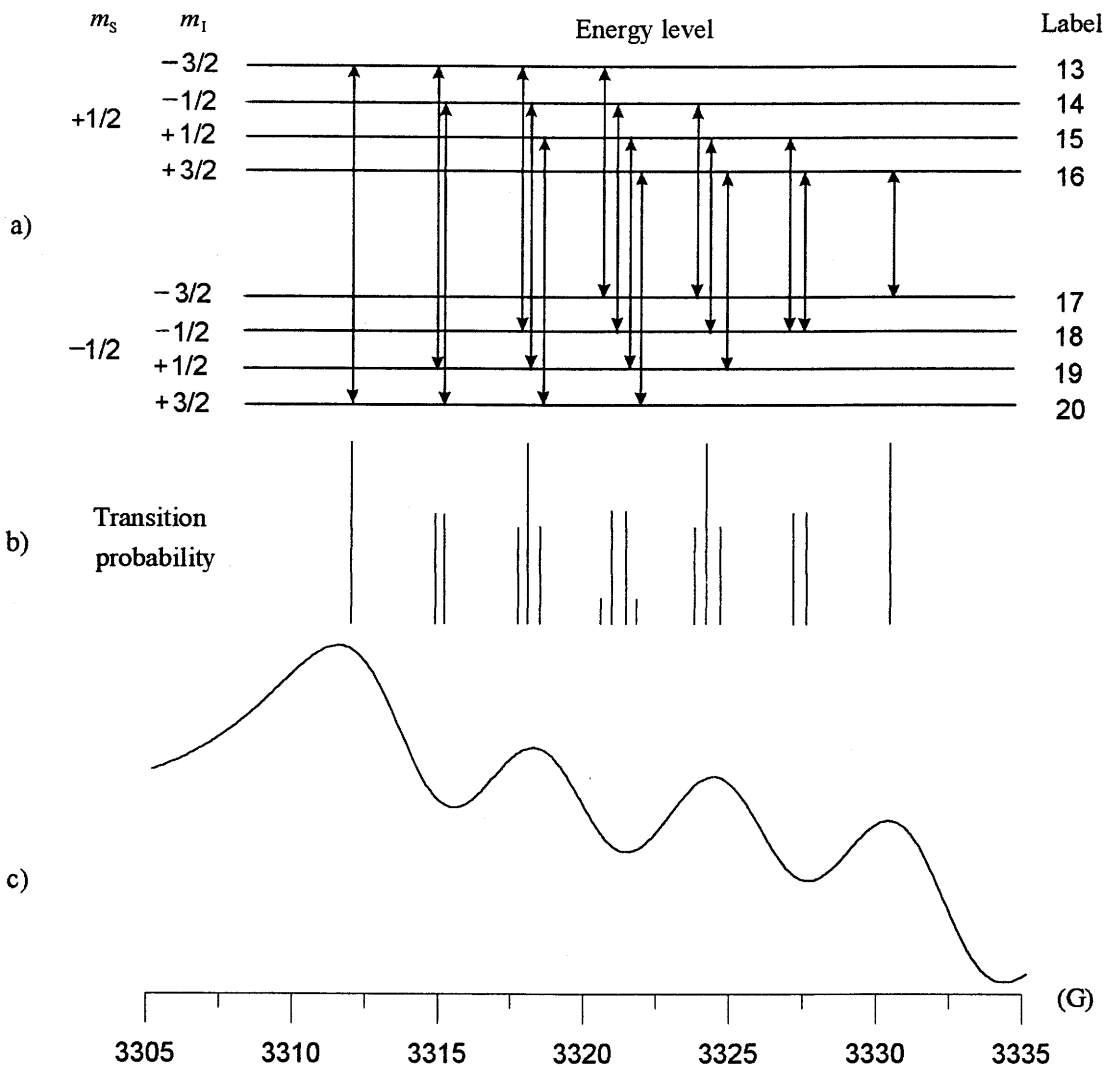

Figure 4.3. a) HFS energy diagrams and calculated possible transitions between m_S -1/2↔+1/2; b) calculated transition probabilities; c) simulated HFS of the single-crystal spectrum of ^{157}Gd in fluorapatite. Note that all calculations were made for the spectrum at **B//z'** and the line hights in b) correspond to the logarithm calculation of the real calculated transition probabilities.

The line positions for the optimization of the matrices **A** and **P** were estimated from single-crystal spectrum simulations for the observed spectra at directions other than **B//z"**, by trial and error. These simulations revealed that, among the 448 possible transitions from the 32 energy levels (label from 1 to 32) for $^{157}Gd^{3+}$ (S = 7/2, I = 3/2), only 16 transitions (label in Fig. 4.3) are responsible for the observed spectra [transitions between m_S values $+1/2 \leftrightarrow -1/2$). Therefore, only lines from these transitions were used in the optimization (Fig. 4.3, Table 4.3). In each iteration, several steps were taken, i.e., first a simulation was performed adopting **A** and **P** estimated from a previous iteration, and then the parameters in **A** were artificially adjusted by trial and error to match the simulated total splitting of the HFS to that of the observed one. Subsequently, the even-isotope spectrum was added according to the total abundance of even isotopes (5.785%) in the starting material Gd_2O_3, to obtain the complete spectrum, and this was then followed by artificially changing the parameters in **P** to match the relative intensities of each peak. Then **A** and **P** were changed simultaneously during the optimization process until satisfactory results were obtained. At this point, $\mathbf{g}_n$ was varied in the iteration process with or without a scalar restriction (Table 4.2), which was continued until no change in the last decimal point of the RMSD. The last step of the optimization was made by fitting **A**, **P** and $\mathbf{g}_n$ simultaneously, yielding a final RMSD of 0.12 G (Table 4.2). This final RMSD is much less than half of the linewidth (4.9 G, i.e., max-min of the 1st derivative) of the inherent individual hyperfine component lines measured by the single-crystal spectrum simulation and observed in the X-band spectrum at **B//x"**.

The errors in the crystal alignment were determined after the X-band experiments by using the software package EPR-NMR (Table 4.4). The normals to the

planes x"y", x"z", and y"z" were found to be ($\theta = 0°$, $\phi = 0$), (90.81°, 95.44°), and (88.81°, 182.12°), respectively. Note that no error was detected for the x'y' plane. The final spin-hamiltonian parameters were expressed in the ideal reference system xyz (Table 4.4).

The final calculated matrix **A** (Table 4.5) is rhombic. This has been confirmed by a fitting in which **A** was assumed to be isotropic while **P** and $\mathbf{g}_n$ were kept unchanged. A much bigger RMSD resulted (0.73 G; Table 4.2). Figure 4.4 shows that the principal directions of **A** match closely the local structural environment of the ideal $Ca2^1$ site (Hughes et al. 1989) and the pseudo-symmetry of the centre 'a' calculated from the terms of type S^4 (Chen et al. 2001a): the principal direction of A_1 is close to a 3-fold pseudo-symmetry axis, A_2 to the normal direction of the face $O3^F$-F-$O3^A$, and A_3 to the direction of the bond Ca2-O2.

The spin-hamiltonian parameter optimization showed that the centre 'a' possesses a non-zero matrix **P**. This result has been confirmed by a fitting for a zero **P** and an isotropic $\mathbf{g}_n$ ($g_n = -0.2143$), which resulted in an increased RMSD of 0.16 G (i.e., an increase by 30%; Table 4.2). The validity of **P** is also evident from the close match between its principal directions and the local structural environment of the ideal Ca2 site (see below).

The almost uniaxial nature of the matrix **P** (Table 4.5) indicates a nearly constant electric-field gradient in the horizontal mirror plane of the ideal Ca2 site (cf. Hughes et al. 1989). This "uniaxial" gradient behavior may be explained by the similar Ca2-F and Ca2-O2 bond distances in this plane (i.e., 2.311 and 2.374 Å, respectively; Hughes et al. 1989). Moreover, the replacement of F^- (radius 1.33 Å) by the larger O^{2-} ion (1.40 Å) accompanying the incorporation of Gd^{3+} into the Ca2 site (Chen et al. 2001a) is expected

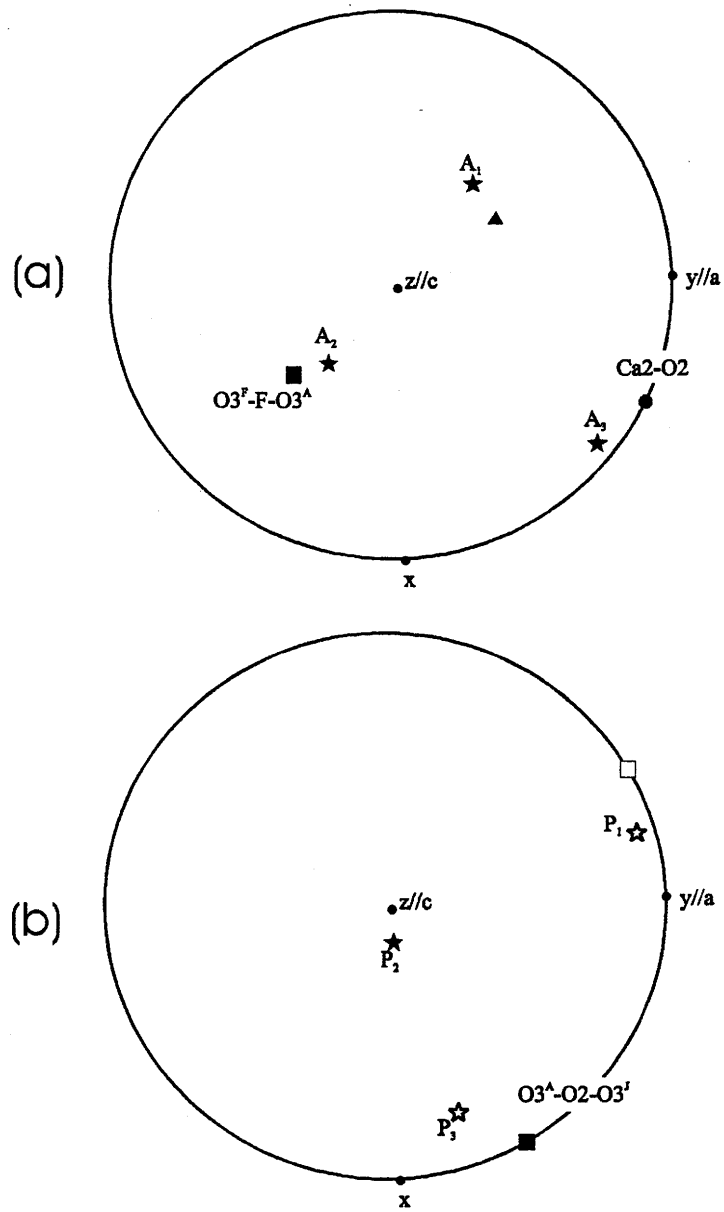

Figure 4.4. Stereographic projection illustrating: (a) the principal directions (solid stars) of **A** calculated from the X-band HFS (transitions between m_S values +1/2 −1/2) of the centre 'a^{1}' (Table 4.5) and (b) the principal directions (solid star, pole in the upper hemisphere; open star, poles in the lower hemisphere) of **P** of 'a^{1}' (Table 4.5), in comparison with the local structural environment of the ideal $Ca2^{I}$ site (large solid circle, Ca2-O2 bond; solid squares, normal directions of faces $O3^{F}$-F-$O3^{A}$ and $O3^{A}$-O2-$O3^{J}$; open square, horizontal bisector of the Ca2-$O3^{F}$ and Ca2-$O3^{I}$ bonds; labeling of oxygen atoms after Hughes et al. 1989) and a 3-fold pseudo-symmetry axis (solid triangle) calculated from the term of type S^{4} for 'a^{1}' (Chen et al. 2001a).

to further reduce the difference between the two bonds (e.g., Fleet and Pan 1995) and thus makes the coordination polyhedron in the horizontal plane more uniaxial. Hence the "uniaxial" nature of **P** offers further evidence for the suggested substitution mechanism at the Ca2 site (Chen et al. 2001a).

The principal directions of **P** match closely the local structural environment of the Ca2 site: i.e., the principal P_1 direction approximates the horizontal bisector between the Ca2-$O3^F$ and Ca2-$O3^I$ bonds (cf. Hughes et al. 1989), while the principal P_2 direction is close to the crystallographic c axis and matches approximately the vertical bisector between the Ca2-$O3^A$ and Ca2-$O3^F$ bonds (Fig. 4.4b). The principal P_3 direction is close to the normal direction of the $O3^A$-O2-$O3^J$ face (Fig. 4.4b). These data provide further evidence that centre 'a' corresponds to Gd at the Ca2 site (Chen et al. 2001a).

Moreover, $P_2/g_e\beta_e$ is only 0.1 G and much smaller than the magnitudes of P_1 and P_3 (0.13 and −0.14 G, respectively, Table 4.5), indicative of a negligible nuclear quadrupole effect in the region of ~**B**//**z**. This is consistent with the experimental results and the single-crystal spectrum simulation at **B**//**z**", where the simulated spectra with a zero and non-zero **P** are not distinguishable (see below). Also, the similarity in the Ca2-$O3^F$ and Ca2-O2 bond distances (i.e., 2.349 and 2.374 Å, respectively; Hughes et al. 1989) is consistent with the result that the principal value P_1 is close to the value P_3 (Table 5). The longer Ca2-$O3^A$ bond (i.e., 2.501 Å; Hughes et al. 1989) accounts for the dramatic decrease in the nuclear quadrupole effect in this direction (i.e., the very small value of P_2; Table 4.5). The nuclear quadrupole gradient suggests that the shape of the electron distribution of the Gd^{3+} nuclide is an approximate ellipsoid of rotation.

The RMSDs when fitting $\mathbf{g}_n$ with and without an isotropic restriction are indistinguishable. The latter fitting reaches a g_n value of –0.2143 (Table 4.2), which is bigger than that of a free Gd^{3+} ion (–0.2253; Weil et al. 1994). A fitting of **A** and **P** with the g_n value of the free Gd^{3+} ion resulted in a slight increase in RMSD (Table 4.2), confirming the validity of the determined value of g_n. Therefore, we only detected isotropic chemical shift of g_n (e.g., Abragam & Bleaney 1970; Baker and Bleaney 1958; Blumberg et al., 1963; Halford et al. 1958; Weil and Anderson 1961) relative to that for the free Gd^{3+} ion (Weil et al. 1994), whereas $\mathbf{g}_n$ anisotropy was not observed.

TABLE 4.2. Optimization of the spin-hamiltonian parameters for matrices **A**, **P** and g_n

No.	Best fit	Restriction on parameter optimization *	RMSD (G)
(1)	**A, P** and g_n	None	0.1203
(2)	**A, P** and g_n	$g_n = g_n\mathbf{U}$	0.1234
(3)	**A** and **P**	$g_n = g_n\mathbf{U}$, $g_n = -0.2253$ (free $^{157}Gd^{3+}$ ion)	0.1240
(4)	**A** and **P**	$g_n = g_n\mathbf{U}$, $g_n = -0.2143$	0.1234
(5)	**A**	$\mathbf{A} = A\mathbf{U}$, $g_n = g_n\mathbf{U}$, $g_n = -0.2143$, **P** as obtained from (4)	0.7310
(6)	**A**	$g_n = g_n\mathbf{U}$, $g_n = -0.2143$, zero **P**	0.1604

* **U** = 3×3 unit matrix

TABLE 4.3 Simulated line positions and relative intensities for the 16 transitions contributing to the single-crystal spectrum observed with **B//z**, and $\mathbf{B}_1$//**x'** at T = 295.0 K and the experimental frequency 9.25303(1) GHz.

No.	Transitions	Line positions (G)	Relative intensities
1	13↔17	3322.18	0.00004
2	13↔18	3319.36	0.00727
3	13↔19	3316.49	0.02161
4	13↔20	3313.60	0.92811
5	14↔17	3325.43	0.00754
6	14↔18	3322.60	0.02956
7	14↔19	3319.73	3.89947
8	14↔20	3316.84	0.02048
9	15↔17	3328.71	0.02340
10	15↔18	3325.89	3.89749
11	15↔19	3323.02	0.02778
12	15↔20	3320.13	0.00839
13	16↔17	3332.03	3.92613
14	16↔18	3329.21	0.02275
15	16↔19	3326.35	0.00818
16	16↔20	3323.45	0.00004

TABLE 4.4 Ideal and calibrated directions of the rotation-plane normals and the crystal reference systems in the X-band EPR experiments.

Plane	x (or x")		y (or y")		z (or z")	
	θ (°)	ϕ(°)	θ(°)	ϕ(°)	θ(°)	ϕ(°)
xy	90.00^{A}	0.00^{A}			0.00^{N}	0.00^{N}
x"y"	90.00^{A}	0.00^{A}			0.00^{N}	0.00^{N}
yz	90.00^{N}	180.00^{N}			0.00^{A}	0.00^{A}
x"y"	88.81^{N}	182.12^{N}			2.02^{A}	264.02^{A}
xz			90.00^{N}	90.00^{N}	0.00^{A}	0.00^{A}
x"y"			90.81^{N}	95.44^{N}	0.81^{A}	95.44^{A}

^{A} Axis direction;
^{N} Normal directions of the rotation planes

TABLE 4.5 The principal values and directions of the matrices **A**, **P** and $\mathbf{g}_n$ for the Gd^{3+} centre 'a'

Y	Matrices			k	Principal values Y_k	Principal directions θ_k (°)	φ_k (°)
	4.18(4)	–2.55(6)	–0.60(5)	1	6.72(0)	51.0(9)	142.8(4)
$\mathbf{A}/g_e\beta_e$ (G)		3.21(5)	0.11(3)	2	5.63(0)	39.2(9)	315.8(7)
			6.05(2)	3	1.09(0)	86.6(5)	50.0(2)
	–0.11(2)	–0.07(1)	0.03(2)	1	0.13(0)	94(8)	287(3)
$\mathbf{P}/g_e\beta_e$ (G)		0.11(1)	0.02(2)	2	0.01(0)	165(9)	18(2)×10
			0.00(1)	3	–0.14(0)	104(8)	18(3)
	–0.214(8)	0.000(0)	0.000(0)				
$\mathbf{g}_n$		–0.214(8)	0.000(0)				
			–0.214(8)				

The estimated errors are given in parentheses.

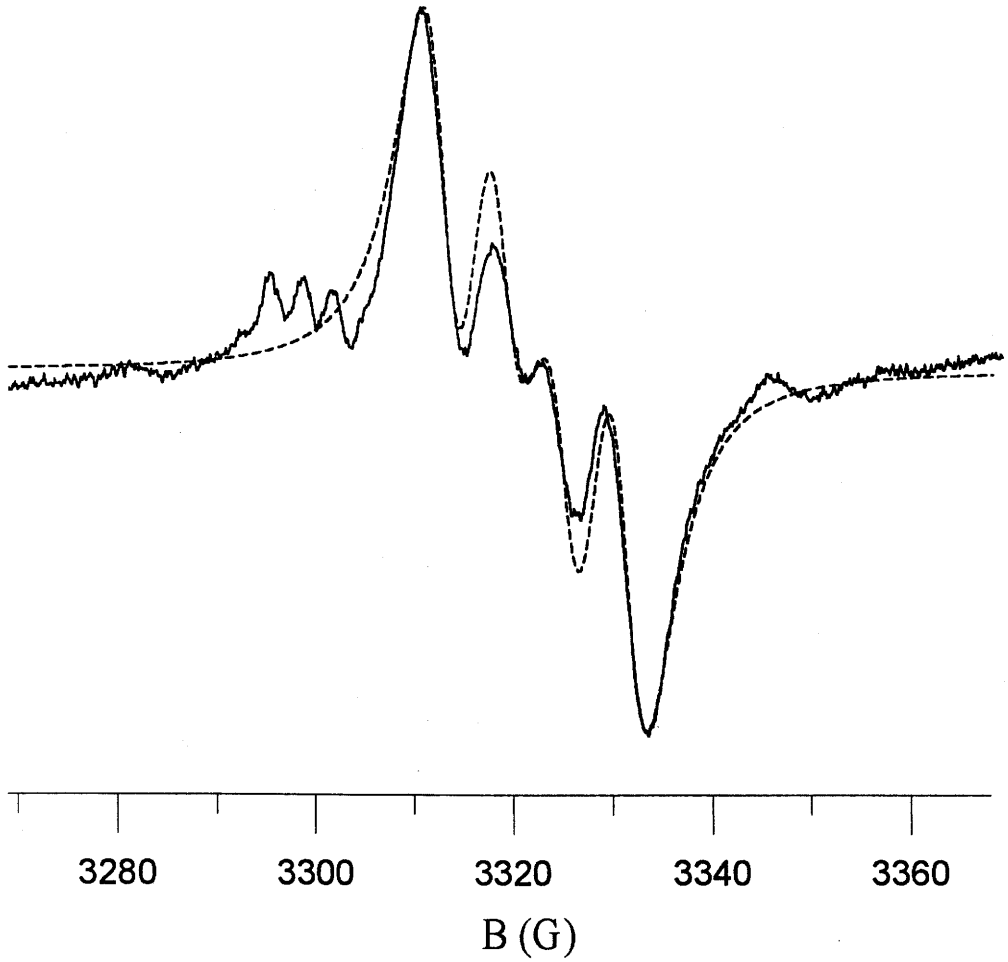

Figure 4.5. Observed and simulated X-band HFS for centre 'a' with $\mathbf{B}//\mathbf{z}$" and $\mathbf{B}_1//\mathbf{x}$" at 9.25303 (1) GHz and 295 K.

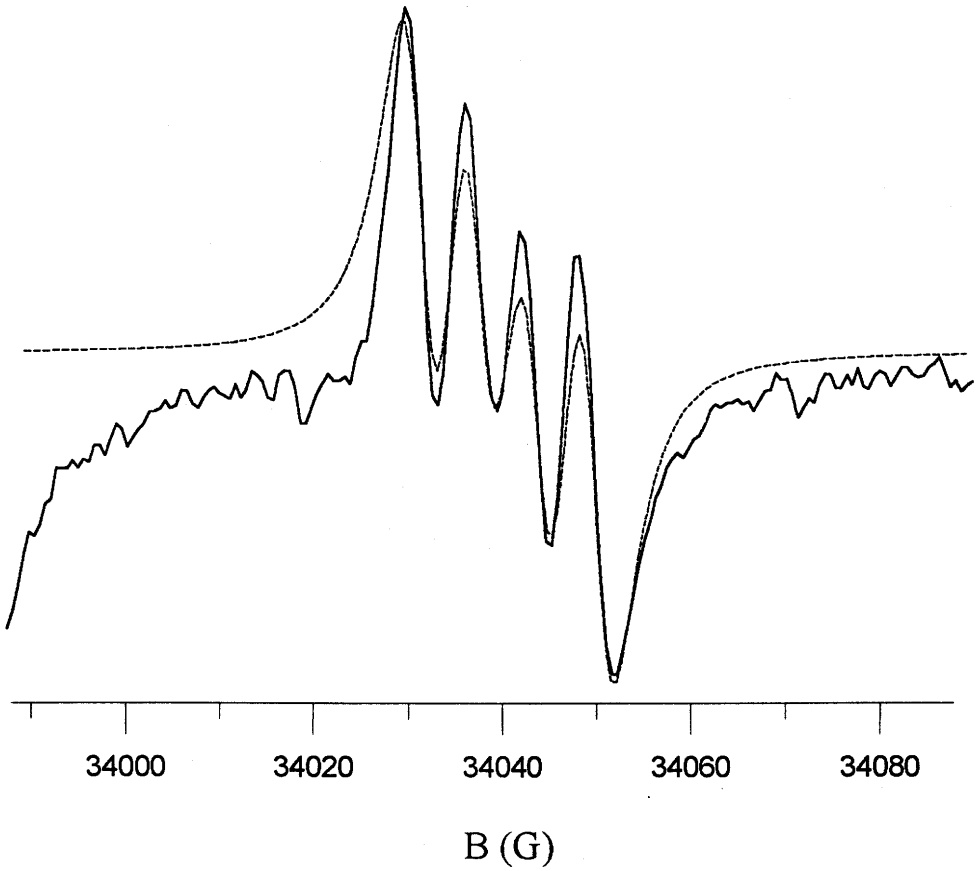

Figure 4.6. Observed and simulated W-band HFS for centre 'a' with **B**//**z**" and $\mathbf{B}_1$//**x**" at 94.4309 GHz and ~296 K.

4.3.3 X-band spectrum simulation

The X-band single-crystal hyperfine spectra of centre 'a' have been simulated by using the calculated matrices **A, P** and $\mathbf{g}_n$ as well as the even-isotope spin-hamiltonian parameters from Chen et al. (2001a). At **B//z"**, rotation group C_1 was utilized in the simulation, because of the full degeneracy for the six symmetry-related Ca2 sites (Chen et al. 2001a). At **B//x"**, rotation group C_2 was adopted to match the observed site splitting (Fig. 1b; see also Chen et al. 2001a). The lineshape of the individual HFS component lines has been shown to be lorentzian, similar to those of the lines observed from the even isotopes (Chen et al. 2001a,b).

Figure 4.5 shows that the simulated and observed spectra at **B//z'** are in excellent agreement. This confirms that not only the line positions but also the relative intensities are quantitatively available from the spin-hamiltonian obtained. Moreover, the estimated concentration factors in the spectrum simulations are 93.6 and 5.6 for the ^{157}Gd and ^{even}Gd nuclides, respectively, in excellent agreement with the known abundances of these isotopes given by the manufacturer (i.e., 93.62 and 5.785 %). Note that the sum of the two weighing factors is 99.2, owing to the fact that $^{155}Gd^{3+}$ was not included in the simulation. This result demonstrates once again that EPR is potentially accurate in estimating the relative isotopic abundances of paramagnetic trace elements in solids.

4.3.4 W-band spectrum simulation

A similar simulation has been made for the W-band HFS spectrum at **B//z'**. This simulation shows that the spin-hamiltonian parameters determined from the X-band spectra gives an excellent prediction of the HFS observed in the W-band experiments

(Fig. 4.6). Also, simulations show that, without the inclusion of the even-isotope Gd^{3+}, the X- and W-band spectra can both be simulated well in hyperfine splitting, lineshape, linewidth, as well as the intensity, although an inclusion of the even isotopes does improve the quality of the simulation, especially for the relative intensity of the two inner lines.

The estimated concentration factors in the W-band spectrum simulation were found to be 93.6 and 4.0 for ^{157}Gd and ^{even}Gd, respectively. They too are in good agreement with the known abundances given by the manufacturer, albeit somewhat poorer than those obtained from the X-band spectrum simulation. A possible explanation for the poorer result in the W-band experiments is peak interference from other paramagnetic species such as $^{55}Mn^{2+}$, which have been clearly detected at this frequency but were not observed in the X-band experiments.

The linewidth of the individual component lines of the HFS in the W-band spectra is 4.5 G, smaller than that (4.9 G) in the X-band EPR. This result is consistent with the second-order perturbation theory (Weil et al. 1994, p.189). From the energy equation of the second-order perturbation theory, a line-position equation was developed, by which the linewidth expression was then developed. The latter predicts that the linewidth of a given transition is inversely proportional to the experimental frequency (i.e., under similar spectral resolutions, as in this study; cf. Chen et al. 2001b).

4.3.5 Hyperfine anisotropy

A series of single-crystal X-band spectrum simulations (Figs. 4.7, 4.8 and 4.9) was made for the transitions between m_S values $+1/2 \leftrightarrow -1/2$ to evaluate the

contributions of the various terms of the spin-hamiltonian to the hyperfine anisotropy (i.e., the splittings and transition probabilities of the hyperfine-component line positions), in addition to those caused by the matrices **A**, **P** and $\mathbf{g}_n$. All simulations assumed isotropic **A** (A = 4.4 G) and isotropic $\mathbf{g}_n$ ($g_n = -0.2143$) as well as zero **P**, while the other spin-hamiltonian terms, except those under evaluation, were kept as those in Chen et al. (2001a). These simulations were performed with **B** in the y"z" plane where magnetic site splitting was not detected (Chen et al. 2001a). The angular simulation region chosen is from **B**//**z**" ($\theta" = 0°$, $\varphi" = 90°$) to **B**//**y**" (90°, 90°).

4.3.5.1 Line-position and total-splitting anisotropy

Figure 4.7a shows that the non-nuclear terms (Chen et al. 2001a) result in a "quadratic" shape of the line-position roadmap for the HFS-component lines. The same shape also exists for the total splitting (TSHFS; Fig. 4.8a and Table 4.3) of the HFS. Here, TSHFS was defined as the field interval between the peaks related to the transitions 13 ↔ 20 and 16 ↔ 17 (Fig. 4.3). Our simulations show that there is no line position crossing for different transitions when the field **B** is rotated in plane y"z" (Fig. 4.7a). Also, the HFS spectrum is nearly superposed to 2-, 3- and 4-fold at most of the **B** orientations, except slightly lifting observed at some directions (Fig. 4.7a), also indicating that the TSHFS is also angular dependent.

Simulation shows that the residual anisotropy is very small under the restriction of a zero **D** (Figs 4.7a and 4.7b), indicating its major role for the anisotropy transferring from the non-nuclear spin-hamiltonian terms to the anisotropy of the angular dependence of the line-position roadmap HPS. Similarly, the angular dependence of the

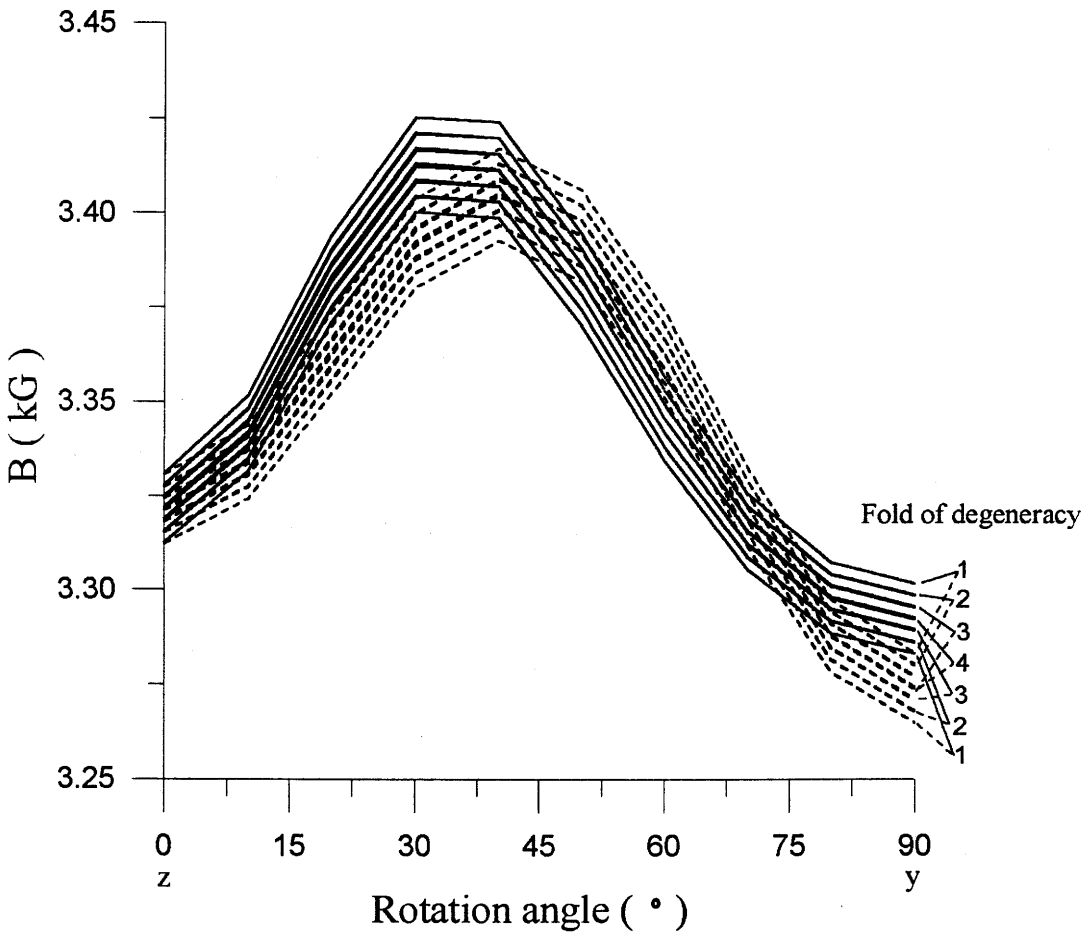

Figure 4.7a. The roadmap of the HFS simulated at the average experimental frequency of 9.250 GHz in the plane yz. The solid curves indicate the roadmap simulatd with isotropic A and zero $I^2(\mathbf{P})$. The other spin-hamiltonian terms $BS(\mathbf{g})$, $S^2(\mathbf{D})$, S^4, S^6, BS^3 and BS^5 are same as those estimated for the even-isotope Gd^{3+} centre 'a'. The dashed curves indicate the roadmap simulated with zero S^4 terms. The other terms are the same as those used in the first simulation. Note that the partial degeneracies of the HFS are indicated.

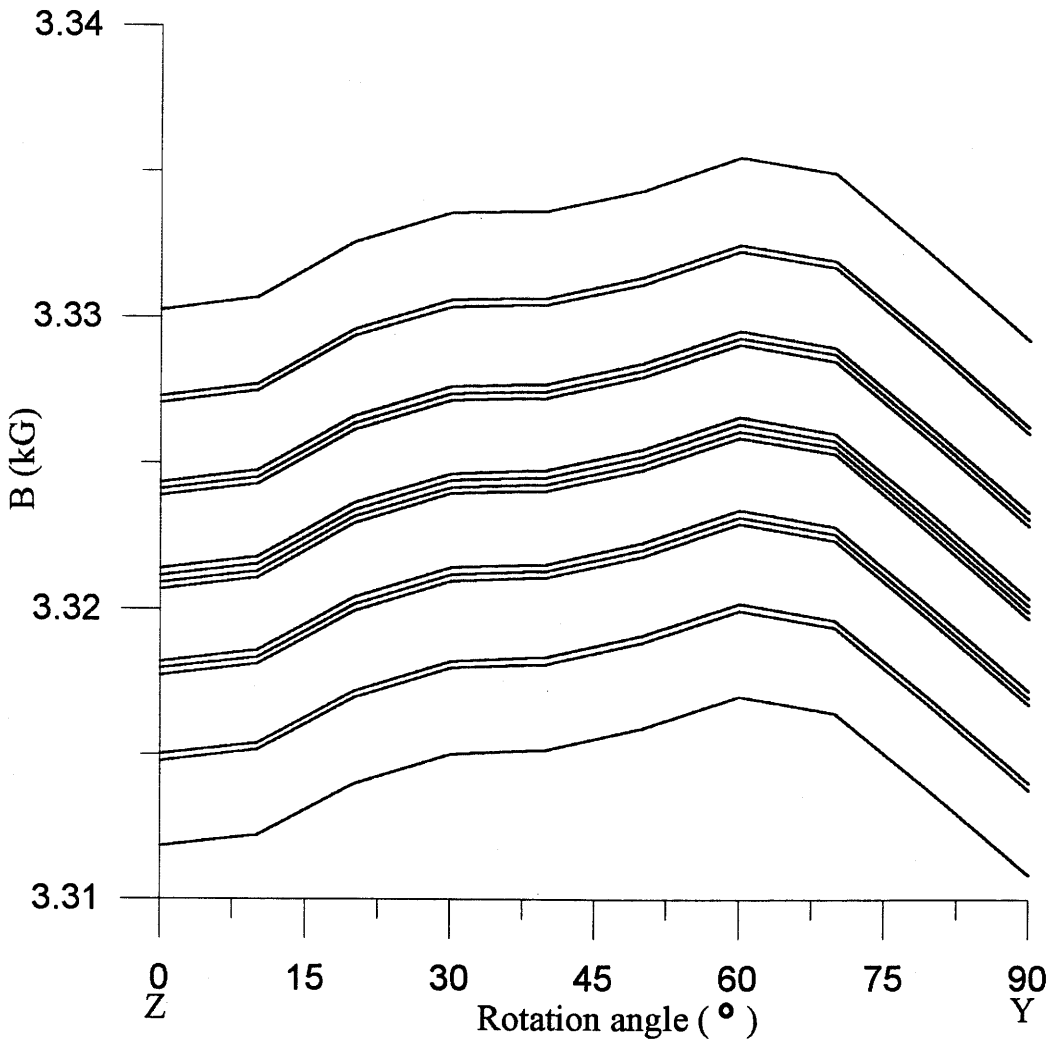

Figure 4.7b. The roadmap of the HFS simulated with a zero **D** at the average experimental frequency of 9.250 GHz in the yz plane. Other spin-hamiltonian terms as the simulation shown by the solid lines in Fig. 4.7a. Note that the partial degeneracy of the HFS has been lifted.

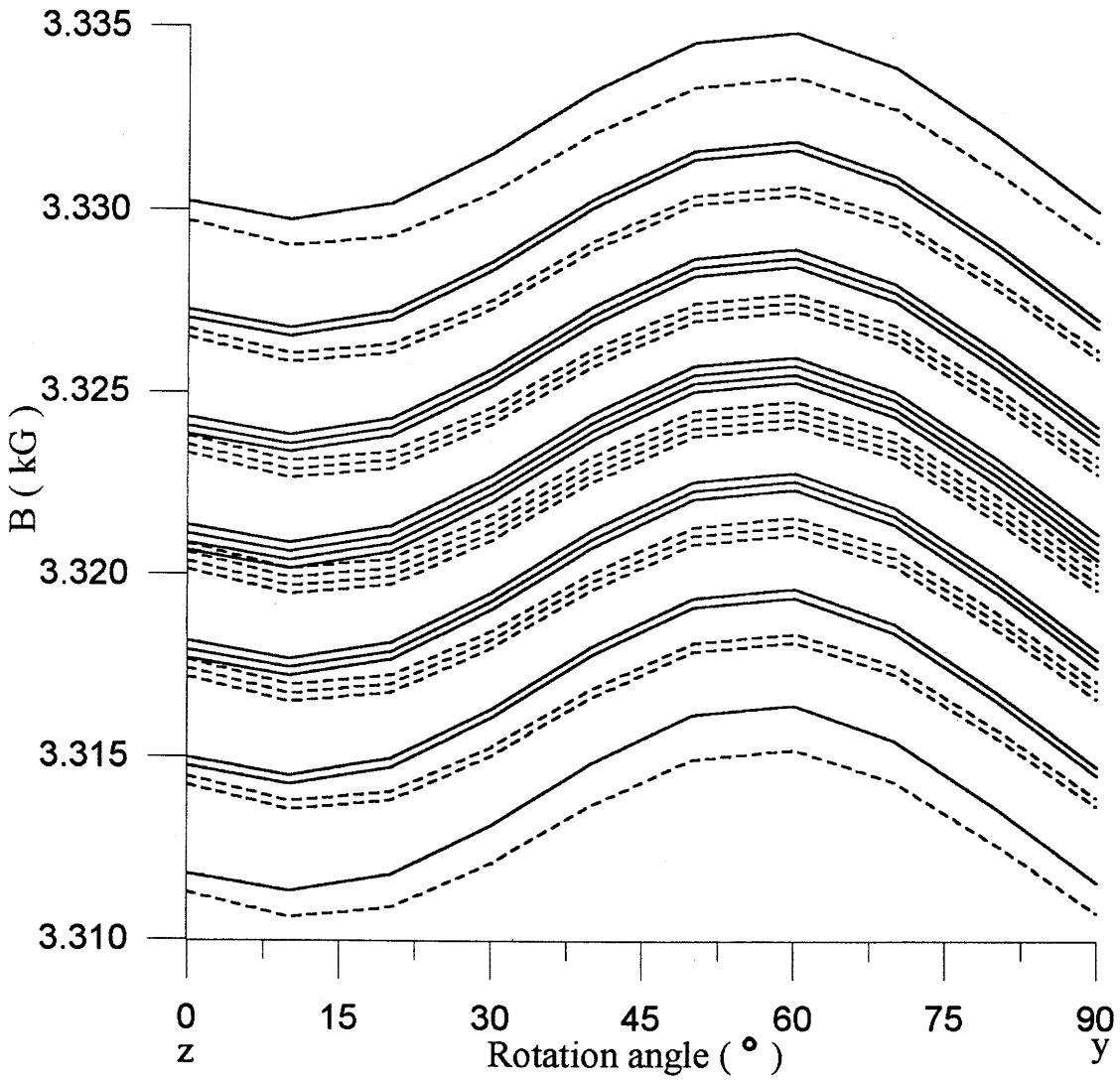

Figure 4.7c. The roadmap of the HFS simulated at the average experimental frequency of 9.250 GHz in the yz plane. The solid lines indicate two simulations, i.e., both with isotropic A and zero S^2(**D**), I^2(**P**) and S^4 terms, but the second one including zero S^6 terms. Other spin-hamiltonian terms are the same as those used before. Note that no observable difffrence exists between the two simulations. The dashed lines indicate a simulation with isotropic g and A plus zero terms of **D**, S^4 and S^6. The parameters of BS^3 and BS^5 are the same as before.

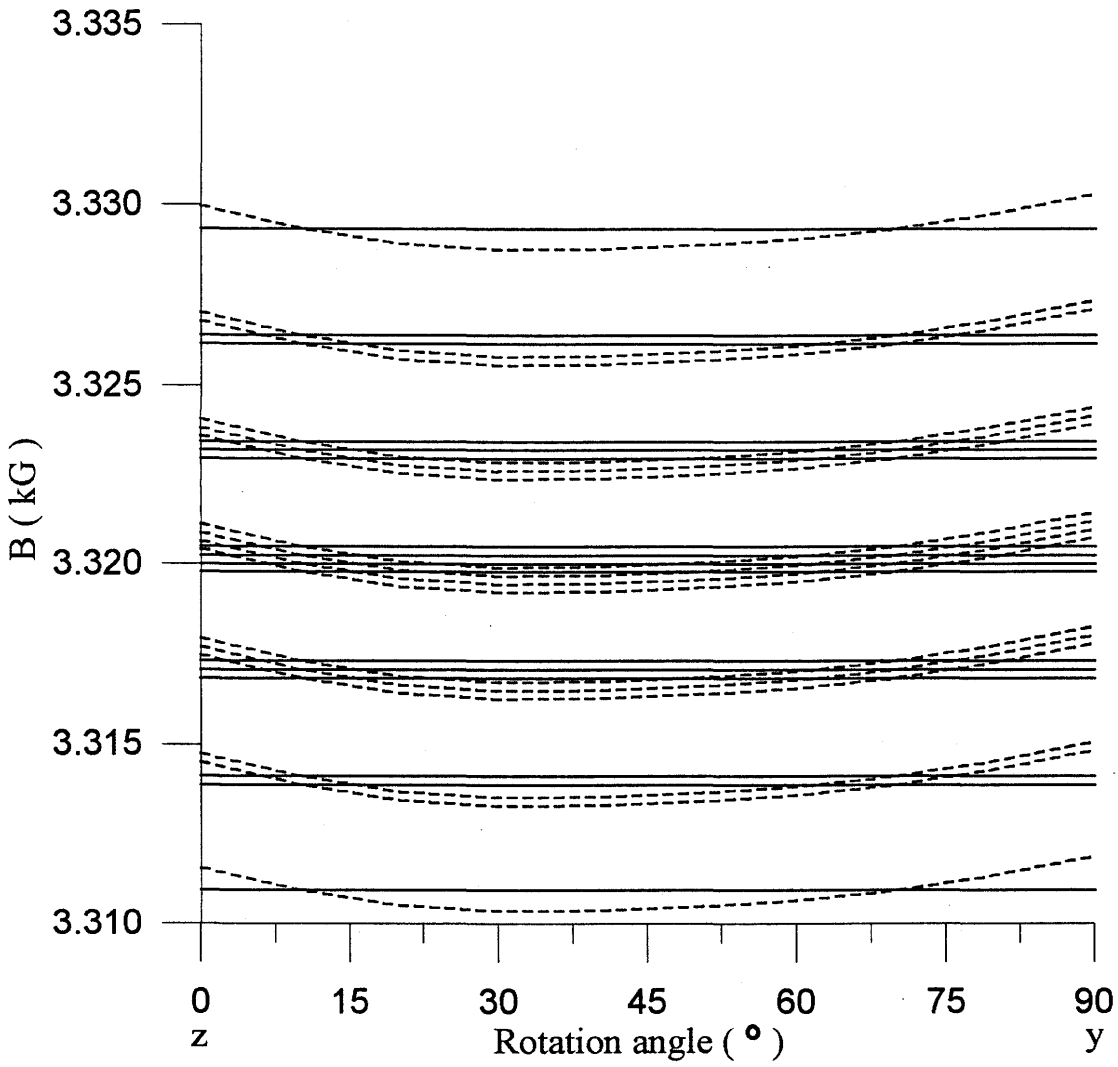

Figure 4.7d. The roadmap of the HFS simulated at the average experimental frequency of 9.250 GHz in the yz plane. The solid lines indicate the simulations with isotropic g and A, zero $S^2(\mathbf{D})$, $I^2(\mathbf{P})$, and zero parameters for terms S^4, S^6, BS^3 and BS^5. The dashed lines indicate that the simulations are the same as those shown by solid lines except with non-zero parameters of the BS^5 terms.

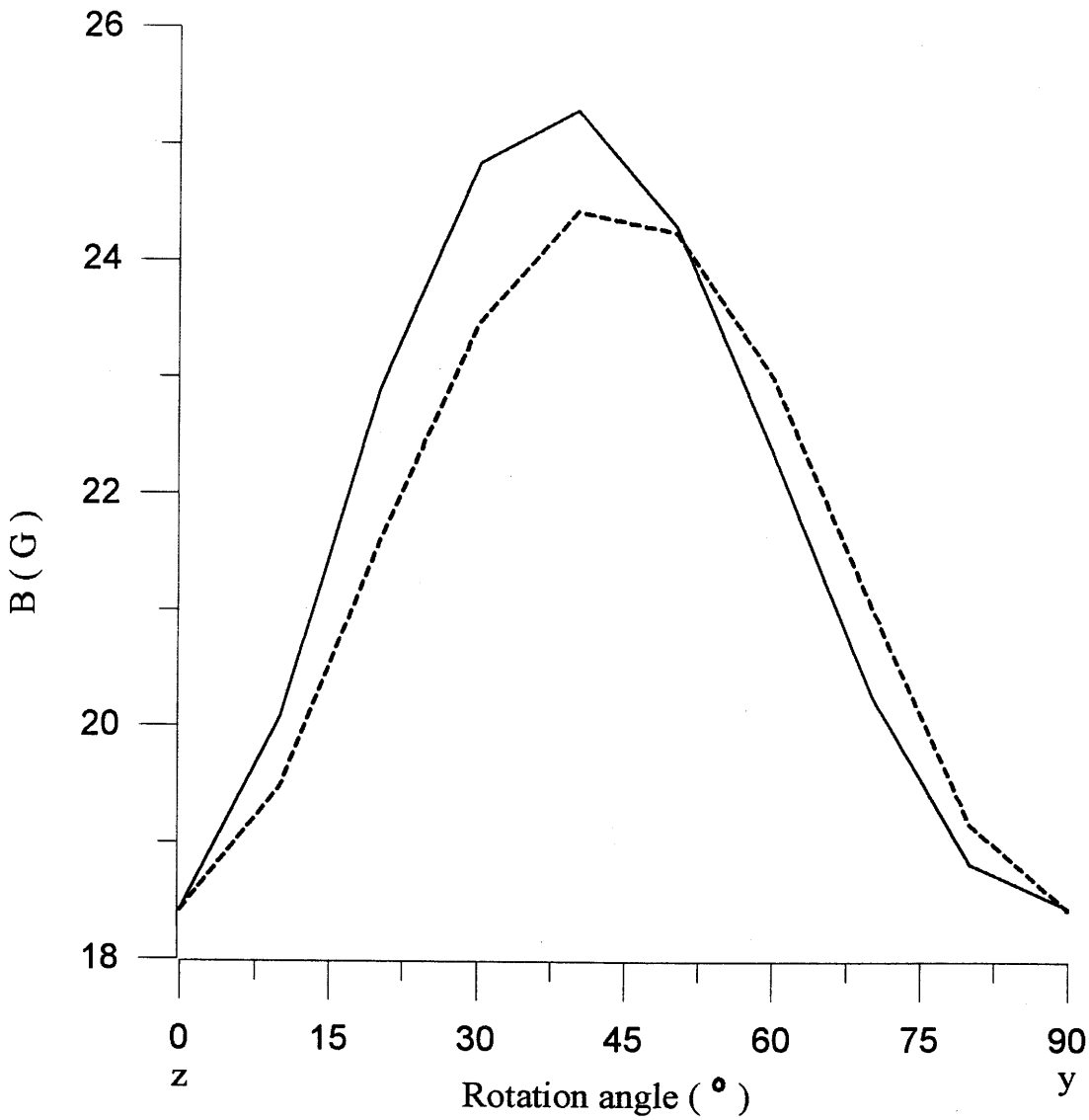

Figure 4.8a. The TSHS of the HFS simulated at the average experimental frequency of 9.250 GHz with **B** in the yz plane. The solid lines indicate the TSHS simulated with an isotropic A and a zero $I^2(\mathbf{P})$. Other terms of type BS(**g**), $S^2(\mathbf{D})$, S^4, S^6, BS^3 and BS^5 are the same as those estimated for the even-isotope Gd^{3+} nuclide occupying the Ca2[1] site. The dashed lines indicate the TSHS simulated with zero S^4 terms; the other terms are the same as those used in the first simulation.

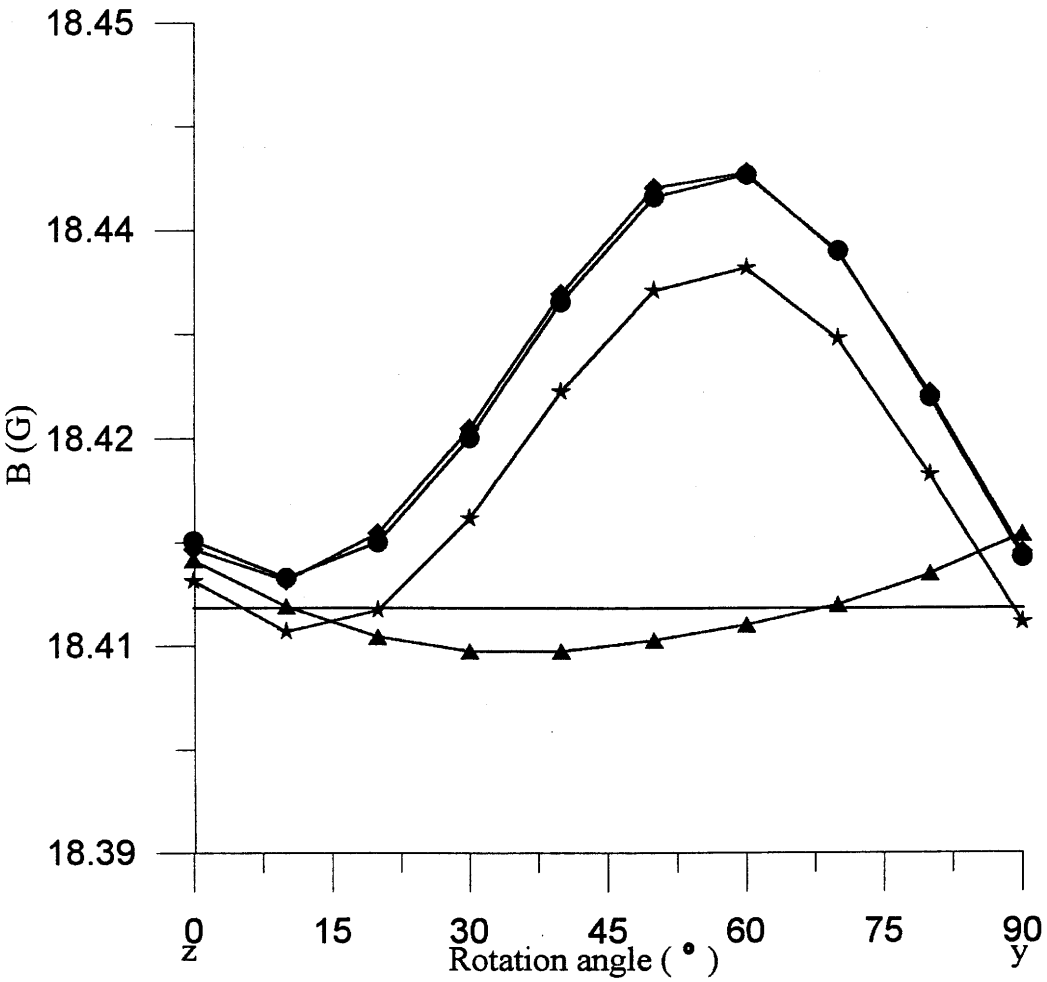

Figure 4.8b. The TSHS of the HFS simulated at the average experimental frequency of 9.250 GHz with **B** in the yz plane. The solid line indicates the TSHS simulated with isotropic matrice g and A, zero terms of type S^2(**D**), I^2(**P**), S^4, S^6, BS^3 and BS^5. The curves with triangles indicates the TSHS with all terms similar to the first case except with a BS^5 terms are the same as before. The curves with stars indicates TSHS with isotropic g and A, zero S^2, I^2, S^4 and S^6. The terms BS^3 and BS^5 were as same as before. The line with circles indicates the TSHS with isotropic A, zero S^2, I^2, S^4 and S^6. The other terms were as same as before. The diamond line indicates the TSHS with isotropic A, zero S^2, I^2, and S^4. The other terms were as same as before.

TSHFS almost disappears, with a variation less than 0.3 G (Fig. 4.8b), which is considerably smaller than that from simulations with **D** (6.5 G; Fig. 4.8a). These results show that the anisotropy of **D** is not only transferred but contributes greatly to the line-position and TSHFS anisotropy of the HFS. Moreover, the D transferring was found not only to be different for different transitions, but also to be anisotropic for an individual transition. However, some residual anisotropy cannot be attributed to the D transferring. For example, a concave shape exists for the line-position roadmap, with a concavity of ~18 G (Fig. 4.7b).

The effects of the term of type S^4 on the angular dependence of the line-position roadmap and the TSHFS are also visible (Figs. 4.7a and 4.8a). However, S^4 cannot be responsible for the degeneracy of the HFS, which is not lifted after the removal of this term (Fig. 4.7a).

Figure 4.7c shows that the shape of the line-position roadmap changes from "quadratic" to "sinusoidal" after the removal of both the S^2 (**D**) and S^4 terms. Similarly, residual anisotropy is present in the angular dependence of the TSHFS (Fig. 4.8b). Figure 4.7c shows that the term of type S^6 contributes little to the line-position roadmap, although a small variation was found for the angular dependence of the TSHFS, with magnitude of about 5.0×10^{-4} G, (Fig. 4.8b). Therefore, transferring from the anisotropy of S^6 to anisotropy of the HFS exists but is rather limited.

Figures 4.7c and 4.8b also show that the term of type BS (**g**) contributes little to the shape of the line-position roadmap and angular dependence of the TSHFS. However, the isotropic restriction on **g** does cause systematic shifts of the line-position roadmap and the TSHFS, with values of about 0.5×10^{-3} and 2.5×10^{-3} G, respectively,

indicating that the transferring from the anisotropy of **g** to the HFS is angular independent.

Figures 4.7d and 4.8b show that the term of type BS^3 is responsible for the "sinusoidal" shapes of the line-position roadmap HFS and the TSHFS, and that the term of type BS^5 can account for the small concavities (i.e., ~6.25×10^{-4} G), because all angular anisotropy of the HFS was eliminated (i.e., linear line-position roadmap and TSHFS) after inclusion of BS^5.

4.3.5.2 Transition-probability anisotropy

Figure 4.9a shows the effects of the non-nuclear spin-hamiltonian terms (e.g., BS (**g**), S^2 (**D**), S^4, S^6, BS^3 and BS^5) on the transition-probability anisotropy of the HFS. When **B** is parallel to the crystallographic axes [i.e., axes **c** ($\theta = 0°$) or **b** ($\theta = 90°$, $\varphi' = 90°$)], the four "allowed" transitions (i.e., transitions 4, 7, 10 and 13; Table 4.3) have almost equal relative intensities and dominate the HFS, while the contributions from the "forbidden" transitions are negligible. With **B** inside the angular region near the bisector of the axes **c** and **b**, the relative intensities of the "allowed" transitions decrease dramatically relative to those of the "forbidden" ones, and become even weaker than those of the latter at some directions. This simulation shows that the angular anisotropy in relative intensities for the HFS of the centre 'a' not only arises from **A, P** and $\mathbf{g}_n$ but is affected by other spin-hamiltonian terms and that the anisotropy contributions from the latter can be very strong.

Figure 4.9b shows that the simulated probabilities with a zero S^2 (**D**) differ from those of the simulation demonstrated in Figure. 4.9a. Here, the "allowed" transitions

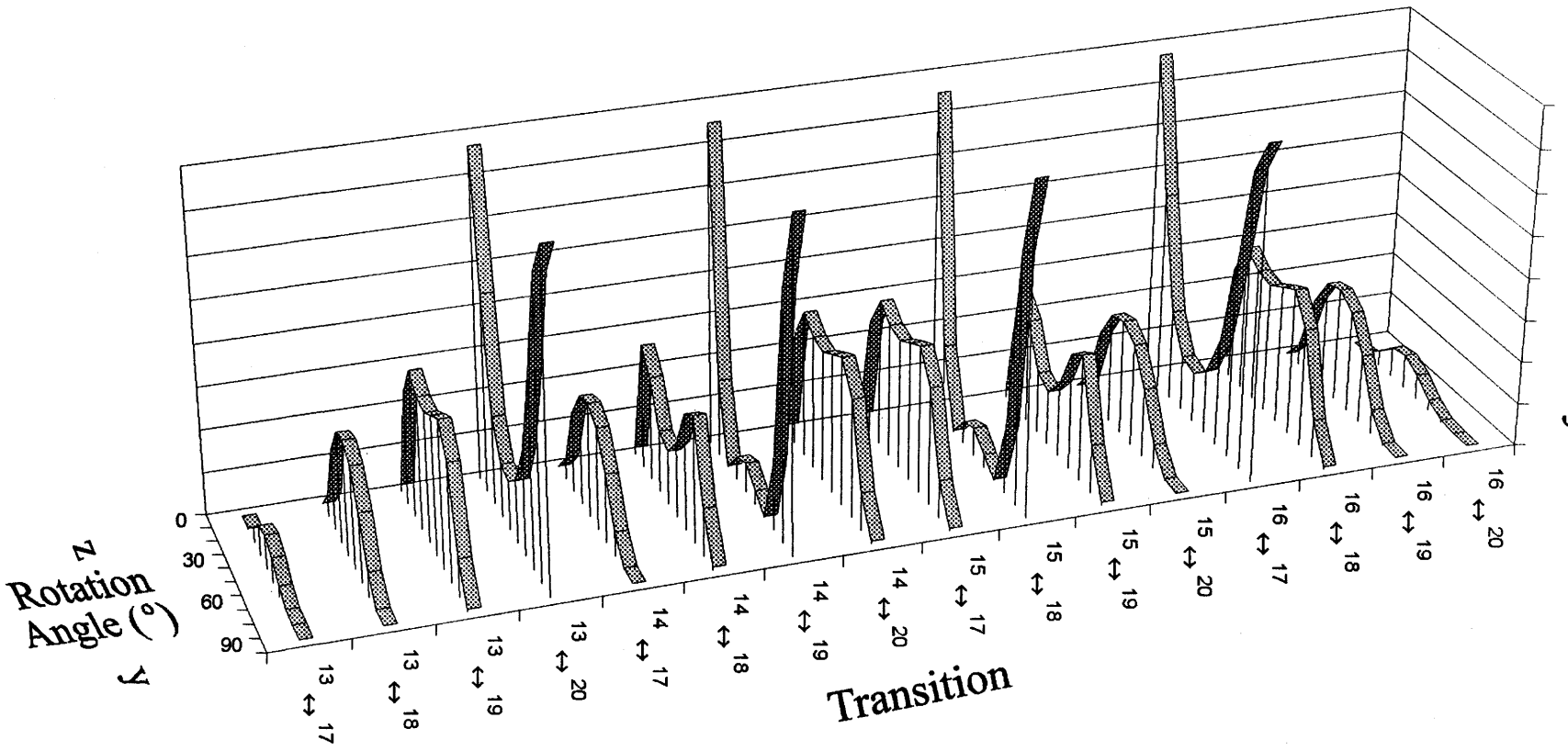

Figure 4.9a. The simulation of the probabilities for the transitions contributing to the observed HFS at the average experimenta frequency of 9.250 GHz in the yz plane with matrices of isotropic A and zero I^2(**P**). The other spin-hamiltonian terms of BS (**g**) S^2(**D**), S^4, S^6, BS^3 and BS^5 are the same as those terms estimated for the even isotopes Gd^{3+} ion cocupying the $Ca2^1$ site. Note tha $\theta = 0$ and 90 correspond to **B//z** and **B//y**, respectively.

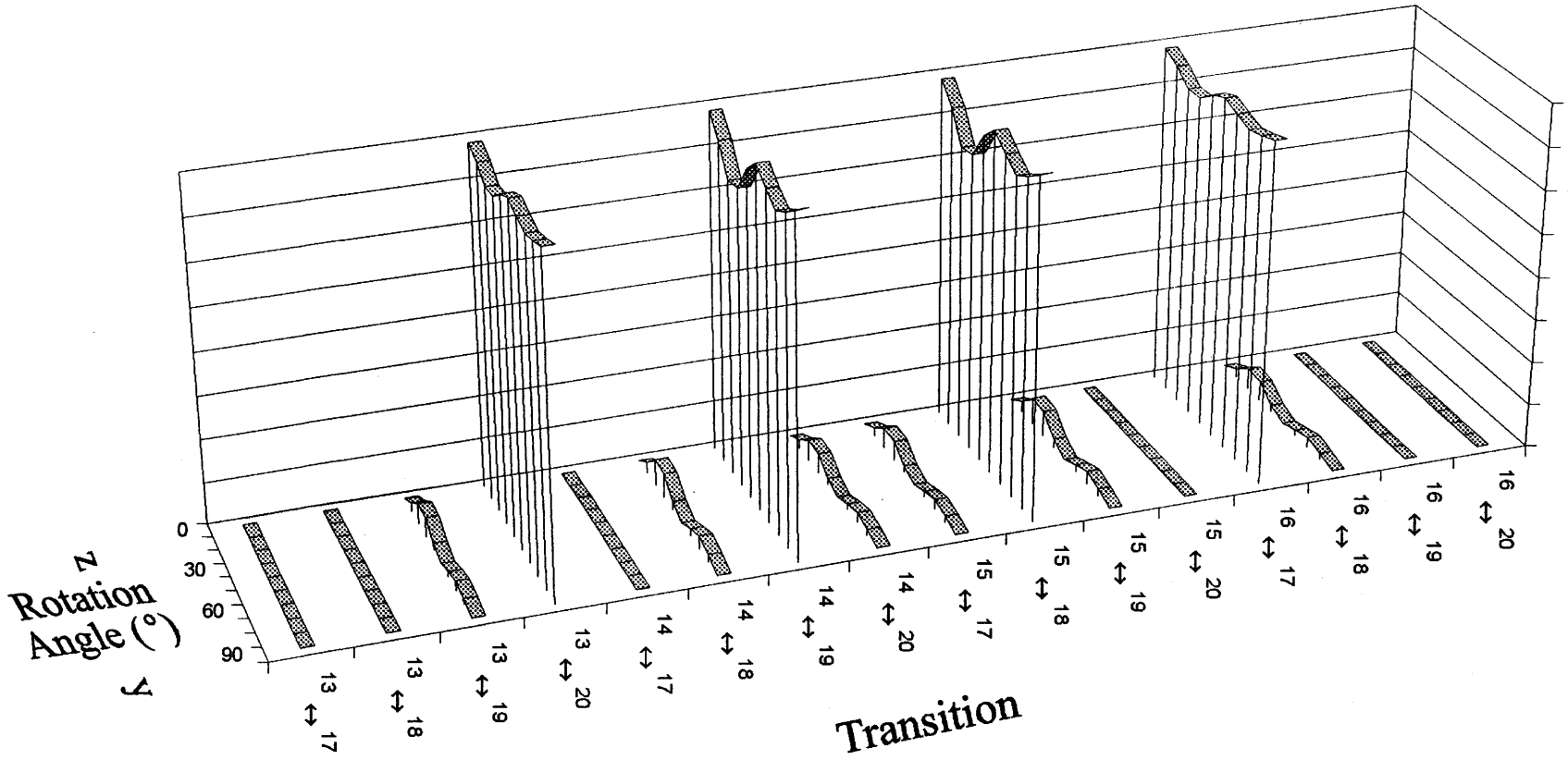

Figure 4.9b. The simulation of the probabilities for the transitions contributing to the observed HFS at the average experimental frequency of 9.250 GHz in the yz plane with a zero **D**. The other spin-hamiltonian terms are the same as those used in the simulation shown in Fig. 4.9a. Note that $\theta = 0$ and 90° correspond to **B//z** and **B//y**, respectively.

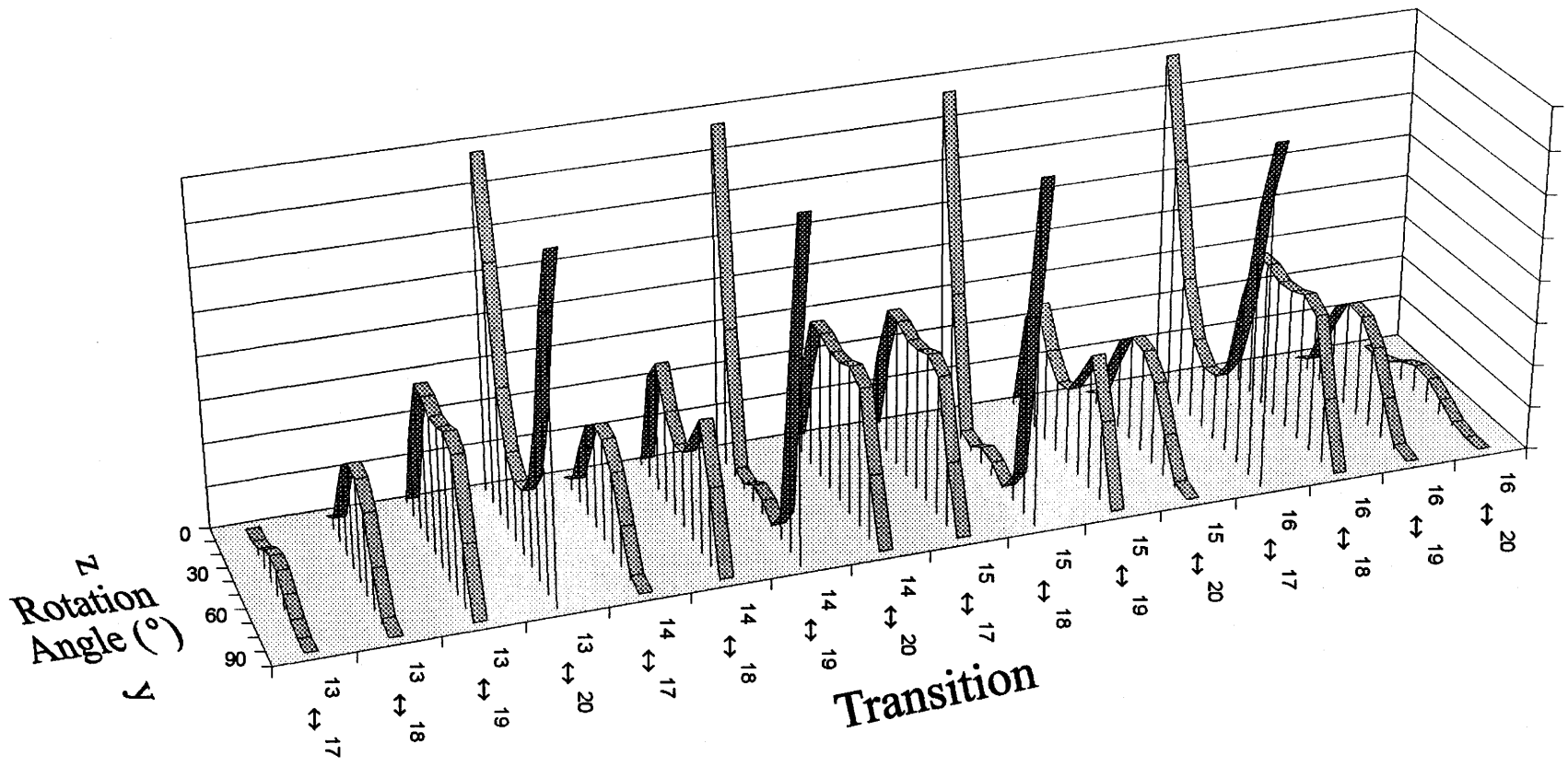

Figure 4.9c. The simulation of the probabilities for the transitions contributing to the observed HFS at the average experimental frequency of 9.250 GHz in the yz plane with a zero S^4. The other spin-hamiltonian terms are the same as those used in the simulation shown in Fig. 4.9a. Note that $\theta = 0$ and 90° correspond to **B//z** and **B//y**, respectively.

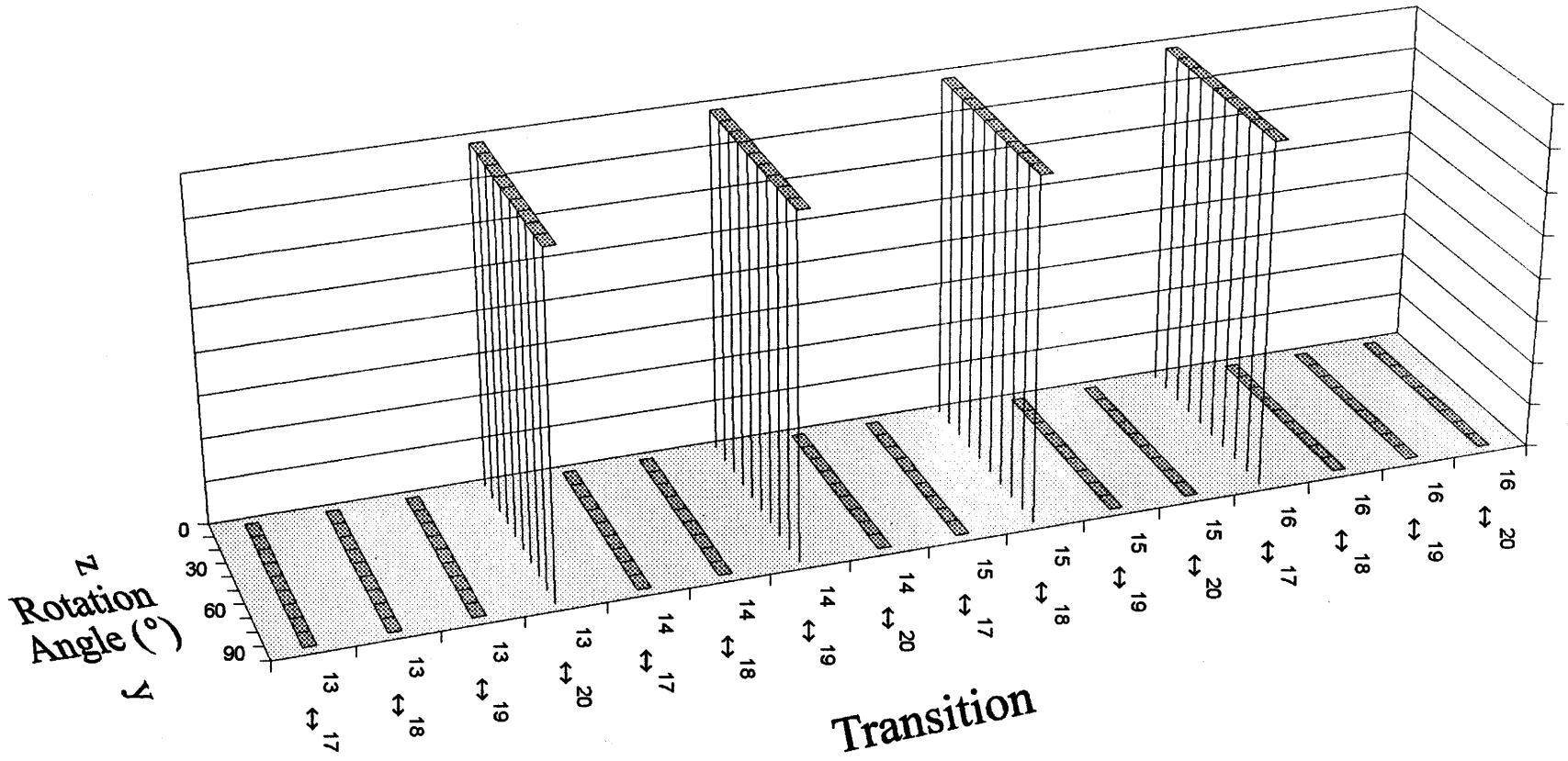

Figure 4.9d. The simulation of the probabilities for the transitions contributing to the observed HFS at the average experimental frequency of 9.250 GHz in the yz plane with a zero $S^2(D)$ and S^4 term. The other spin-hamiltonian terms are the same as those used in the simulation shown in Fig. 4.9a. Note that $\theta = 0$ and 90° correspond to **B//z** and **B//y**, respectively.

always dominate the HFS and result in a well-resolved four-line structure in all directions. The contributions from the "forbidden" transitions are much weaker and are only apparent at the angular regions where the probabilities of the "allowed" transitions are reduced.

Another question is whether the transferring of anisotropy is from the rhombic feature of **D**. A simulation was made for a uniaxial **D** matrix with diagonal $D'_1 = D'_2 = (D_1 + D_2)/2$ and $D'_3 = -(D_1+D_2)$ (where D_1 and D_2 are the principal values of **D**, Chen et al. 2001a). This simulation yielded similar results to those for the rhombic **D** (Fig. 4.9a), indicating that transferring of anisotropy from **D** to the HFS exists even for a uniaxial **D** and herein dominates the transferring contribution from the non- **A, P** and $\mathbf{g}_n$ terms.

Figure 4.9c shows that the effect of S^4 on the transition probability anisotropy is also observable, but that the relative intensities are similar to those determined for the simulation with a non-zero S^4 (Fig. 4.9a).

Figure 4.9d shows the simultaneous effects of S^2 (**D**) and S^4 on the transition-probability anisotropy of the HFS. The angular dependence of the probabilities for the "allowed" transitions has almost completely disappeared, with an average variation in probability of only $1.55(4)\times10^{-2}$, while the "forbidden" transitions give an average variation in probability of $4(5)\times10^{-4}$. These data suggest that, without the transferring of the anisotropy from the terms S^2 (**D**) and S^4, the "allowed" transition probabilities are isotropic. The probabilities for those "forbidden" transitions may still not be isotropic, considering the high uncertainty in the estimated average probability, but are relatively unimportant in their contribution to the HFS spectrum.

4.4 Conclusions

The anisotropy of the HFS of the $^{157}Gd^{3+}$ nuclide occupying the Ca2 site is caused by the spin-hamiltonian terms of **A**, as well as by other types of terms, including BS (**g**), S^2 (**D**), S^4, S^6, BS^3 and BS^5. The term S^2 dominates the contribution of anisotropy from these spin-hamiltonian terms. Its anisotropy is transferred to the HFS, resulting in strong anisotropic roadmaps of line positions of the HFS, TSHS and relative intensities. This effect also exists for a uniaxial **D**. Moreover, the D transferring was found not only to be different for different transitions, but also to be different for an individual transition. The anisotropy contribution from the term S^4 has a secondary importance relative to that from S^2 and is not negligible. The contribution from S^6 is small and negligible relative to that from S^4. The transfer from BS (**g**) to the HFS is present, but angular-independent. The sinusoidal shape of the residual anisotropy under the conditions of zero S^2, S^4; zero S^2, S^4 and S^6 or zero S^2, S^4 and S^6 plus isotropic BS is attributed to the transfer from BS^3. The nonlinearity in the shape of the roadmap of HFS and angular dependence of the TSHS is proved to come from the contribution of BS^5.

CHAPTER 5

Summary

The spin-hamiltonian parameters of two Gd^{3+} centres (the centres 'a' and 'b') in synthetic fluorapatite, including the matrices **g** and **D** and the high-spin terms of type S^4, S^6 as well as BS^3 and BS^5, have been determined by analyzing well-resolved single-crystal even-isotope X- and W-band EPR spectra in three orthogonal rotation planes.

The validity of the spin-hamiltonian parameters for the Gd^{3+} centre 'a', determined from single-crystal X-band EPR spectra, has been confirmed by agreement between the simulated and observed X-band spectra of both single crystals and powder samples (line shape and line positions), and other EPR data, such as energy levels, angular dependence of line positions (roadmaps), and EPR signal relative intensity. The validity of the spin-hamiltonian parameters for the Gd^{3+} centre 'a' has also been confirmed by the successful prediction of the W-band single-crystal spectrum for this centre. To the best of my knowledge, this is the first successful prediction of single-crystal W-band EPR spectra from spin-hamiltonian parameters determined from X-band EPR spectra.

The Gd^{3+} centre 'a' in the synthetic fluorapatite corresponds to a substitution of the Gd^{3+} ion into Ca2 sites with a rhombic local environment. The deviation of the matrix **D** from a unixial symmetry lies outside the estimated experimental error. The site assignment of the Gd^{3+} ion of the centre 'a' has been confirmed by matching the structural directions of the ideal Ca2 site in pure fluorapatite and the fitted experimental

parameter-matrix principal directions (**D** and **g**), and the calculated pseudo-symmetry directions (S^4 terms). The suggested substitution mechanism for this centre is $Ca^{2+} + F^- \Leftrightarrow Gd^{3+} + O^{2-}$.

The validity of the spin-hamiltonian parameters of the Gd^{3+} centre 'b', determined from W-band EPR spectra, has been confirmed by agreement between the simulated and observed single-crystal W-band spectrum (line shape and line positions) and other EPR data, such as energy levels, angular dependence of line positions (roadmaps), EPR signal relative intensity, and magnetic site splitting.

The Gd^{3+} centre 'b' in the synthetic fluorapatite corresponds to a substitution of the Gd^{3+} ions into Ca1 sites and also has a highly rhombic local environment. The site assignment of the centre 'b' has been confirmed by matching between the structural directions of the ideal Ca1 site and the calculated experimental parameter-matrix **D** principal directions and the estimated pseudo-symmetry directions of the S^4 term. The suggested substitution mechanism for this centre is $2Gd^{3+} + \square \Leftrightarrow 3Ca^{2+}$, having an arrangement of the type Gd^{3+} -- □ --- Gd^{3+} with the vacancy (□) at a nearest-neighbor to one Gd^{3+} occupied Ca2 site (i.e., $Ca2^6$ to $Ca1^1$, or $Ca2^k$ to $Ca1^{k+1}$, k = 1, 2 ...5), but the second one is not necessarily to be a nearest neighbor.

A combined X- and W-band EPR study of ^{157}Gd-doped fluorapatite crystals revealed a well-resolved $^{157}Gd^{3+}$ hyperfine structure of the centre 'a'. The spin terms of type SI (**A**), I^2 (**P**) and BI ($\mathbf{g}_n$) as well as the high-spin terms of type S^3I and SI^3, for this centre have been determined from the single-crystal X-band EPR spectra of the ^{157}Gd-doped fluorapatite. The validity of the HFS spin terms has been confirmed by the agreement between the simulated and observed single-crystal X-and W-band spectra in

line shape and line positions, energy levels and EPR signal relative intensity. This is the first successful determination of matrices **P** and $\mathbf{g}_n$ for Gd centres by single-crystal EPR.

The calculated spin terms for the hyperfine, nuclear quadrupole and Zeeman effects (i.e., matrices **A**, **P** and $\mathbf{g}_n$) provide further evidence for that the centre 'a' corresponds to Gd^{3+} ions at the Ca2 sites and has rhombic local symmetry. Also, the **P** matrix shows that the electron distribution of the Gd^{3+} nuclide at the centre 'a' is close to uniaxial, with the largest value along the direction of the Ca2-O2 bond and almost isotropic in the horizontal plane.

Single-crystal spectrum simulations have shown that the anisotropy of the HFS is caused by **A** as well as by other types of terms, including terms of the BS (**g**), S^2 (**D**), S^4, S^6, BS^3 and BS^5. The term S^2 has a dominant effect on the hyperfine anisotropy over all other non-**A** spin-hamiltonian terms. The transfer from the anisotropic S^2 results in a strong anisotropy of the relative intensities of the HFS lines, the line-position roadmap of the HFS and the total splitting of the hyperfine structure (TSHFS). This effect of anisotropy transfer also exists for a uniaxial matrix **D**. Moreover, the D transferring was found not only to be different for different transitions, but also to be anisotropic for an individual transition. The anisotropy contribution from the S^4 term has a secondary importance relative to that from the S^2 term and is not negligible. The contribution from the S^6 term is small and negligible relative to that from the S^4 term. Transferring from the BS term to the HFS is present, but angular-independent. The sinusoidal shape of the residual anisotropy under the conditions of zero S^2 and S^4 terms; or of zero S^2, S^4 and S^6 terms or of zero S^2, S^4 and S^6 terms (plus an isotropic BS term) is attributed to the transferring from the BS^3 term. The small nonlinearity in shape of the roadmap of the

HFS and angular dependence of the TSHS is shown to come from the contribution of the BS^5 term.

Finally, the present findings for the local structural environments and substitution mechanisms of the Gd^{3+} centre 'a' and 'b' in synthetic fluorapatite are useful to further understanding of the uptake of REEs in natural apatites, which in turn is of crucial importance for the applications of REEs to such geological and environmental problems as petrogenetic modeling of the sources and evolution of igneous rocks (e.g., Watson & Green, 1981), paleoenvironmental reconstruction (e.g., Holmden et al., 1998; Pan and Stauffer, 2000), and containment of various radioactive and hazardous wastes (e.g., U, ^{90}Y, ^{90}Sr, Pb and Cd; Wronkiewicz et al., 1996 and references therein). Moreover, this study has shown that the general spin-hamiltonian parameters obtained for the two Gd^{3+} centres can be used to successfully model the powder EPR spectra of Gd-doped fluorapatite. Therefore, these spectroscopic results may be extended to model Gd-doped fluorapatite precipitated from aqueous experiments, which is invariably fine-grained in size. This modeling may provide insights into possible controls (e.g., dissolution/precipitation/recrystallization, morphology, surface structure, substitution mechnism, etc.) on the uptake of REEs in phosphate deposits and in biogenic apatites.

Chapter 6

Future Work

1. Quantum-mechanical modeling is required to understand the physical significance of the principal directions and principal values of the spin-hamiltonian terms, e.g., of type BS (**g**), S^2 (**D**), BI ($\mathbf{g}_n$), I^2 (**P**), and SI (**A**).

2. The local structural environments of the two Gd^{3+} centres from this study provided constraints on two important substitution mechanisms for incorporating REE^{3+} ions into fluorapatites. Two other substitution mechanisms proposed for incorporating REE^{3+} ions into fluorapatites are (Fleet & Pan, 1995b; 1997a):

$$Gd^{3+} + Na^{+} \Leftrightarrow 2Ca^{2+}, \qquad Ca_{10-2x}\,Na_xGd_x(PO_4)_6F_2\ , \qquad (1)$$

$$Gd^{3+} + Si^{4+} \Leftrightarrow Ca^{2+} + P^{5+}, \qquad Ca_{10-x}\,Gd_x(P_{1-x}Si_xO_4)_6F_2\ . \qquad (2)$$

They can be investigated by a single-crystal EPR study. Single-crystal fluorapatite doped with Gd^{3+} (~100 ppm) and Na^{+} has been successfully synthesized. Preliminary X-band observation on the single-crystal and powder samples indicated that the Gd^{3+} signal of this sample is relatively weak because of the low Gd content, but the central line (transition: $-1/2 \leftrightarrow +1/2$) from a Gd^{3+} centre(s) can still be clearly detected, which is expected to be caused by a new Gd^{3+} centre ('c') in fluorapatite. The local structural environment of 'c' is expected to be different from those determined for 'a' and 'b'. The central lines

from the X-band experiments can be used to determine the g matrix for the Gd^{3+} centre 'c'. However, W-band experiments are required to investigate the local structural environment of 'c', because some transitions of this centre are difficult to detect in the X-band EPR.

3. An experiment is required to synthesize single-crystal fluorapatite doped with both Gd^{3+} and Si^{4+} ions to investigate the substitution mechanism expressed by equation (2), which may correspond to another Gd^{3+} centre ('d'). This investigation is appealing in that many synthetic apatite crystals in the laser industry are REE-bearing silicate apatites (Elliott 1994; Gruber et al. 1999). The local structural environment of centre 'd' is expected to be distinct comparing to those of centres 'a', 'b' and 'c', and therefore may be studied by single-crystal EPR.

4. The W-band EPR spectra of this study suggested that the site occupancy ratio of Gd between the two Ca sites (i.e., $Gd_{Ca2}/Gd_{Ca1} = 0.19$) in flux-grown fluorapatite of ~57 ppm Gd (Chen et al. 2001b) differs from that (2.03) in hydrothermally-grown fluorapatite of 10.36 wt% Gd_2O_3 (Fleet and Pan 1995b). Several factors (e.g., charge-compensating mechanisms and temperature) have been postulated to be responsible for this discrepancy (Chen et al. 2001b). These factors can be tested by a W-band EPR study of Gd-doped fluorapatite samples that are synthesized at different temperatures and contain variable amounts of Gd and other impurities.

5. ENDOR to search for ^{19}F fluorapatite.

6. Most low-temperature and biogenic apatites are invariably fine-grained in size. The successful simulations of the powder EPR spectra by using the calculated spin-hamiltonian parameters of the two Gd^{3+} centres of this study point to their possible applications to low-temperature and biogenic apatites. Accordingly, precipitation experiments using artificial seawater have been made to produce fine-grained Gd-bearing fluorapatite samples at ~85°C. Also, adsorption experiments have been performed for fine-grained fluorapatite samples in solutions of variable Gd contents. These experimental products will be investigated by powder W- and Q-band EPR studies, in order to provide insights into the uptake of REEs by fluorapatite in low-T hydrothermal environments.

7. Computer modeling (Chen, 2001d) suggested that synchrotron EXAFS spectra are probably capable of distinguishing the local structural environments of Gd in the two Ca sites in fluorapatite. Therefore, a combined EPR and EXAFS study on the uptake of REEs by fine-grained apatites may be fruitful.

REFERENCES

Abragam, A. and Bleaney B. (1970): Electron paramagnetic resonance of transition ions, 991p. Clarendon Press, Oxford.

Al'tshuler, S.A., and Kozyrev, B.M. (1974) Electron paramagnetic resonance in compounds of transition elements, 2nd rev. ed., Halstead-Wiley, New York, NY.

Amoros, J.L., Buerger, M.J., and Amoros, M.C. (1975) The Laue method. Academic Press, New York, NY.

Baker, J.M. and Bleaney, B.B. (1958) Paramagnetic resonance in some lanthanon ethyl sulphates. Proceedings of the Royal Society of London, 245A, 156-174.

Blumberg, W.E., Eisinger, J., and Geschwind, S. (1963) Cu^{3+} ion in corundum. Physical Review, 130, 900-909.

Borisov, S.V. and Klevtsova, R. F. (1963) The crystal structure of REE-Sr apatite. Zhurnal Structurnoi Khimii, 4, 629-631.

Brodbeck, C.M., and Bukrey, R.R. (1981) Model calculations for the coordination of Fe^{3+} and Mn^{2+} ions in oxide glasses. Physical Review B, 24, 2334-2342.

Brown, I.D. (1981) The bond-valence method: An empirical approach to chemical structure and bonding. In Structures and Bonding in Crystals II, M. O'Keeffe and A. Navrotsky, Eds., Academic Press, New York, NY, 1-30.

Buckmaster, H.A., Chatterjee, R., and Shing, Y.H. (1972) The application of tensor operators in the analysis of EPR and ENDOR spectra. Physica Status Solidi (A), 13, 9-50.

Buckmaster, H. A., Chatterjee, R., and Malhotra, V. M. (1981) Generalized spin hamiltonian to describe EPR and ENDOR spectra of $^{57}Fe^{3+}$ in trigonal symmetry. Journal of Magnetic Resonance, 43, 417-426.

Calas G. (1988) Electron paramagnetic resonance, Spectroscopic Methods in Mineralogy and Geology. Reviews in Mineralogy, 18, 513-572.

Chen, N., Pan, Y., and Weil, J.A. (1999) Single-axis crystal holder for EPR work, and use of powdered DPPH as a *g*-standard. EPR Newsletter of the International EPR (ESR) Society, 10, 6-7.

Chen, N., Pan, Y., and Weil, J.A. (2001a) Electron paramagnetic resonance spectroscopic study of synthetic fluorapatite: I. Local structural environment and substitution mechanism of Gd^{3+} at the Ca2 site. American Mineralogist (accepted).

Chen, N., Pan, Y., Weil, J.A., and Nilges, M.J. (2001b) Electron paramagnetic resonance spectroscopic study of synthetic fluorapatite: II. Gd^{3+} at the Ca1 site, with a neighboring Ca2 vacancy (accepted).

Chen, N., Pan, Y., Weil, J.A., and Nilges, M.J. (2001c) Electron paramagnetic resonance spectroscopic study of synthetic fluorapatite: III. ^{157}Gd-doped crystals and hyperfine splitting anisotropy (work in progress).

Chen, N. (2001d) Computer modeling of the EXAFS spectrum for two Gd-occupied Ca sites in fluorapatite (term paper for PHYS 893.3).

Close, D.M., Mengeot, M., and Gilliam, O.R. (1981) Low-temperature intrinsic defects in x-irradiated hydroxyapatite synthetic single crystals. Journal of Chemical Physics, 74, 5497-5503.

Comodi, P., Liu, Y., Stoppa, F., and Woolley, A. R. (1999) A multi-method analysis of Si-, S- and REE-rich apatite from a new kind of kalsillite-bearing leucitite (Abruzzi, Italy). Mineralogical Magazine, 63, 661-672.

Elliott, J.C. (1994) Structure and chemistry of the apatite and other calcium orthophosphates. Elsevier Science B.V., Amsterdam, the Netherlands.

Elliott, J.C., MacKie, P.E., and Young, R.A. (1973) Monoclinic hydroxyapatite. Science, 180, 1055-1057.

Fleet, M.E., Liu, X., and Pan, Y. (2000a) Rare-earth elements in chlorapatite [$Ca_{10}(PO_4)_6Cl_2$]: Uptake, site preference and degradation of monoclinic structure. American Mineralogist, 85 1437-1446.

Fleet, M.E., Liu, X., and Pan, Y. (2000b) Site preference of rare-earth elements in hydroxyapatite [$Ca_{10}(PO_4)_6(OH)_2$]. Journal of Solid State Chemistry, 149, 391-398.

Fleet, M.E., and Pan, Y. (1997a) Rare-earth elements in apatite: Uptake from H_2O-bearing phosphate-fluoride melts and the role of volatile components. Geochimica et Cosmochimica Acta, 61, 4745-4760.

Fleet, M.E., and Pan, Y. (1997b) Site preference of rare-earth elements in fluorapatite: Binary (LREE+HREE)-substituted crystals. American Mineralogist, 82, 870-877.

Fleet, M.E., and Pan, Y. (1995a) Crystal chemistry of rare-earth elements in fluorapatite and some calc-silicates. European Journal of Mineralogy, 7, 591-605.

Fleet, M.E., and Pan, Y. (1995b) Site preference of rare-earth elements in fluorapatite. American Mineralogist, 80, 329-335.

Gaft, M., Reisfeld, R., Panczer, G., Shoval, S., Champagnon, B., and Boulon, G. (1997) Eu^{3+} luminescence in high-symmetry sites of natural apatite. Journal of Luminescence, 72-74, 572-574.

Gaite, J.M. (1980) Pseudo-symmetries of crystallographic coordination polyhedra. Application to forsterite and comparison with some EPR results. Physics and Chemistry of Minerals, 6, 9-17.

Gaite, J.M. (1987) Study of the structural distortion around S-state ions in crystals, using the fourth-order spin-hamiltonian term of the EPR spectral analysis. In Electronic Magnetic Resonance of the Solid State, Weil, J. A., Ed., Canadian Society of Chemistry, 151-174.

Gaite, J.M., Bulka, G.R. , Hasanova, N.M., Nizamutdinov, N.M., and Vinokurov, V.M. (1985a) Study of the environment of Fe^{3+} in $Na_2Cd(SO_4)_22H_2O$ by EPR. Journal of Chemical Physics, 82, 4358-4361.

Gaite, J.M., Bulka G.R., Hasanova, N.M., Nizamutdinov, N.M., and Vinokurov, V.M. (1985b): EPR of Gd^{3+} in $Na_2Cd(SO_4)_22H_2O$, comparison with previous results obtained for Fe^{3+}. Journal of Chemical Physics, 83, 6088-6090.

Gaite, J.M., and Michoulier, J. (1973) Electron paramagnetic resonance of Fe^{3+} in diopside and spodumene. Journal of Chemical Physics. 59, 488-494.

Geschwind S. (1961) Paramagnetic resonance of Fe^{3+} in octahedral and tetrahedral sites in yttrium gallium garnet (YgaG) and anisotropy of yttrium iron garnet (YIG). Physical Review, 121, 363-374.

Grandjean-Lecuyer, P., Feist, R., and Albarede, F. (1993) Rare-earth elements in old biogenic apatites. Geochimica et Cosmochimica Acta, 57, 2507-2514.

Grauch R. I. (1989) Rare earth elements in metamorphic rocks. Reviews in Mineralogy, 21, 147-167.

Greenblatt, M. (1980) Electron spin resonance of tetrahedral transition oxyanions (MO_4^{n-}) in solids. Journal of Chemical Education, 57, 546-551.

Gruber, J.B., Zandi, B., Ferry, M., and Merkle, L.D. (1999) Spectra and energy levels of trivalent samarium in strontium fluorapatite. Journal of Applied Physics, 86, 4377-4382.

Isoya, J., Tennant, W.C., Uchida, Y., and Weil, J.A. (1982) Biradical center in α-quartz. Journal of Magnetic Resonance, 49, 489-497.

Halford, D., Hutchison, C.A., and Llewellyn, P.M. (1958) Electron nuclear double resonance of neodymium. The Physical Review, 110, 284-286.

Holmden, C., Creaser, R. A., Muehlenbachs, K., Leslie, S. A., and Bergstrom, S.M. (1998) Isotopic evidence for geochemical decoupling between epeiric seas and bordering oceans: Implications for secular curves. Geology, 26, 567-570.

Hughes, J.M., Cameron, M., and Crowley, K.D. (1989) Structural variations in natural F, OH, Cl apatites. American Mineralogist, 74, 870-876.

Hughes, J.M., Cameron, M., and Mariano, A.N. (1991) Rare-earth-element ordering and structural variations in natural rare-earth-bearing apatites. American Mineralogist, 76, 1165-1173.

Kliava, J. (1982) Superposition model analysis of the short-range ordering for Mn^{2+} in oxide glasses. Journal of Physics C: Solid State Physics, 15, 7017-7029.

Lee, S. and Brodbeck, C.M. (1977) Magnetic-resonance line-broadening effects associate with crystalline imperfections. Physical Review B, 16, 4743-4745.

Mckay G. A. (1989) Partitioning of rare earth elements between major silicate minerals and basaltic melts. Reviews in Mineralogy, 21, 45-77.

MacKie, P.E., and Young, R.A. (1973) Location of Nd dopant in fluorapatite, $Ca_5(PO_4)_3F$:Nd. Journal of Applied Crystallography, 6, 26-31.

McDonough, W. F. and Frey F. A. (1989) Rare earth elements in upper mantle rocks. Reviews in Mineralogy. 21, 100-145.

McGavin, D.G. (1987) Symmetry constraints on EPR spin-hamiltonian parameters. Journal of Magnetic Resonance, 74, 19-55.

Michoulier, J., and Gaite, J.M. (1972) Site assignment of Fe^{3+} in low-symmetry crystals. Application to $NaAlSi_3O_8$. Journal of Chemical Physics, 56, 5205-5213.

Minge J. and Weil, J.A. (1989) ^{57}Fe hyperfine structure of $[FeO_4/Li]^0$ center in α-quartz. Journal of Physics and Chemistry, 50, 997-1001.

Mombourquette, M.J., Tennant,W.C., and Weil, J.A. (1986) EPR study of Fe^{3+} in α-quartz:a reexamination of the so-called *I* centre. Journal of Chemical Physics, 85, 68-79.

Mombourquette, M.J., and Weil, J.A. (1987) Modeling Fe^{3+} in quasitetrahedral surroundings using the Newman superposition model. Journal of Chemical Physics, 87, 3385-3391.

Mombourquette, M.J., Weil, J.A., and McGavin, D.G. (1996) EPR-NMR user's manual. Department of Chemistry, University of Saskatchewan, Saskatoon, Saskatchewan.

Nilges, M.J., Smirnov, A. I., Clarkson, R.B., and Belford, R.L. (1999) Electron paramagnetic resonance W-band spectrometer with a low-noise amplifier. Applied Magnetic Resonance, 16, 167-183.

Pan, Y., and Breaks, F. W. (1997) Rare earth elements in fluorapatite, Separation Lake area, Ontario: Evidence for S-type granite-rare-element pegmatite linkage. Canadian Mineralogist, 35, 659-671.

Pan, Y., and Fleet, M.E. (1996) Intrinsic and external controls on the incorporation of rare-earth elements in calc-silicate minerals. Canadian Mineralogist, 34, 147-159.

Pan, Y., Fleet, M.E., and MacRae, N.D. (1993) Oriented monazite inclusions in apatite porphyroblasts from the Hemlo gold deposit, Ontario, Canada. Mineralogical Magazine, 57, 697-707.

Pan, Y., and Stauffer, M.L. (2000) Cerium anomaly and Th/U fractionation in the 1.85 Ga Flin Flon Paleosol: Clues from REE- and U-rich accessory minerals and implications for paleoatmospheric reconstruction. American Mineralogist, 85, 898-911.

Pifer, J.H., Ziemski, S., and Greenblatt, M. (1983) Effect of anion substitution on the electron spin resonance of Cr^{5+} calcium phosphate apatite. Journal of Chemical Physics, 78, 7038-7043.

Prener, J.S. (1976) The growth and crystallographic properties of calcium fluo- and chlorapatite crystals. Journal of the Electrochemical Society, 114, 77-83.

Shaltiel, D. and Low, W. (1961) Anisotropic broadening of linewidth in the paramagnetic resonance spectra of magnetically dilute crystals. Physical Review, 124, 1062-1066.

Tennant, W.C., Walsby, C.J., Claridge, R.F.C., and McGavin, D.G. (2000) Rotation matrix elements and further decomposition functions of two-vector tesseral spherical tensor operators; their uses in electron paramagnetic resonance spectroscopy. Journal of Physics: Condensed Matter, 12, 1-15.

Urusov, V.S., and Khudolozhkin, V.O. (1974) An energy analysis of cation ordering in apatite. Geochemistry International, 11, 1048-1053.

Warren, R.W. (1970) EPR of Mn^{2+} in calcium fluorophosphates. I. the Ca(II) site. Physical Review B 2, 4383-4388.

Watson, E.B., and Green, T.H. (1981) Apatite/liquid partition coefficients for the rare-earth elements and strontium. Earth and Planetary Science Letters, 56, 405-421.

Weil, J.A. and Anderson, J. H. (1961) Direct field effects in electron paramagnetic resonance hyperfine spectra. Journal of Chemical Physics, 35, 1410-1417.

Weil, J.A., Bolton, J.R., and Wertz, J.E. (1994) Electron paramagnetic resonance, Elementary theory and practical applications. Wiley-Interscience, New York.

Weil, J.A., Buch T., and Clapp, J.E. (1973) Crystal point group symmetry and microscopic tensor properties in magnetic resonance spectroscopy. Advances in Magnetic Resonance, 6, 183-257.

Wenzel, R.F., and Kim, Y.W. (1965) Linewidth of the electron paramagnetic resonance of $(Al_2O_3)_{1-x}(Cr_2O_3)_x$. Physical Review, 140, A1592-A1598.

Wright, J., Seymour, R.S., and Shaw, H.F. (1984) REE and neodymium isotopes in conodont apatite: Variations with geological age and depositional environment. Geological Society of America, Special Paper 196, 325-340.

Wronkiewicz, D.J., Wolf, S.F., and DiSanto, T.S. (1996) Apatite- and monazite-bearing glass-crystal composites for the immobilization of low-level nuclear and hazardous wastes. Materials Research Society, 412, 345-352.

Yablokov, Y. V., (1960) Paramagnetic resonance in different forms of 2,2-diphenyl-1-picrylhydrazyl. Doklady Akademii SSS (English transition). 133 424-426.

APPENDIX I

Computer Software EPR-NMR

The computer program EPR-NMR (Mombourquette et al. 1996) was used in the data analysis of this thesis work. EPR-NMR was initiated at the Chemistry Division of Argonne National Laboratory, USA and developed continually by the EPR group headed by Dr. J. A. Weil at the Department of Chemistry, University of Saskatchewan, Canada. It is written in the programming language FORTRAN-77 and can be compiled on a PC computer. It is very flexible and can be adopted for various computer systems, e.g., VAX/VMS, DECStation 5000/125, and M680x0. Computations are carried out by the program to FORTRAN double precision.

EPR-NMR can be used to optimize spin-hamiltonians, to perform the angle corrections for Zeeman-field directions, as well as spectrum simulations [e.g., energy levels, angular dependence of line positions and relative intensity (roadmaps), single-crystal and powder spectra (line shape and line positions), EPR signal relative intensity, magnetic-site splittings, estimation of relative abundances for different EPR species in single-crystal- and powder samples]. A schematic diagram of the program is shown in appendix 1.1. EPR-NMR has various operating modes, which are grouped into four categories according to the operating complexity, as follows: a) the energy-levels can be simulated for a known spin-hamiltonian at a given Zeeman-field direction; b) the spectrum can be simulated for assigned transition(s), i.e., electron paramagnetic resonance (EPR) or nuclear magnetic resonance (NMR) in either field-swept or

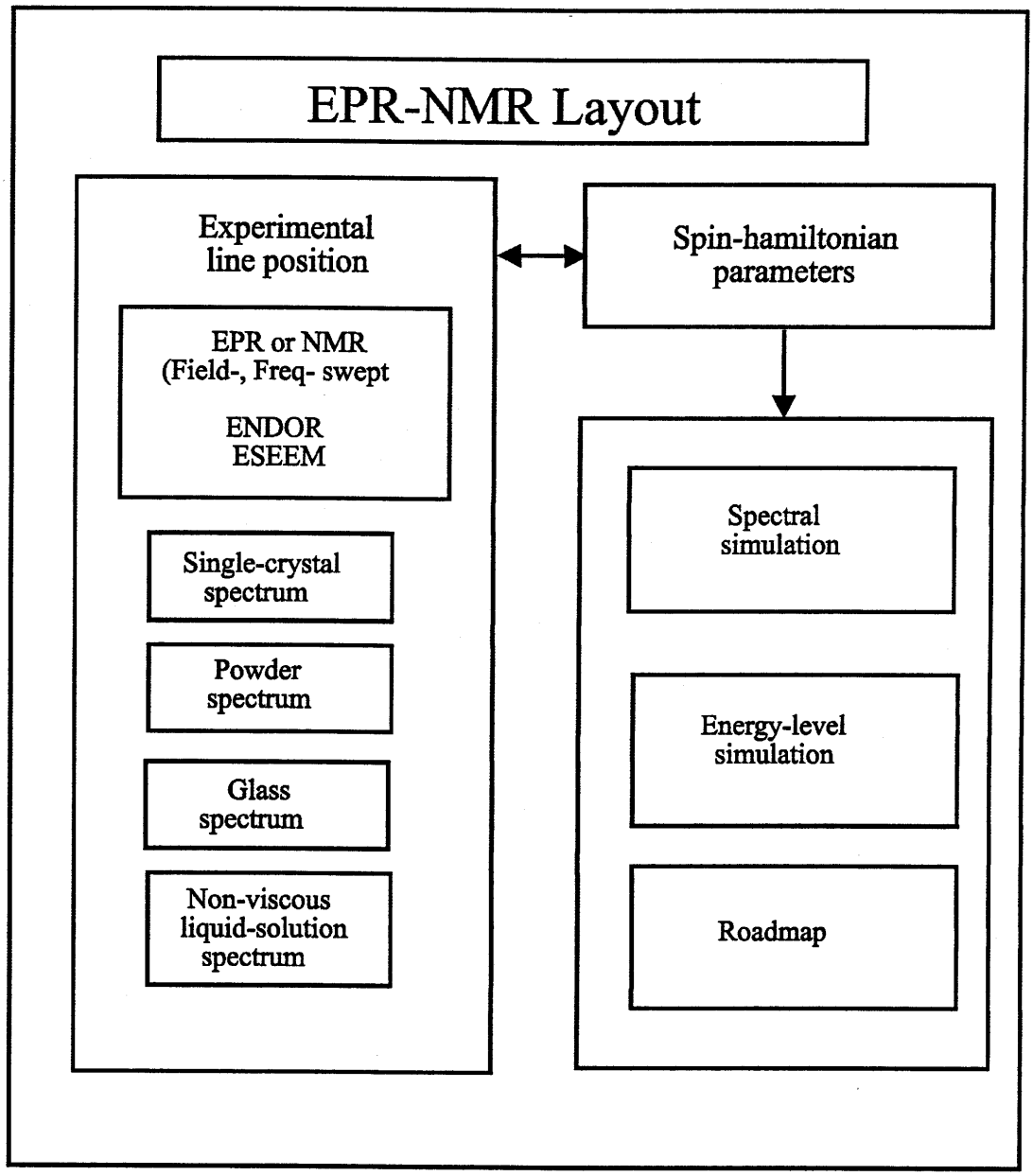

Appendix 1.1. Schematic diagram of the program EPR-NMR (from Mombourquette et al., 1996).

```
BCORR=(0.0,0.0,0.0) BJ3 BJ5 ECHO EPRFD J4 J6
INTENS MINIM Nblock=1 Nsite=2 NVP=6
PrtDevia=2.0 PrtProPar RotGrp=C2 WeightF

Gd in AP30(30),fitting, ROT 1,2 & 3

3.5

1.995     0.000      0.000
          1.995      0.000
                     1.995

69.329    0.000      0.000
         69.399      0.000
                  -138.728

0.0 0.0 0.0 0.0 0.0
0.0 0.0 0.0 0.0

0.0 0.0 0.0 0.0 0.0
0.0 0.0 0.0 0.0 0.0
0.0 0.0 0.0

0.0 0.0 0.0 0.0 0.0
0.0 0.0 0.0 0.0 0.0
0.0 0.0 0.0 0.0

0.0 0.0 0.0 0.0 0.0
0.0 0.0 0.0 0.0 0.0
0.0 0.0 0.0 0.0 0.0
0.0 0.0 0.0 0.0 0.0
0.0 0.0

1 2 3 4 5 6
0 0 0 0 0 0

0.0 0.0

315

90.0   0.0    1      9197.404772
4
1      2      2654.81      1.0
2      3      2913.01      0.0001
6      7      3635.26      0.0001
7      8      4004.76      1.0

90.0   0.0    1      9197.971761
1
3      4      3111.63      1.0

90.0   0.0    1      9197.974405
1
4      5      3270.88      1.0
```

Command lines

Title & annotation

Principal spin quantum number

g

$S^2(D)$

S^4

S^6

BS^3

BS^5

SH parameters varied & tied

Excitation field θ,ϕ (degree)

Number of data points

Zeeman field direction θ,ϕ
block number
transition frequency
number of transitions

transition labels
observed fields
weighting factors

Appendix 1.2a. An example of an input file to EPR-NMR for optimization of matrix g.

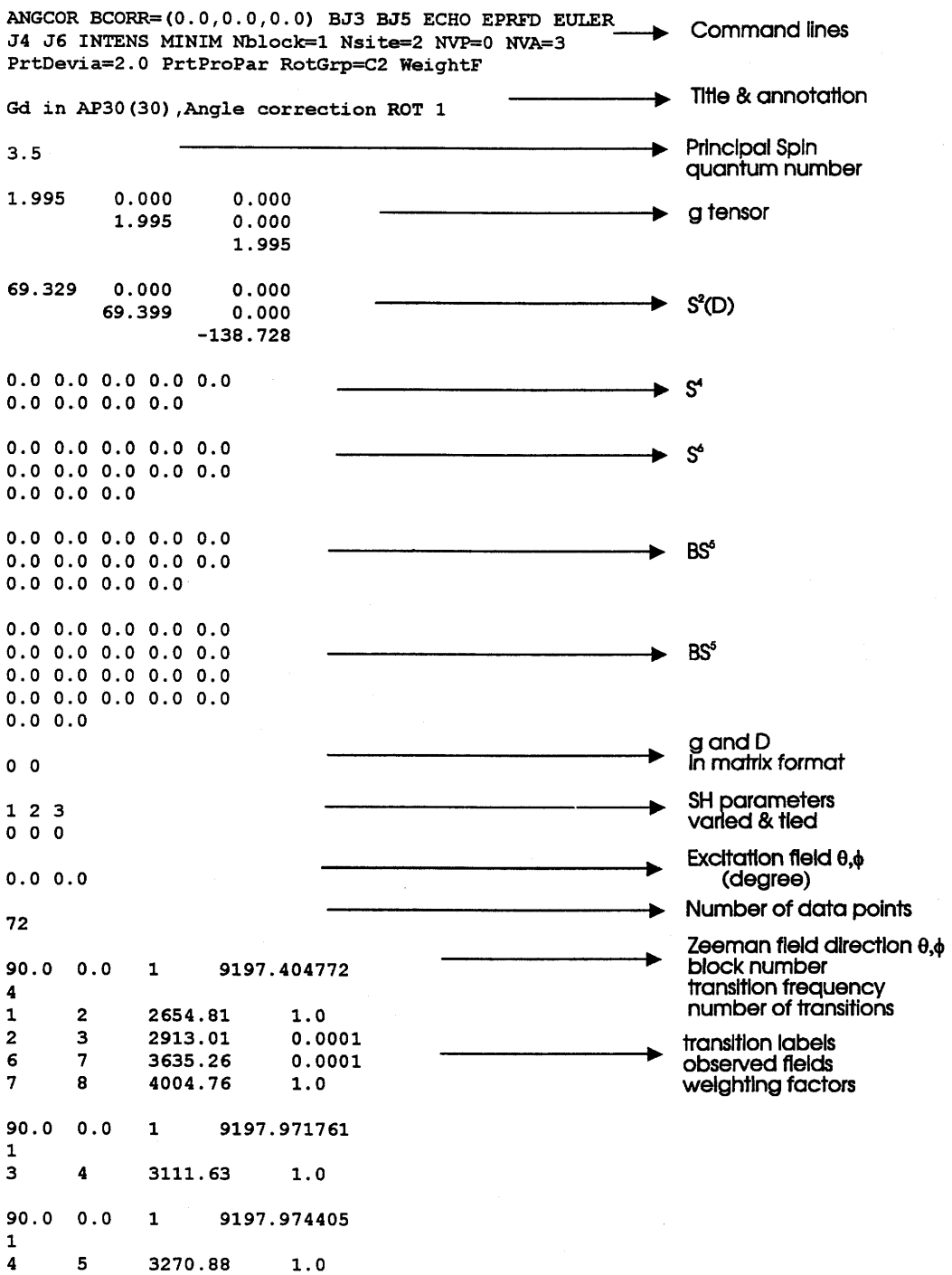

Appdendix 1.2b. An example of an input file to EPR-NMR for angle correction.

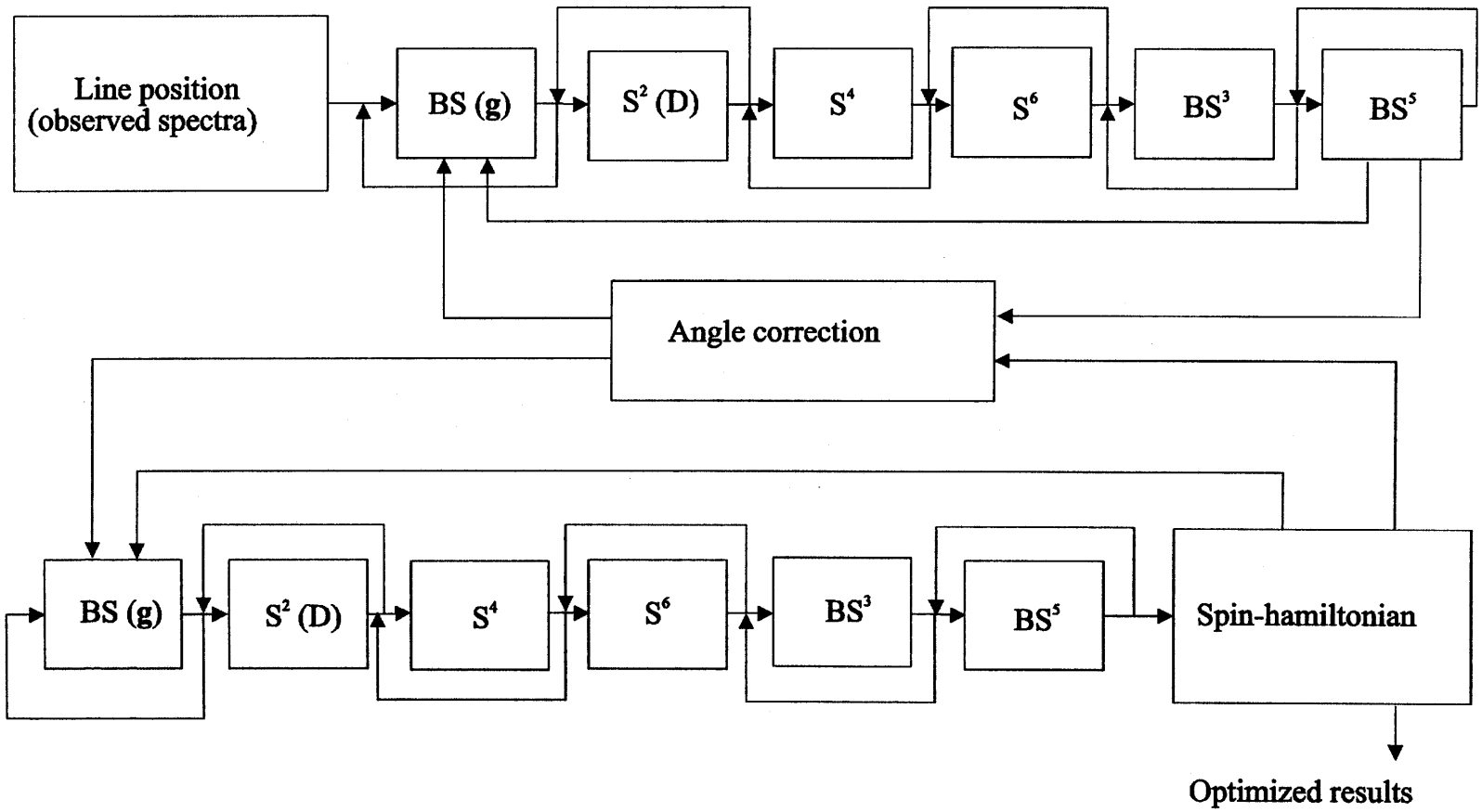

Appendix 1.3. Flow-chart of the optimization procedure for the spin-hamiltonian parameters of (say) even-isotope Gd^{3+} EPR spec

frequency-swept mode. Spectra also can be simulated for electron-nucleus double resonance (ENDOR), and electron spin echo envelope modulation (ESEEM). The simulation can include transition frequencies or magnetic-field magnitudes, and relative transition probabilities. The simulated spectrum is convoluted to a line-shape of a lorentzian or gaussian function;

c) a comparison can be made concerning the consistency between the observed single-crystal data and calculated ones with given spin-hamiltonian parameters; d) the spin-hamiltonian subset(s) under correction of the directions of the field **B** can may be optimized by a non-linear least-squares routine. Initial spin-hamiltonian parameters are required, but they need only be estimates or outright guesses. The program can iterate systematically the parameters so as to minimize the difference between observed and calculated spectra (line positions) to obtain the best-fitting.

To perform a calculation with EPR-NMR, the type of chosen calculation(s) (i.e., mode) and necessary data needed to perform the operation(s) need to be specified in an input file to the program. Appendix 1.2a and 1.2b show examples of the input files for the optimization of the parameters in the matrix **g**, and the directions of the magnetic fields. The general flow-chart of the optimization procedure for spin-hamiltonians of the even isotopes Gd^{3+} is shown in Appendix 1.3.Generally, an input file for EPR-NMR can be divided into three portions, i.e., command block, parameter block, and data block.

The command block specifies the operation(s) to be taken. The command block may have several lines composed of a series of commands, separated by spaces or commas. These commands determine the format of the other two blocks in the input file and the operation to be performed by the program. Commands used in this work are defined, for example, as follows:

ANGCOR: the command to switch on the angle minimization independently or simultaneously for polar coordinates of the rotation planes and thus calibrate the error in orientations of the Zeeman-field directions.

BCORR(0.0, 0.0, 0.0): a magnetic-field correction will be added to each observed field in a unit defined by command FLDunites. The default unit is Gauss. This operation is most useful when there is a systematic magnetic field error. If the line positions in the input file have calibrated, the parameters in the command will be set to be zero.

$\mathbf{J_4}$, $\mathbf{J_6}$, $\mathbf{BJ_3}$, $\mathbf{BJ_5}$: These terms corresponds to the spin-hamiltonian terms of types $\mathbf{S}^4$ ($\mathbf{I}^4$); $\mathbf{S}^6$; $\mathbf{BS}^3$ and $\mathbf{BS}^5$, respectively. The parameters in these terms need to be assigned in the parameter block.

ECHO: The output file of EPR-NMR will include the complete data set assigned in the input file if this command is switched on. Otherwise only the command lines are echoed.

EPRFD: A field-swept EPR experiment is specified.

EULER: the command to specify the format of one (or more) of the spin-hamiltonian term(s) (i.e., matrices) in the input file. If the command is switched on, the specified matrix is input as three principal values and three Euler angles. Both of the principal values and Euler angles are optimized, rather than matrix elements. In the angle-correction process, all minimization operations for spin-hamiltonian parameters have been switched off, only the three Euler angle are optimized. Here the specified matrices (e.g., matrices **g** and **D**) are still input matrix format.

INTENS: Relative transition probabilities are calculated.

MINIM: The command switches on the operation of parameter optimization.

Nblock: Number of blocks where data to be are stored. The maximum number is twelve.

Nsite: Number of the symmetry-related sites.

NVP: Number of variable spin-hamiltonian parameters. NVP is different for various types of spin-hamiltonian terms. It is 1 to 6 for BS (**g**) and SI (**A**);1 to 5 S^2(**D**) and I^2(**P**); 1 to 9, 1 to 13; 1 to 14; 1 to 22 for the tensors S^4, S^6 and BS^3 and BS^5, respectively.

PrtDevia: "$$$" sign option indicates fitting error. When the command is specified, "$$$" will be added to calculated frequencies and magnetic field in the output file, in the case the weighted difference between the calculated result and observed ones is larger than the specified RMSD.

PrtProPar: The program parameters will be included in the output file.

RotGrp: specification of the proper rotation group of crystal symmetry.

WeightF: The weighting factors can be specified in the input file along with each observed magnetic field. The weighting factor is a non-negative number varied between 1 and 0. Its value corresponds to the accuracy of the EPR observation. A larger factor will be assigned to an observed line with higher accuracy, while a small factor is assigned if the accuracy is low. If the command is off, all weighting factors are assigned to be 1.0.

The parameter block includes file title and annotation, spin quantum numbers, related spin-hamiltonian terms, as well as varied and tied spin-hamiltonain parameters. The parameters can be optimized simultaneously or separately, i.e., fitting simultaneous for the parameters in all terms, fitting for the all parameters in each of the chosen type of

term separately; fitting for the part of the especially assigned parameters in a single term, fitting for the especially assigned parameters from different terms.

The data block includes the information concerning excitation-field direction assigned by polar angles (i.e., θ_0, φ_0; in degrees); number of data points; Zeeman-field directions (i.e., θ, φ); block number(s), transition frequencies; number of transitions, transition labels, observed line positions (in Gauss), and weighting factors. During the iteration processing of minimization, transition labels, weighting factors, and Zeeman field directions will be changed gradually until an acceptable result for the root-mean-sum-of-squares of weighted differences (RMSD) is reached.

Appendix II

Computer Software ROTSTO

The computer software ROSTO was the second software used in this thesis work. ROTSTO was initiated by W. C. Tennant at the Institut fuer Anorganische Chemie, Universitaet-Mainz in 1989, extended by C. J. Walsby in 1998, and further extended and re-coded by W. C. Tennant (1999) at the Department of Chemistry, University of Canterbury, New Zealand.

ROTSTO is a FORTRAN program designed to carry out two kinds of EPR research. At first the software can calculate "new" values for the spin terms of type **BS** (**g**), and $\mathbf{S}^2$ (**D**), and the parameters associated with the high-spin terms of type $\mathbf{S}^4$, $\mathbf{S}^6$, and $\mathbf{BS}^3$ as well as $\mathbf{BS}^5$ by use of the Euler rotation between different reference systems. Secondly it can make local-symmetry analysis for the paramagnetic species by using the technique of pseudo-symmetry analysis, which has been used widely in EPR studies (e.g., Michoulier and Gaite, 1972; Gaite, 1980; Gaite et al., 1985a,b; Mombourquette et al., 1986).